THESIS

Co-tutelle thesis Lille University / Samara State Technical University

Ecole Doctorale
Sciences de la Matière du Rayonnement et de l'Environnement

presented by

Maria Nikulshina - Kulikova

for the degree of

Doctor in Chemistry
Chemistry-Physical chemistry

(Ni)MoWS alumina supported hydrotreating catalysts prepared from mixed $H_4SiMo_nW_{12-n}O_{40}$ heteropolyacids

Date of the thesis defence: April 20th, 2018

Jury

Victor Kogan, Professor, N.D. Zelinsky Institute of Organic Chemistry, Russia	**Referee**
Frédéric Richard, Assistant Professor, University of Poitiers, France	**Referee**
Françoise Maugé, Directeur de Recherche, University of Caen, France	**Member**
Andrey Pimerzin, Professor, Samara State Technical University, Russia	**Member**
Pavel Nikulshin, Leading Researcher, Samara State Technical University, Russia	**Supervisor**
Carole Lamonier, Professor, Lille University, France	**Supervisor**
Pascal Blanchard, Assistant Professor, Lille University, France	**Invited**
Christine Lancelot, Assistant Professor, Lille University, France	**Invited**

TABLE OF CONTENTS

Chapter 4

4. Ni-promoted alumina supported NiMoWS hydrotreating catalysts

INTRODUCTION

Hydrotreatment is an important group of processes in the petroleum refining industry. It has been used for more than 80 years and the technology has progressively evolved [1]. It is known, that NO_x and SO_x emissions from fuel combustion processes are the major component of air pollutants influencing on human health and environment. The main difficulty of the oil refining industry, at present, is associated with more stringent environmental requirements for motor fuels (transportation fuels), namely, to reduce the content of heteroatomic (S-, N- and O-containing) and aromatic compounds [2]. Moreover, to follow the increasing market demand for higher quality products as ultra low sulfur diesel (ULSD) the process becomes complicated due to the decrease of crude oil quality and diesel feed streams available to refiners [3].

One of the key approaches for overcoming these challenges is the development of new highly active hydrotreating (HDT) catalysts that allow producing ultra-clean fuels at mild conditions and operational expenditures [4,5]. Today it is a well-known fact that the active phase of HDT catalysts is composed of molybdenum (tungsten) disulfide promoted with cobalt and/or nickel atoms [6,7]. Researches aimed at changing the active phase composition, the promoter/molybdenum ratio and the support nature were proposed to improve the catalytic properties.

The development of the trimetallic NiMoWS bulk catalyst «Nebula» in the early 2000 allowed crossing over to a new level of activity of hydrotreating catalysts. This catalyst exhibits activity at least three times higher than any other hydrotreating catalyst, conventionally used in industry [8]. Based on the correlation between the energy of the metal-sulfur bond calculated by DFT and hydrodesulfurization performances evaluated in dibenzothiophene HDS, P. Raybaud and co-workers [9] reported a new synergy effect when Ni is used as a promoter for $MoWS_2$ solid solution. Thus NiMoWS catalyst had higher HDS activity than NiMoS and NiWS. In contrast, CoMoWS catalyst resulted from the linear combination of the thiophene HDS activities of the two CoWS and CoMoS references.

Olivas et al. [10] confirmed that synergetic effect of Ni is present in mixed $(Mo-W)S_2$ clusters by comparison with supported $Ni(MoS_2)$ and $Ni(WS_2)$ separated catalysts. Therefore, it should be concluded that trimetallic Ni–Mo–W sulfide catalysts have a potential advantage over bimetallic Ni-Mo and Ni-W systems, in respect to deep sulfur and nitrogen removal. However, precise determination of the reasons of high activity of these catalysts is not simple. Some authors supposed that mixed Ni-Mo-W active sites are formed [11]. However, the experimental investigations of bimetallic mixed Mo-W active sites are scarce. At the same time, the

development of effective ways to form mixed Mo-WS$_2$ slabs seems to be a key to design new highly effective hydroprocessing catalysts.

The aim of the study is the investigation of Mo-W synergetic effect in catalysis by bi- and trimetallic MoW and NiMoW sulfides and development of new highly efficient hydrotreating catalysts based on the use of mixed SiMo$_n$W$_{12-n}$ heteropolyacids as Mo and W precursors.

The thesis consists of five chapters. The first chapter provides an overview of the literature on deep hydrotreatment, and the reactivity of heteroatomic compounds, the structure of active phase and active sites of hydrotreating catalysts. The advantages and potential of using trimetallic NiMoW systems are considered. Methods of preparation of bulk and supported hydrotreatment catalysts, including the use of heteropolyanions as initial precursors, are described.

The second chapter provides the details on the experimental methods involved in this research. The physico-chemical methods, which were used for the characterization of starting precursors and prepared catalysts, as well as the methods for the investigation of the catalytic properties of (Ni)MoW samples, are described.

The third chapter focuses on the synthesis of H$_4$SiMo$_n$W$_{12-n}$O$_{40}$ heteropolyacids and their subsequent characterization by different techniques.

The fourth chapter is devoted to the preparation of unpromoted MoW alumina supported catalysts and the investigation of their physicochemical and catalytic properties in hydrodesulfurization of dibenzothiophene and naphthalene hydrogenation. For the first time, sulfidation in gas phase has been followed by XAS in the ROCK beamline (Soleil synchrotron) allowing to monitor at the same time Mo and W edges. Innovative results have been obtained using the combination of advanced characterization as High Angle Annular Dark Field microscopy (HAADF) and XAS after sulfidation. This chapter also discusses the effect of sulfidation agents, H$_2$S in gas phase or DMDS (dimethyl disulfure) in liquid phase on the catalytic activity.

The fifth chapter describes the synthesis and characterization of Ni-promoted alumina supported MoW hydrotreating catalysts. The catalytic activity of NiMoW/Al$_2$O$_3$ catalysts in hydrotreating of model feed containing DBT and naphthalene is presented. The influence of quinoline addition on the catalytic properties in co-hydrotreating with DBT and naphthalene is discussed. This chapter provides also results of the investigation of trimetallic NiMoW by XAS and HAADF.

Chapter 1

Review of the Literature

1.1. Hydrotreating processes in oil refinery

Release of new stringent standards on the sulfur concentration in the transportation fuels led to an intense research activity on desulfurization. The removal of sulfur compounds is usually performed by hydroprocessing under high H_2 pressure, elevated temperatures (300-400 ºC) in presence of a heterogeneous catalyst. Despite more than a century history of application of transition metal sulfides in hydroprocessing fuels, further improvements of the catalytic activity are a real challenge for the science and industry. This chapter is a review of the literature of catalytic hydroprocessing reactions. It includes data characterizing reactivities, reaction networks, and kinetics of hydrodesulfurization, hydrogenation of aromatic hydrocarbons and hydrodenitrogenation. Special attention is paid to the bulk and supported trimetallic NiMoW systems. Role of precursors focused on the use of heteroplycompounds and preparation techniques in the formation of sulfide catalysts and their catalytic activity is discussed.

1.1.1. Modern state of hydro-processes in oil refinery

Petroleum is by far the most commonly used source of energy, especially for liquid transportation fuels. The increase in energy and fuels demand has led to global petroleum increased consumption and resource depletion. This leads to a need to refine heavy feedstocks and residua to maximize the yield of liquid fuels. It is known that in recent years, the quality of crude oil has become worse (i.e., increase in density, in S and N content) [12,13]. Over the past decades, environmental regulations that require the production of cleaner fuels are compounded by the quality of crude oil and involvement of distillates of secondary processes to refining.

Refinery configurations vary depending on the desired distribution of refinery products (gasoline, gas oil, jet fuel, etc.). Typically, the dewatered and desalted crude oil is separated into different fractions by distillation (atmospheric and vacuum). Obtained straight-run fractions are characterized by their boiling point range (Fig. 1). Hereafter the different fractions are hydrotreated [6,13].
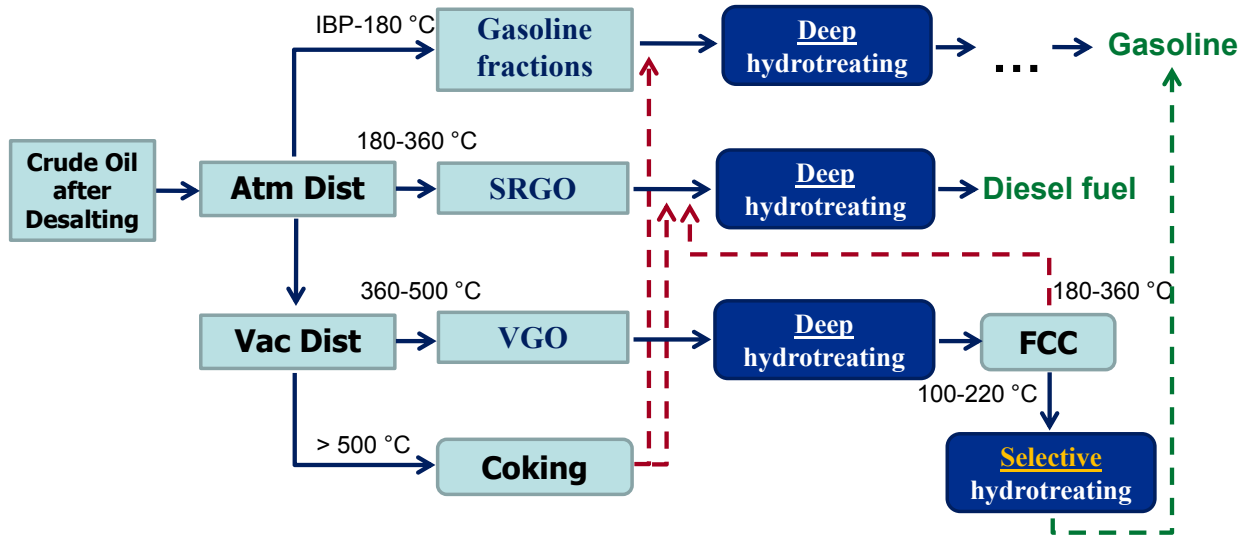
Fig. 1. Role of hydrotreating processes in modern oil refinery.

Hydrotreating is the largest tonnage process of modern refineries. The main purpose of hydrotreating is the removal of heteroatoms from the organic molecules of petroleum cuts. Hydrotreatment provides the upgrading of fuel quality allowing to decrease undesired emissions in exhaust gases. Furthermore, the importance of removing aromatic, S- and N-containing compounds is related to the hydroprocessing catalysts (reforming, hydrocracking, etc.) capacity to resist to poisoning and coking by these compounds.

Many ways to increase deep hydrotreating are used in industry in accordance with the reactivity of the feed and the degree of desulfurization desired. Generally, it can be managed by variation of the operating conditions (increase of the temperature, pressure, hydrogen-rich gas circulation ratio and content of hydrogen, decrease of liquid hourly space velocity (LHSV)) and/or application of highly active catalysts. However, using new highly active catalytic systems does not require a significant change in the operating conditions of the process, and is, therefore, the most efficient solution to the problem of deep hydrotreating.

1.1.2. Main compounds and target reactions of hydrotreating

1.1.2.1. Sulfur-containing compounds and their hydrodesulfurization reactivity

The main task of hydrotreating processes is to reduce the content of sulfur, nitrogen and oxygen compounds in order to decrease their influence on environment and health. Sulfur is the most abundant heteroatom impurity in crude oil, its content varies significantly with their origin from less than 0.1 (North Africa and Indonesia) to more than 14 wt% but generally falls in the range 1 to 4 wt% (Saudi Arabia and Venezuela). Petroleum with less than 1 wt% sulfur is referred to as low-sulfur, and as high-sulfur with more than 1 wt% sulfur. Crude oil contains a complex mixture of a large variety of sulfur compounds with different reactivities (Fig. 2). In the low boiling naphtha fraction, sulfur is mainly present in the form of thiols (mercaptans), sulfides, disulfides, or thiophenes. For the kerosene and gas oil middle distillate fractions, thiophenic compounds containing benzo- and dibenzothiophene structures dominate.

It is known that the hydrodesulfurization (HDS) active sites are sulfur anion vacancies or coordinatively unsaturated sites (CUS) created in a reaction with hydrogen [6]. The adsorption of S-containing molecules, such as thiophene and dibenzothiophene (DBT), occur on these CUS and the bonding is through the S atom (σ-type bond). After HDS, sulfur atom of the reactant remains on the original vacancy. This S atom is subsequently hydrogenated to H_2S and desorbed, regenerating new vacancy.

The transformation of S-containing molecules occurs through two parallel reactions: direct desulfurization (DDS) and prehydrogenation (HYD). The HDS products from DBT include biphenyl (BP) via DDS pathway, as well as cyclohexylbenzene (CHB) and bicyclohexyl (BCH) from the HYD pathway (Scheme 1) [14].
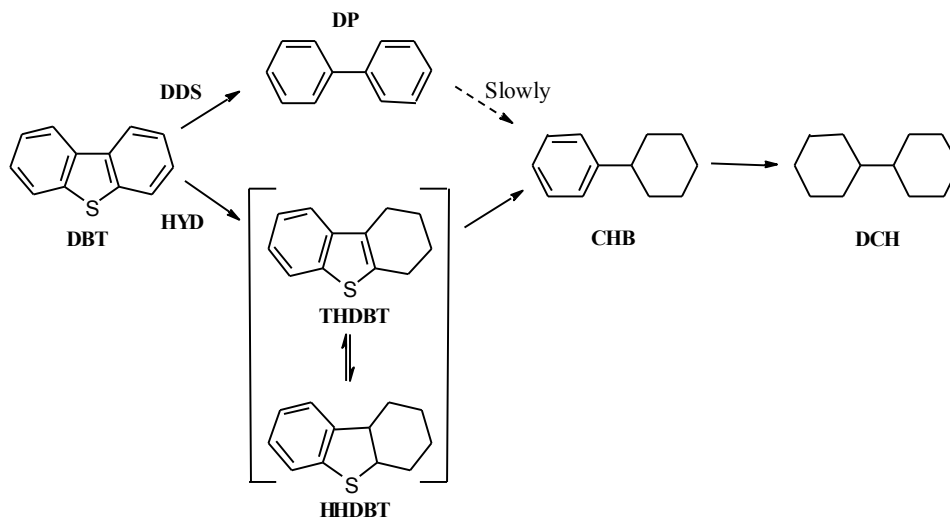
Scheme 1. Reaction network of the HDS of DBT on sulfided NiMo on alumina catalyst [14].

The HYD pathway becomes the predominant one for unpromoted catalysts in DBT HDS, while the DDS pathway is the predominant one for promoted catalysts. The position and size of the alkyl substituting group influence the reactivity of the compounds. Fig. 2 presents a qualitative relationship between the type and size of sulfur molecules in various distillate fuel fractions and their relative reactivities. DBTs carrying two alkyl substituents at the 4- and 6-positions are the most resistant to desulfurization due to the steric hindrance around the sulfur atom [15]. In contrast, 2,8- and 3,6- alkyldibenzothiophenes are as reactive as dibenzothiophene, some of them being even more reactive [14,16,17]. The decrease in the DDS pathway with alkyl substitutes can be explained via adsorption mechanism. The alkyl groups located close to the sulfur atom create a steric hindrance and make the σ-type interaction with the vacancy difficult [6,18].
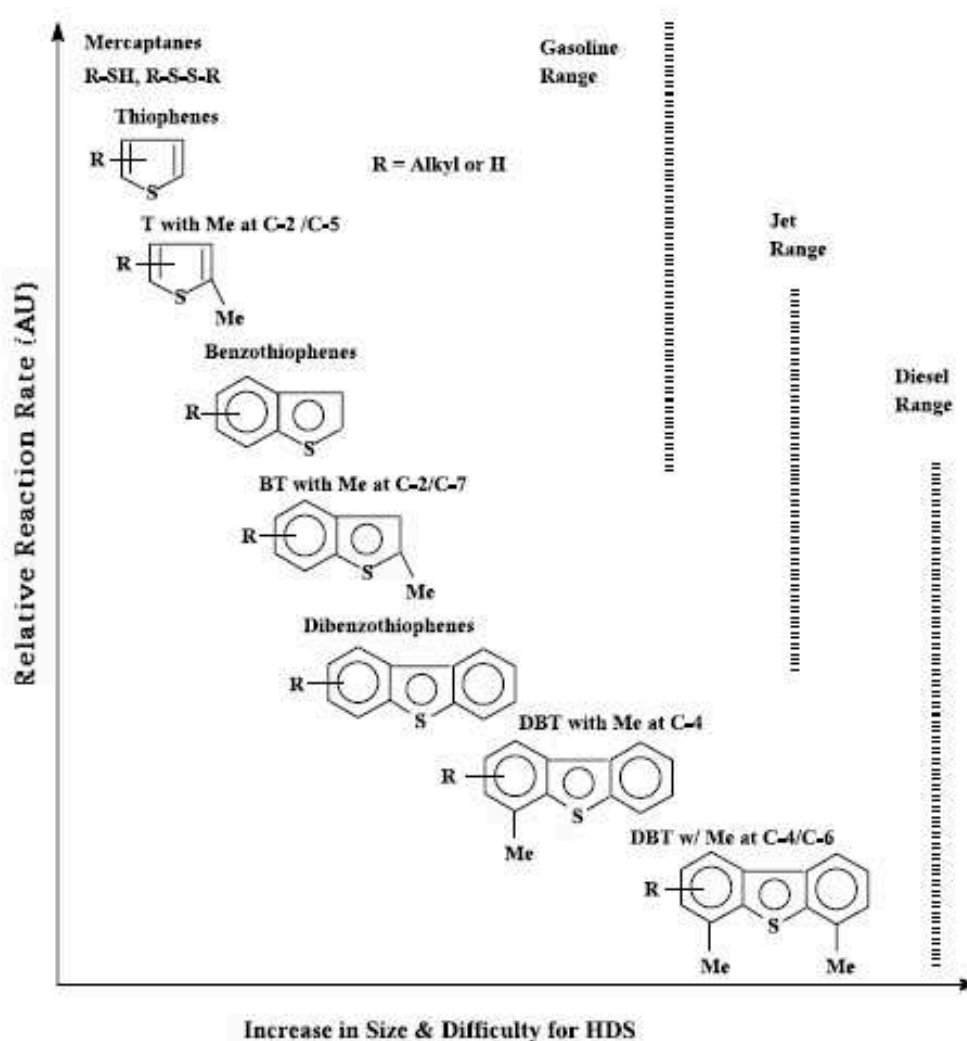
Fig. 2. Reactivity of various organic sulfur compounds in HDS versus their ring sizes and positions of alkyl substitutions on the ring [2].

8

It was found that DBT and 2,8-DMDBT transform preferentially via DDS pathway whereas 4-MDBT even more 4,6-DMDBT is transformed according to HYD pathway (**Scheme 2**) [17,19]. It is expected that HDS of alkyl-DBTs takes place predominantly by the HYD pathway via π-bonding of the reactant to the catalyst surface. In this case the alkyl substitutes do not create significant steric hindrance.
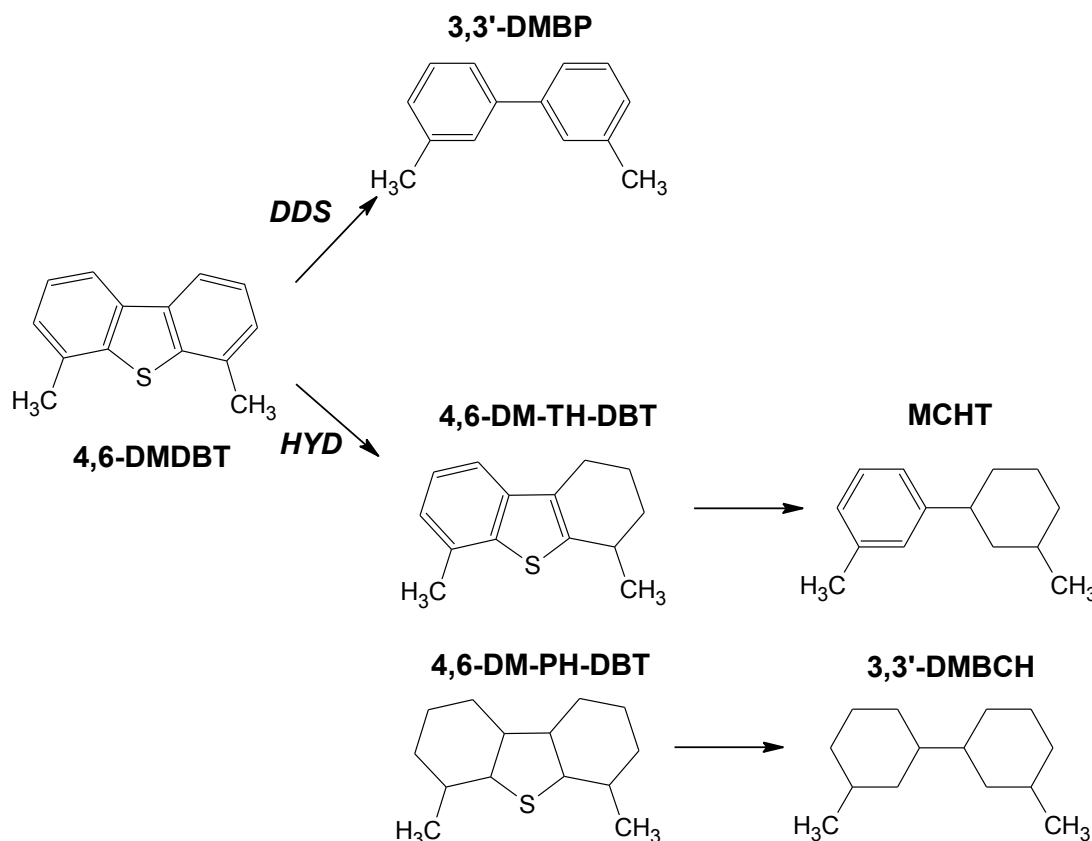
Scheme 2. Reaction network of the HDS of 4,6-DMDBT [14].

1.1.2.2 Kinetics of hydrodesulfurization reactions

Two types of kinetic models are commonly applied to express the rate of hydrodesulfurization and hydrodenitrogenation in a hydrotreating process. These models are the power law model and the Langmuir-Hinshelwood model.

A hydrotreating power law model often takes the following form:

$$-r_{\text{HDS}} = k_{\text{HDS}} \cdot C_S^n \cdot P_{H_2}^p, \qquad (1.1)$$

where r_{HDS} is the rate of change in the heteroatom concentration, k_{HDS} is the rate constant, C_S is the sulfur concentration, P_{H2} is the partial pressure of hydrogen, and n and p are the respective reaction orders of S concentration and H_2 pressure [20].

Because most real feedstocks for hydrotreating processes consist of many different compounds, it can be difficult to apply a single power law equation to represent the HDS rates. Langmuir-Hinshelwood models express the rate of decomposition of specific molecules for hydrotreating. The model takes into account the percentage of catalyst active sites that are occupied by the adsorbed reactant at steady state, as well the percentage of sites that are vacant or inhibited by other adsorbed compounds from the feed stream.

The Langmuir-Hinshelwood equation with two different types of active centers for the adsorption of DBT and H_2 is [3,6]

$$-r_{HDS} = k \frac{K_{DBT}C_{DBT}}{1+K_{DBT}C_{DBT} \cdot K_{H_2S}C_{H_2S}} \cdot \frac{K_{H_2}C_{H_2}}{1+K_{H_2}C_{H_2}}, \qquad (1.2)$$

where k is the rate constant for DBT HDS (mol/(g of catalyst s)), K_i is the adsorption equilibrium constant of DBT, H_2S and H_2 (kPa^{-1}), C_i is the coverage of DBT, H_2S and H_2 on catalyst surface (kPa).

When dealing with real feeds containing a wide range of sulfur, aromatics and nitrogen compounds, establishing rate equations for each type of compound would become tedious and quite complex. When this is the case, rate equation is often established resembling basic Langmuir-Hinshelwood model that represents the overall rate of HDS:

$$-r_{HDS} = \frac{k_{HDS} \cdot C_S^n}{[1+K_S C_S + K_A C_A + K_N C_N]}, \qquad (1.3)$$

where k_{HDS} is the apparent rate constant for DBT HDS (mol/(g·s)), K_i and C_i are the apparent adsorption equilibrium constant and bulk concentration of sulfur-, aromatic and nitrogen-containing compounds.

1.1.2.3. Inhibition effects of aromatics and nitrogen-containing compounds

The stringent environmental regulations limit the aromatic content in transport fuels. These can be divided into four categories: mono-, di-, tri-, and polycyclic aromatics (Fig. 3). The first three groups are more common in middle distillates, whereas the latter group dominates in the residuum fractions. Most of them are carcinogenic. Moreover, presence of aromatic compounds in the feed has an inhibiting effect on the reactivity of the refractory compounds [21].
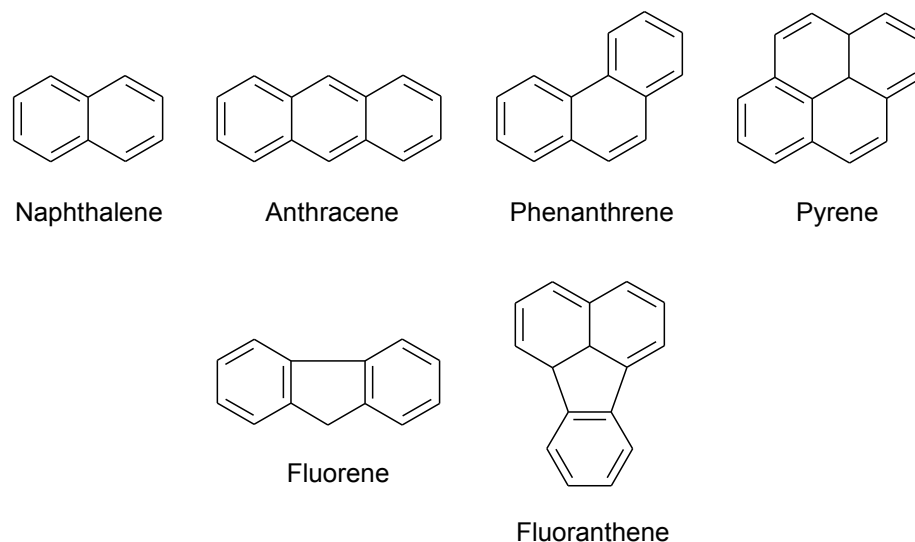
Fig. 3. Aromatic hydrocarbons [22].

The kinetic study showed that the rates of hydrogenation of subsequent rings tend to become lower and the hydrogenation of the last ring is the most complicated step of hydrogenation [23,24]. The hydrogenation rate decreases in the following order: Anthracene > naphthalene > phenanthrene > benzene.

Aromatic compounds are adsorbed on surface of the catalysts in flat mode through π-complex adsorption mechanism [22]. For deep desulfurization the aromatics may compete in the adsorption or reaction processes. However, the presence of alkyl substituents on the rings of aromatics hardly affects the strength of adsorption [25]. The reaction network of naphthalene hydrogenation is as follows:
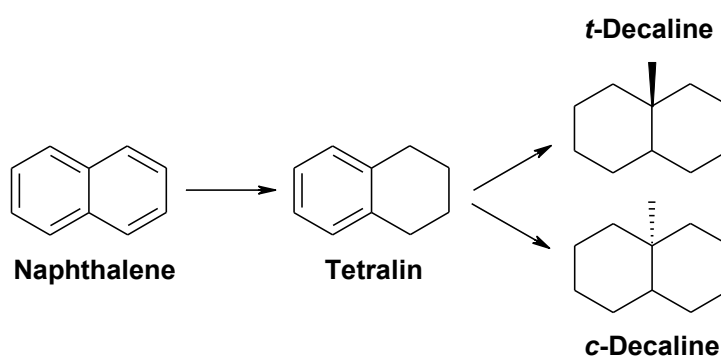
Scheme 3. Reaction network of the HYD of naphthalene.

Moreover, the catalytic hydrodesulfurization reactions are inhibited by nitrogen compounds due to suppression of hydrogenation functionality [21,26,27].

Most of the nitrogen is concentrated in fractions heavier than those containing sulfur and in the cracked fractions (Fig. 4). About a third of nitrogen compounds are present in the basic form containing the pyridine nucleus [6].
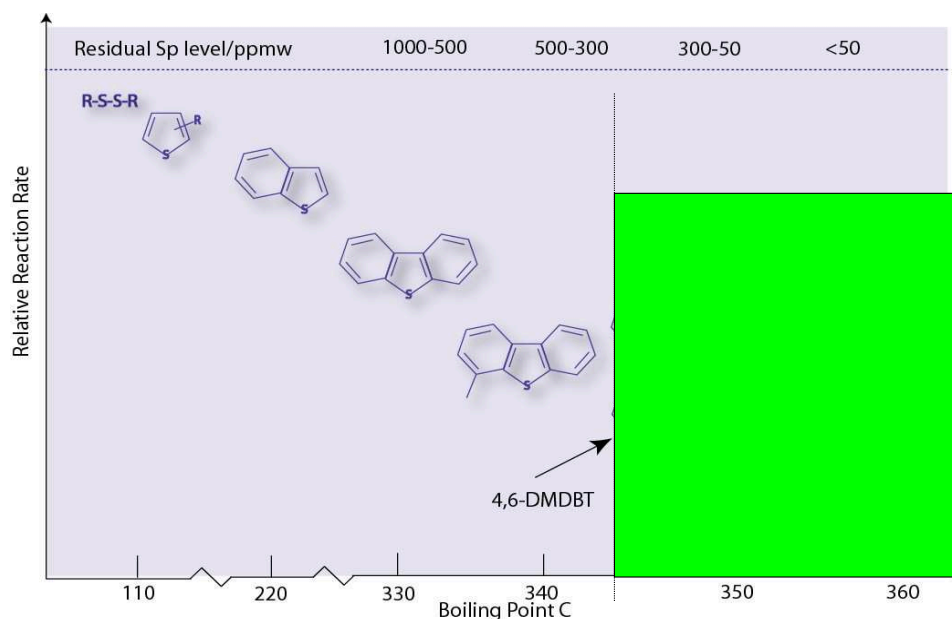
Fig. 4. N-containing compounds in oil cuts

It is known that nitrogen removal from heterocyclic organonitrogen compounds occurs via hydrogenation of the ring containing the heteroatom and then hydrogenolysis of the C-N bond. Hydrogenation of the hetero-ring is required to reduce the relatively large energy of the carbon-nitrogen bonds in such rings and thus allows easier carbon-nitrogen bond scission [22]. The quinoline reaction pathway is shown in Scheme 4. The adsorption strength of the N-compounds increases in the order ammonia < aniline <pyridine < piperidine, quinoline [28].
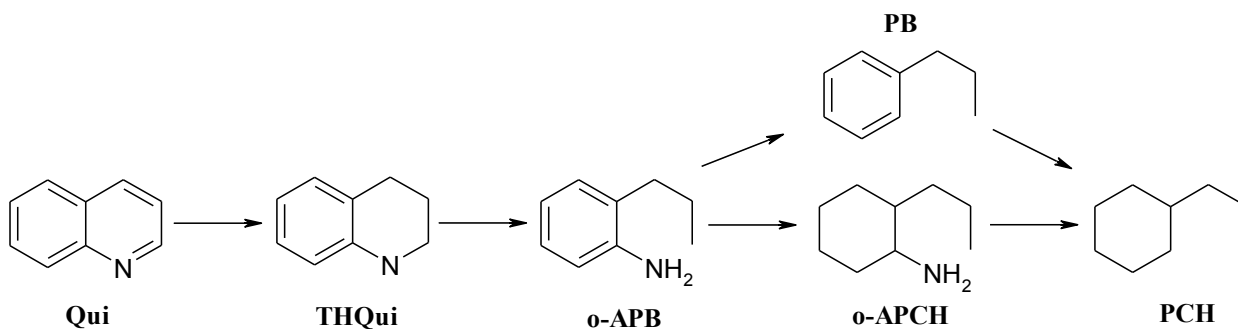
Scheme 4. Reaction network of the HDN of quinoline.

The nitrogen compounds have a strong inhibiting effect on HDS of 4-MDBT and 4,6-DMDBT even at low concentrations, e.g. 50 ppm, while the HDS of DBT remains nearly

unaffected by these compounds unless the concentrations are less than 500 ppm [29]. Similar results were obtained in [28], the influence of addition of quinoline on DBT HDS is shown in Fig. 5.
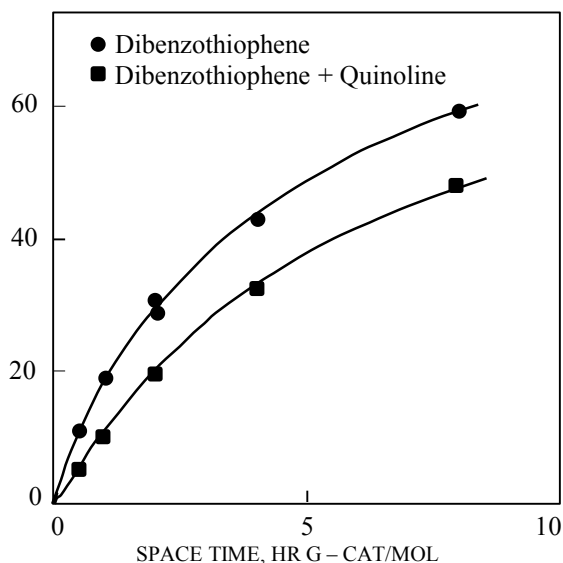
Fig. 5. At 360 ºC addition of quinoline moderately decreases the rate of hydrodesulfurization of dibenzothiophene on NiMo/Al$_2$O$_3$ catalyst [28].

Kwak et al. [29] found that the N-containing compounds suppress the prehydrogenation step more than the DDS ones in the HDS of DBT, while DDS is suppressed to a greater extent than HYD in the HDS of 4-MDBT or 4,6-DMDBT. The inhibiting effect of the nitrogen compound on the hydrodesulfurization reaction increases in the following order: carbazole< indole < quinoline [30,31].

Consequently, the suppression of inhibiting effect of the N-compounds is particularly important for deep hydrotreatment of refractory molecules with the steric hindrance around the sulfur atom.

1.2. Hydrotreating catalysts

1.2.1. On active phase and active sites of hydrotreating catalysts

It is known the active phases of unpromoted W (Mo) sulfide catalysts in hydrogenation and hydrogenolysis reactions are the coordinatively unsaturated sites located at the edges and corners of WS_2 (MoS_2) structures (Fig. 6).
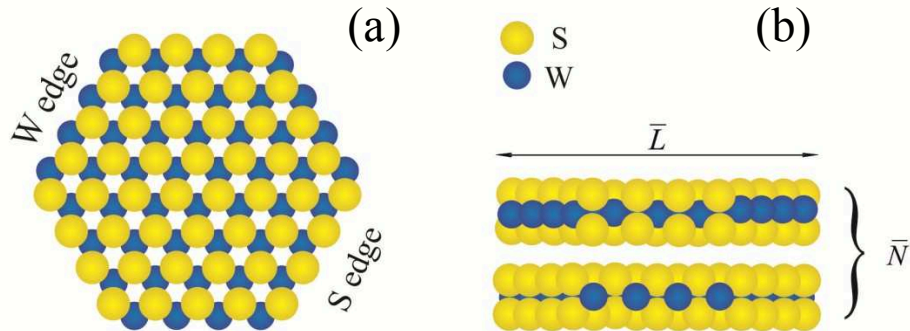
Fig. 6. Ball model of a WS_2: (a) top view and (b) side view.

To describe the structures of the active phases of Co(Ni)-promoted molybdenum catalysts several structural models were proposed [6,7,32,33]. According to "intercalation model" the WS_2 (MoS_2) structures consist of slabs, each of which comprises a plane of W (Mo) atoms sandwiched between two hexagonal, close-packed planes of S atoms. The promoter Co (Ni) ions occupy octahedral intercalation positions in the van der Waal's gap between the slabs. "Pseudointercalation model" is based on the structure of bulk MoS_2 with a prismatic arrangement of S atoms around each Mo. The promoter Co or Ni is intercalated in the octahedral holes between S-Mo-S layers at the crystallite edge. "The contact synergy model" based on results obtained for unsupported CoMo catalysts shows the presence of bulk Co_9S_8 and MoS_2. The promotional role of Co was associated to a contact between the two phases. This contact synergism is explained by spill-over of hydrogen from Co_9S_8 and MoS_2. At the present time, "Co-Mo-S model" is the most common model, the Co-Mo-S phase is MoS_2-like structures with the promoter atoms located at the edges of the S–Mo–S layers. The Ni-Mo/Al_2O_3 catalysts have behavior very similar to that of the Co-Mo/Al_2O_3 catalyst and show the presence of Ni-Mo-S phase, where Ni atoms are located at the edge positions of MoS_2 as well in "Co-Mo-S model"[34]. Two types of "Co-Mo-S type" phase with different catalytic properties were found depending on parameters of preparation and activation, type of support, presence of additives, etc. Type-I Co-Mo-S (Ni-Mo-S) is the single slab structures interacting strongly with the

support, via Mo-O-Al linkages located at the edges, which are difficult to sulfide completely. Type-II consists in the multiple slabs with weaker support interactions and higher sulfidation degree of metals. It is known Type-II structures have a higher catalytic activity than Type I. Nickel by analogy with cobalt can be present in three forms after sulfidation: as Ni_3S_2 crystallites on the support, as nickel atoms on the edges of MoS_2 crystallites (Ni–Mo–S phase), and as nickel cations Ni^{2+} in octahedral or tetrahedral sites in the γ -Al_2O_3 (Fig. 7).
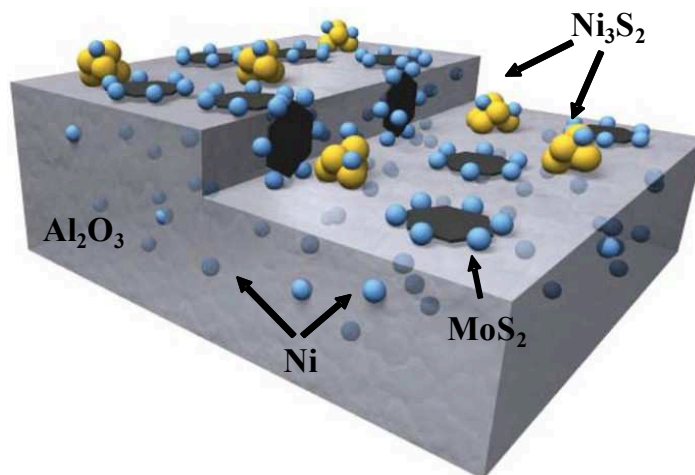
Fig. 7. Three forms of nickel sulfide species present in a sulfided Ni–Mo/Al_2O_3 catalyst [35].

Investigation of the morphological characteristics can help to understand HDS catalysts. High-resolution transmission electron microscopy (HRTEM) experiments allow to obtain images of S–Mo–S layers, which are oriented parallel to the electron beam, i.e. the layers are viewed as lines. Thus the active phase of HDT catalysts are observed in TEM images as small two-dimensional MoS_2 or WS_2 slabs dispersed on a support with a size depending on the carrier and loading. Considering that HDS and HYD reactions occur on edge sites, a geometrical model has been developed considering these particles with an hexagonal like shape [36]. Hereafter the morphology of the S–W–S (S–Mo–S) layers in MoS_2/C, WS_2/C, Ni–Mo–S/C and Ni–W–S/C catalysts was determined by the HAADF-STEM technique [37]. It was found that MoS_2 (WS_2) had using carbon supports the structure of truncated triangular while the addition promoter atoms modifies the shape to one closer to hexagonal (Fig. 8).

(b)
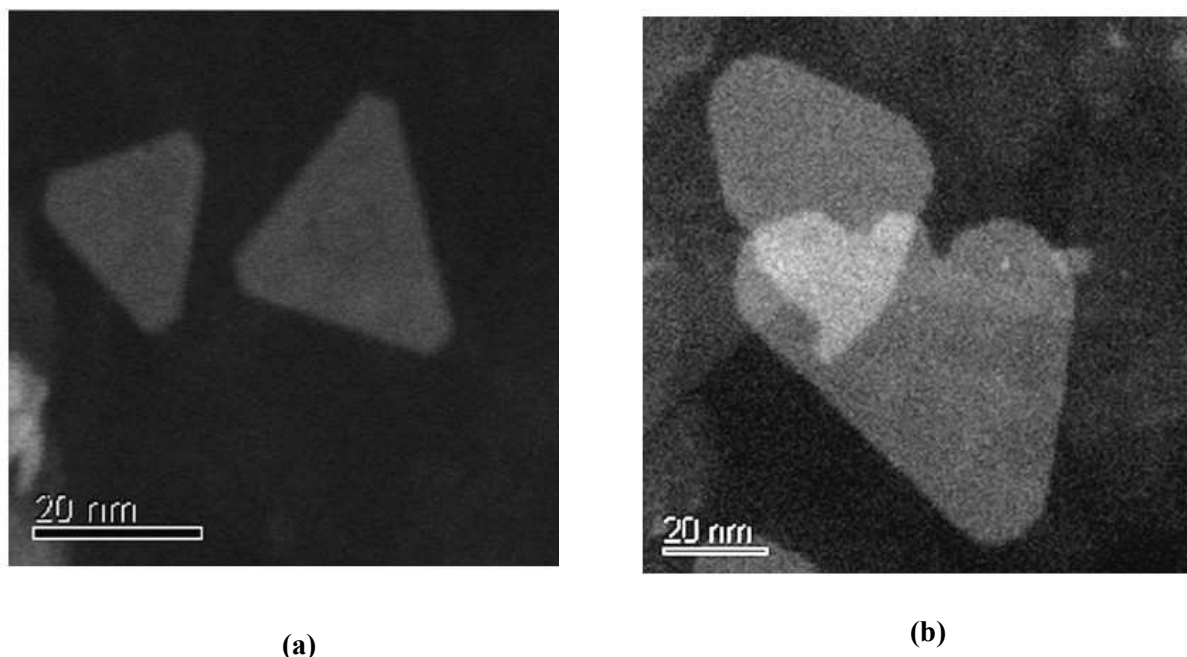
Fig. 8. HAADF-STEM image of WS$_2$ (a) and Ni-W-S clusters supported on a thin graphite support [37].

The influence of sulfiding temperature was studied by different techniques. It was found that high sulfidation temperature results to lateral growth of the crystallite and as a consequence, a decreasing in the relative amount of WS$_2$ (MoS$_2$) edge necessary for mixed site formation [38,39]. It is known that sulfidation of W is more difficult than Mo. Completely sulfided W species appear at temperature higher than 400 °C [38,40]. As high sulfidation temperature induces sintering of WS$_2$ slabs, utilization of high sulfidation pressure at lower temperature is preferred. However, the sulfidation of molybdenum and tungsten can be easier in the presence of promoter atoms (Ni, Co) which are sulfided first [41]. The strong conditions of W sulfidation also have influence on promotion ratio thus the optimal Ni/W ratio is higher that Ni/Mo ones [42,43].

1.2.2. Relations between active phase composition and catalytic properties

Toulhoat and Raybaud [44] reported that for HDT reactions the sulfur–metal bond energy is a relevant intrinsic property of the active phase to be correlated with activities. More precisely, the sulfur–metal bond energy, EMS, correlates well with the activity via a volcano curve (Fig. 9 (a)). Similar volcano relationship was first obtained empirically by Pecoraro and Chianelli [45] by correlating the HDS activity of DBT on bulk transition metal sulfides and the TMS experimental formation enthalpy.

(a)

(b)
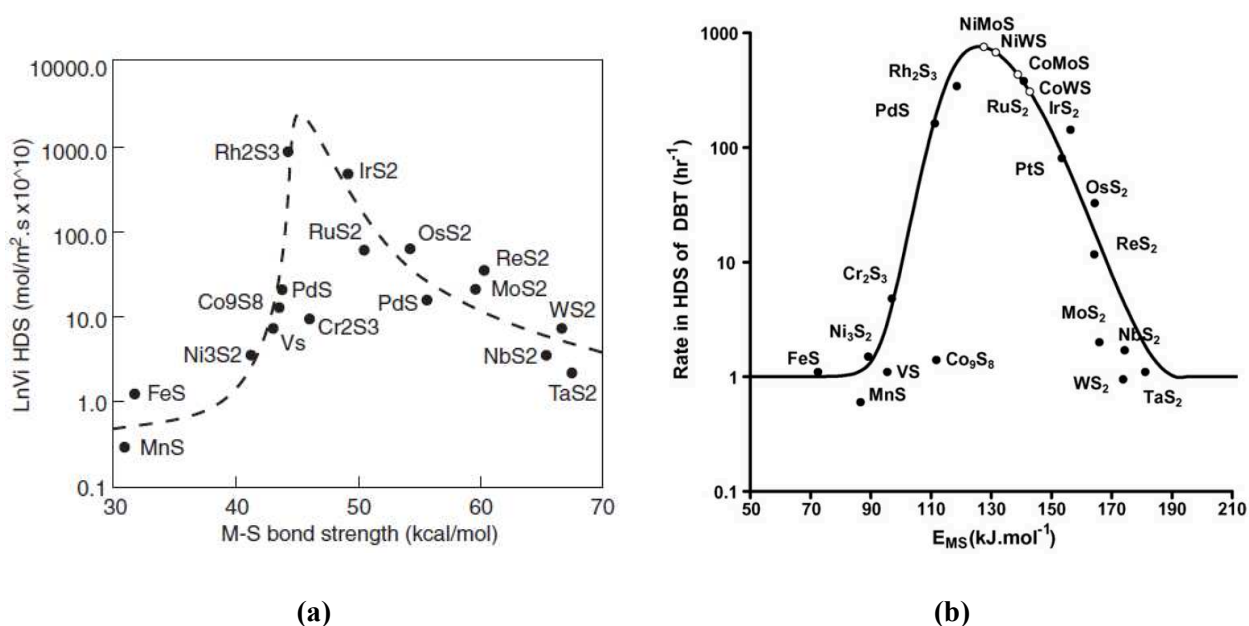
Fig. 9. HDS activity of the TMS vs. the bond strength of the transition metal sulfides **(a)** [46] and pattern of experimental activity (particle size corrected) for the HDS of DBT plotted against the computed EMS **(b)** [44]

Conventional hydrotreating catalysts, sulfided $Co(Ni)Mo(W)/Al_2O_3$, possess both HDS and HYD activities. Nonetheless, it has been established that CoMo catalysts exhibit higher activity in HDS reactions while NiMo is better in HDT of N-containing compounds [6,47]. NiW based catalysts have essential HYD activity, but lower HDS activity compared to Co(Ni)Mo systems, therefore, are being used less. Effect of catalysts composition to HDT activity is shown in Table 1 [48].

Table 1. Catalytic properties of HDT catalysts with the different composition.

Catalyst[1]	HDS	HYD of aromatics	HDN
$CoMo/Al_2O_3$	XXXX[2]	X	XX
$NiMo/Al_2O_3$	XXX	XX	XXX
NiW/Al_2O_3	XX	XXXX	XX

[1] sulfided catalysts with equal metal content

[2] activity: X – medium; XX – high; XXX – very high; XXXX – excellent.

The high hydrogenation activity of NiW catalysts has contributed to their application in hydrocracking processes [49]. In the HDT reactions, the hydrogenating properties of the

catalyst play a major role in the removal of the refractory compounds with steric hindrance around the sulfur atom, which are transformed according to a HYD pathway [50-52].

1.3. Mixed (Ni)MoWS catalysts

1.3.1 The reasons of usage of (Ni)MoWS$_2$ active phases in hydrotreating catalysis

The development of Ni(Co)Mo (STARS) and NiMoW (NEBuLA) bulk catalysts in the early 2000 allowed crossing over to a new level of activity of hydrotreating catalysts for production of ULSD (Fig. 10) [8,53]. The trimetallic NiMoWS bulk catalyst has at least three times higher activity than any other hydrotreating catalyst, conventionally used in industry [54].
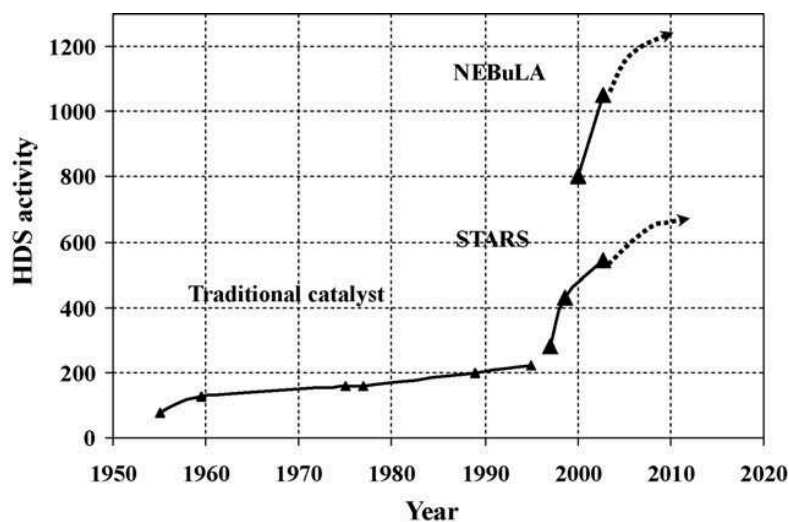
Fig. 10. Relative activity of the new STARS and NEBuLA catalysts compared to conventional CoMo/Al$_2$O$_3$ developed over the last 50 years [3].

Later, Raybaud and co-workers [9] predicted a synergetic effect of NiMoW active phase. The investigation based on hydrodesulfuration (HDS) of thiophene and density functional theory (DFT) calculations showed a new synergy effect of Ni promoted $Mo_{1-x}W_xS_2$ solid solution. $NiMo_{0.5}W_{0.5}S_2$ catalyst demonstrated higher HDS activity than NiMoS and NiWS (Fig. 10). In contrast, the HDS activity of $CoMo_{0.5}W_{0.5}S_2$ catalyst results from the linear combination of the activities of the two CoWS and CoMoS references due to the too high the sulfur metal bond energy value.
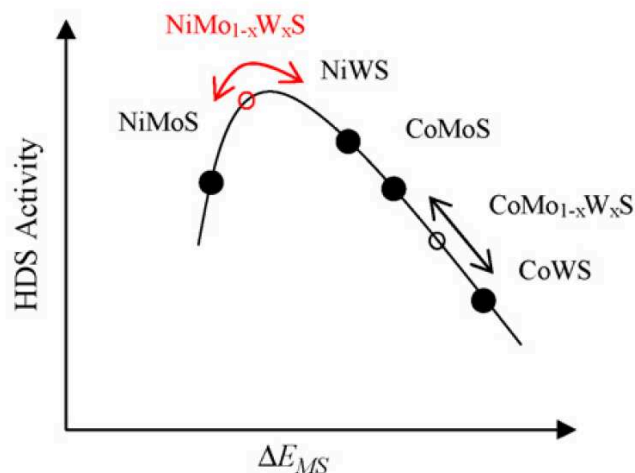
Fig. 10. Schematic representation of the relative positions of the Co(Ni)MoWS systems on the volcano curve and explanation of the new synergy effects for NiMoWS systems [9].

Moreover, Olivas et al. [10] also described the higher synergistic effect of Ni in $(Mo-W)S_2$ compared to $Ni(MoS_2)$ and $Ni(WS_2)$ separated bulk catalysts. The authors based on Extended Hückel calculations explained the high catalytic activity of trimetallic sample in dibenzothiophene (DBT) HDS due to the formation of the Ni-Mo-W-S phase after sulfidation, resulting increase the availability of electrons over the Fermi level and the metallic character of the catalysts.

1.3.2. From bulk to supported (Ni)MoWS catalysts: Preparation methods and achieved results

Table 2 summarizes the types of investigated trimetallic NiMoWS bulk and supported catalysts and their catalytic properties. Some detail of the preparation of NiMoW catalysts and their catalytic activity will be discussed below.

There are several ways to prepare unsupported HDS catalysts. The most commonly used methods of preparation NiMoW bulk catalysts described in the literature are (co)-precipitation [54-58] and thiosalts decomposition.

Thiosalt decomposition is a method for obtaining $Mo(W)S_2$ catalysts with controlled stoichiometry. Moreover, these thiosalts have already sulfur bound to the metal atoms in a tetrahedral coordination which can be kept after decomposition [59]. The catalyst precursors can be decomposed by ex situ [60-64] or in situ methods [61,65,66].

Despite that trimetallic Ni–Mo–W sulfide catalysts have a potential advantage over bimetallic Ni-Mo(W) systems, in respect to deep sulfur and nitrogen removal, no clear explanation of their higher activity has yet been proposed. One explanation is the formation of mixed NiMoWS active phase, however, For mixed MoW systems there are four possible structural models:

1. homogeneous MoS_2 and WS_2 slabs are stacked to each other (interlayer solid solution);

2. both Mo and W atoms can be present in each slab resulting in $MoWS_2$ (intralayer solid solution);

3. $MoWS_2$ phase is the result of randomly distributed homogeneous MoS_2/WS_2 slabs and mixed $MoWS_2$ ones;

4. separate MoS_2 and WS_2 particles can be form.

Nevertheless, the difference between inter- or intralayer solid solutions cannot be determined by X-ray diffraction (XRD), energy dispersive X-ray spectroscopy (EDXS), IR- or Raman spectroscopy, only a local method such as EXAFS can provide relevant information [67].

If the structures of active phases of bimetallic Ni(Co)-Mo(W) and their catalytic properties were thoroughly investigated, the question are still remain about the reasons of high catalytic activity of trimetallic Ni-Mo-W.

Unsupported WMoS compounds as an interlayer solid solution were synthesized by co-crystallization from aqueous solution of ammonium tetrathiomolybdate and ammonium tetrathiotungstate [68]. EXAFS results showed the presence of second contribution with

heteroatom in second coordination shell. Authors also marked importance of the nature of starting precursor and concluded that the solid solution can be prepared only with a precursor in which the two cations are closely associated. This approach was further used for preparation of alumina supported $Mo_{0.50}W_{0.50}S_2$ and $Ni-Mo_{0.50}W_{0.50}S_2$ catalysts. In both cases the second coordination shells demonstrated the presence of both molybdenum and tungsten atoms. It was confirmed that the intralayer solid solution structure is retained in the supported samples [67].

Hereafter, Licea et al. [69] reported the EXAFS results for unsupported Ni(Co)MoW catalysts which consisted of nickel sulphide domains and $Mo_{1-x}W_xS_2$ solid solutions. However, the trimetallic catalysts exhibited lower catalytic activity compare to NiMo catalyst. The catalytic activity and selectivity of these systems was associated with the the nature of the promoters and not with the group VI elements.

Wang with co-workers [58] developed bulk NiMoW HDS catalyst with a unique multilayered structure, in which the Ni_7S_6 species with layered structure act as a support for Mo, W, or MoW sulfide particles (Fig. 11). The precursor was prepared by means of a surfactant-assisted co-precipitation method from ammonium molybdate, ammonium metatungstate, and nickel carbonate. Based on a combination of XRD and EXAFS of oxidic precursor the authors confirmed the formation of nickel species with multilayer structure and proposed the preservation of this structure after sulfidation. Prepared NiMoW catalyst exhibited a much higher HDS performance than that of the commercial $CoNiMoW/Al_2O_3$ catalyst in the HDS of actual diesel.

ion-exchange with $Mo_7O_{24}^{6-}$ and $H_2W_{12}O_{40}^{6-}$

hydrotalcite-like nickel species

sulfidation with 10% H_2S/H_2

layered sheet of Ni species

MoW species

CO_3^{2-} or OH^-

MoS_2, WS_2 or $MoWS_2$ species

bulk Ni_7S_6

sulfide catalyst with multilayered structure
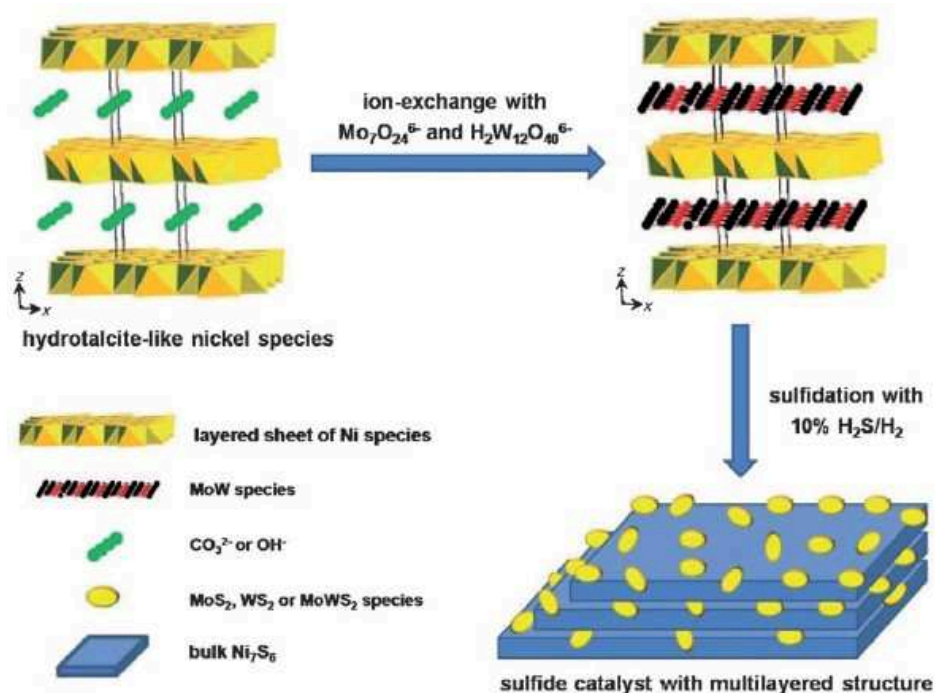
Fig. 11. Formation of the NiMoW sulfide catalyst with multilayered structure [58].

Interlayer $MoWS_2$ phase was found in unsupported NiMoW prepared by co-precipitation in aqueous solution of ammonium heptamolybdate (AHM), ammonium metatungstate (AMT) and Ni nitrate [70]. The presence of Mo and W and Ni-metal (metal-Ni) contribution in the same slab was confirmed by EXAFS. Additionally, it was observed that a substantial fraction of NiS_x consists of very small clusters or atomically dispersed Ni.

Two main components of hydrotreating catalysts are active metals and support. It is widely known the most effectively HDT catalysts contain metals in active sites Type II Ni(Co)-Mo-S. The concentration of these sites indicates the level of catalytic activity and therefore development of the catalysts with maximum concentration of Type II sites is actual task. The principal preparation method of supported HDT catalysts is the pore volume impregnation of support with an aqueous solution of metals salts with subsequent drying and calcination. The final step of synthesis of the catalysts is their activation by sulfidation. Improvement of each from these steps can result to increase of the catalytic activity.

It is now known that one of the main factors that affect catalyst activity is the interaction between the active components and the support. Metal–support interactions influence not only the dispersion of the active species, but also their reducibility and sulfidability. Alumina presents a strong metal-support interaction and therefore sulfidation of the active phases must be well asserted [71].

The difference between the morphologies of the sulfided catalysts would have a significant impact on the catalytic activity. The trimetallic supported NiMoW catalysts showed, generally, a better dispersion of Mo and W sulfides than in the corresponding bimetallic formulations: only short particles formed more high layers. The strong metal-support interaction in Mo(W)/Al hinders sintering of the MoS_2 or WS_2 slabs, resulting in a dispersed $Mo(W)S_2$ phase [72].

The influence of phosphorus addition to $NiMoW/Al_2O_3$ sulfide catalysts was studied [73,74]. It was found that P addition to NiMoW improved the dispersion of Mo and W species on alumina. P-doped trimetallic catalyst showed better hydrotreating activity compare to bimetallic and trimetallic systems without P.

The surfaces of NiMoW catalysts supported on Al-Ti-Mg were analyzed using DFT and tested in DBT HDS [75]. The authors observed a direct correlation between the calculated surface energies and catalytic activity. It was found that the incorporation of promoter (Ni) to Mo and W edges in the active surface sites resulted in an increase of surface energy while NiMoW catalyst had a lower surface energy than those of the bimetallic ones. The authors

suppose that the presence of Ni causes an elongation of the Mo(W)-S bond lengths, leading to fully substituted Mo(W)-edges and as a consequence increased catalytic activity.

The genesis of the active phase in trimetallic $NiMo_xW_{(1-x)}/Al_2O_3$ catalysts depending on sulfidation conditions was investigated by Hensen with co-workers [11]. The samples were sulfided in a flow of H_2/H_2S (10% H_2S) at a pressure of 1 or 15 bar. It was found that the presence of Mo did not affect the sulfidation of W due to higher sulfidation rate of molybdenum than that of tungsten. It was observed that sulfidation at atmospheric pressure and 400 °C led to the formation of NiMoW particles with a core−shell structure, where Mo was mostly located in the core and W in the shell. (Fig. 12 (b)) Increase of sulfidation pressure to 15 bar resulted in the formation of homogeneous $MoWS_2$ particles. In this case tungsten was sulfided at lower temperature, around the temperature of MoS_2 formation, consequently, a larger fraction of W was incorporated into the MoS_2 phase. High sulfidation temperature also led to a more homogeneous distribution of both metal in the $MoWS_2$ particles (Fig. 12 (a)). Authors explained this fact by the particle size. The sintering of particles at high temperature gives rise to formation of larger particles which did not retain the core−shell structure. Results of examination of catalytic activity showed that the samples with a core−shell structure demonstrated higher activity in thiophene HDS (1 atm), whereas a homogeneously mixed phase catalyzed the HDS of DBT at 40 bar.

(a)   **(b)**
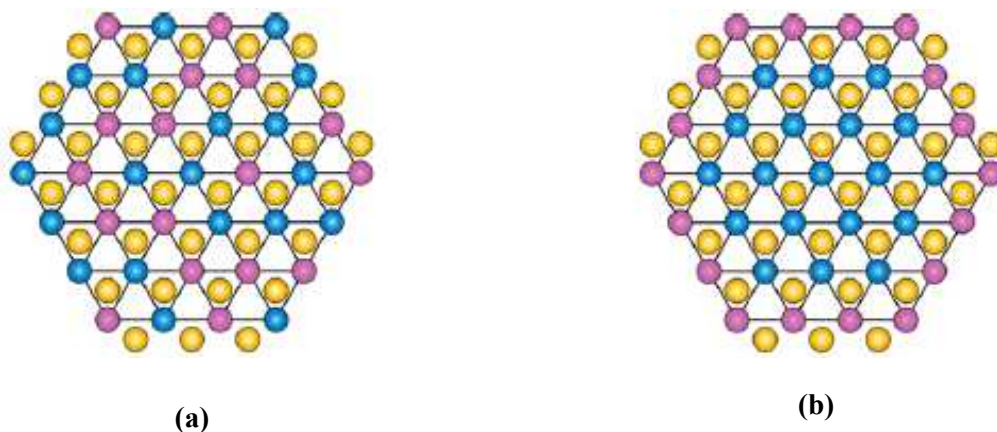
Fig. 12. The structures of the active phase in $NiMo_xW_{(1-x)}/Al_2O_3$ catalysts ($x \leq 1$): randomly mixed $MoWS_2$ particles **(a)** and mixed $MoWS_2$ particles with a two-dimensional core−shell structure **(b)**. Color scheme: S (yellow); Mo (blue); W (pink) [11].

As can be seen from the above, further studying of trimetallic NiMoW catalysts is necessary to understand how structural and morphological changes give rise to changes in the catalytic activity.

Table 2. Types of trimetallic NiMoWS bulk and supported catalysts and their catalytic properties

| Catalyst type | Precursors | | | | | Catalytic activity | |
	Ni	Mo	W	Modifier	Reactants	Synergy compare to bimetallic NiMo(W) catalysts	Refs.
				Unsupported NiMoW catalysts			
NiMoW	Industrial catalyst			-	Diesel, vacuum gas oil, light gas oil and coking gas oil	+	[8,53].
NH_4-Ni-Mo_{1-x}-W_x-O	$Ni(NO_3)_2$	$(NH_4)_2MoO_4$	$(NH_4)_6H_2W_{12}O_{40}$	-	DBT	+	[55,76]
NH_4-Ni-$Mo_{05}W_{05}$-O	$Ni(NO_3)_2$	$(NH_4)_2MoO_4$	$(NH_4)_6H_2W_{12}O_{40}$	-	DBT	n/a*	[54]
NiMoW	$Ni(NO_3)_2$	$(NH_4)_6Mo_7O_{24}$	$(NH_4)_6H_2W_{12}O_{40}$	-	DBT	+	[62]
	$Ni(NO_3)_2$	$(NH_4)_6Mo_7O_{24}$	$(NH_4)_6H_2W_{12}O_{40}$	-	FCC gas oil, coking gas oil	+	[56]
	$Ni(NO_3)_2$	$(NH_4)_6Mo_7O_{24}$	$(NH_4)_6H_2W_{12}O_{40}$	-	DBT	+	[10]
	$NiCO_3$	$(NH_4)_6Mo_7O_{24}$	$(NH_4)_6H_2W_{12}O_{40}$	-	4,6-DMDBT, straight-run diesel	+	[58]
	$NiSO_4$	$(NH_4)_6Mo_7O_{24}$	$(NH_4)_6H_2W_{12}O_{40}$	-	DBT	n/a	[77,78]
	$Ni(NO_3)_2$	$(NH_4)_6Mo_7O_{24}$	$(NH_4)_6H_2W_{12}O_{40}$	-	Thiophene, 4,6-DMDBT, straight-run gas oil	n/a	[79]
NiMoW	$NiCl_2$	$(NH_4)_2MoS_4$	$(NH_4)_2WS_4$	-	DBT	n/a	[65]
NiMoW	$Ni(NO_3)_2$	$(NH_4)_2MoS_4$	$(NH_4)_2WS_4$	-	DBT	n/a	[60,61,63,64]
NiMoW	$NiCO_3$	$(NH_4)_2MoS_4$	$(NH_4)_2WS_4$	-	FCC diesel oil	n/a	[72]
				Supported NiMoW catalysts			
NiMoW/alumina	Industrial catalyst			-	Residual oil	+	[80]
NiMoW/alumina	$Ni(NO_3)_2$	$(NH_4)_6Mo_7O_{24}$	$(NH_4)_6H_2W_{12}O_{40}$	-	Naphthalene	+/-	[81]
NiMoW/alumina	$Ni(NO_3)_2$	$(NH_4)_2MoO_4$	$(NH_4)_6H_2W_{12}O_{40}$	-	Various feedstocks	+	[82]
NiMoW/alumina	$Ni(NO_3)_2$	$(NH_4)_6Mo_7O_{24}$	$(NH_4)_{10}H_2(W_2O_7)_6$	-	Coker light gas oil	+	[73]
NiMoW/alumina	Iindustrial catalyst			-	Diesel cut	+	[83]
NiMoW/alumina	$Ni(NO_3)_2$	$(NH_4)_6Mo_7O_{24}$	$(NH_4)_6H_2W_{12}O_{40}$	$Ni(H_2PO_2)_2$	DBT, FCC diesel oil	+	[74]

NiMoW/alumina	$Ni(NO_3)_2$	$(NH_4)_2MoS_4$	$(NH_4)_2WS_4$	-	FCC diesel oil	n/a	[72].
NiMoW/SiO$_2$	$Ni(NO_3)_2$	$(NH_4)_2MoO_4$	$(NH_4)_6H_2W_{12}O_{40}$	-	DBT	+	[84]
NiMoW/SBA-15	$Ni(NO_3)_2$	$(NH_4)_6Mo_7O_{24}$	$(NH_4)_6H_2W_{12}O_{40}$	citric acid	DBT, 4,6-DMDBT	+	[85]
NiMoW/SBA-15 NiMoW/alumina	$Ni(NO_3)_2$	$(NH_4)_6Mo_7O_{24}$	$(NH_4)_6H_2W_{12}O_{40}$	citric acid	DBT	n/a	[86]
NiMoW/(P)-SBA-16	$Ni(NO_3)_2$	$(NH_4)_6Mo_7O_{24}$	$(NH_4)_6H_2W_{12}O_{40}$	-	DBT, 4,6-DMDBT	n/a	[87]
NiMoW/Al-HMS	$Ni(NO_3)_2$	$(NH_4)_6Mo_7O_{24}$	$(NH_4)_6H_2W_{12}O_{40}$	-	DBT	+	[88]
NiMoW/Al-Ti-Mg	$Ni(NO_3)_2$	$(NH_4)_2MoS_4$	$(NH_4)_2WS_4$	-	DBT	+	[75]
NiMoW/alumina	$Ni(NO_3)_2$	$(NH_4)_6Mo_7O_{24}$	$(NH_4)_6H_2W_{12}O_{40}$	-	Thiophene, straight run gas oil	+	[9]
NiMoW/alumina	$NiCO_3$	PMo_{12} HPA	PW_{12} HPA	citric acid	Straight run diesel, light gas oil of catalytic cracking	+	[89]
NiMoW/alumina	$Ni(NO_3)_2$	$(NH_4)_6Mo_7O_{24}$	$(NH_4)_6H_2W_{12}O_{40}$	-	Thiophene, DBT, Gas-Oil	+/-	[11]
NiMoW/alumina	$Ni(NO_3)_2$	$(NH_4)_6Mo_7O_{24}$	$(NH_4)_6H_2W_{12}O_{40}$	-	o-propylaniline, dimethyl disulfide, DBT	+	[70]
NiMoW/USY zeolite	$NiCO_3$	$(NH_4)_6Mo_7O_{24}$	$(NH_4)_6H_2W_{12}O_{40}$	-	4,6-DMDBT	n/a	[90]
NiMoWAl	NiAl-terephthalate	$(NH_4)_6Mo_7O_{24}$	$(NH_4)_6H_2W_{12}O_{40}$	-	DBT, Tetrahydronaphthalene	-	[91]
WMo(Ni)/alumina	$Ni(NO_3)_2$	Mo-based hybrid inorganic–organic nanocrystals	W- based hybrid inorganic–organic nanocrystals	-	DBT, FCC diesel	+	[92]

1.4. Advanced Characterizations: XAS and HAADF

The investigation of the exact structure of the HDS catalysts active sites could benefit from the use of advanced characterization techniques as X-Ray Absorption Spectroscopy (XAS) and HAADF.

The structural characterization of systems as nano-disulfide slabs (around 3 nm) without long-range order is complicated for common techniques however, microcrystalline or amorphous species can be studied by EXAFS, which as a result has gained widespread use in studies of catalysts. This technique allows to obtain the detailed information about the environment of the probed atoms (number of neighbors and distances). In addition, EXAFS studies can conveniently be carried out under realistic reaction conditions (sulfidation conditions under H_2 and H_2S mixture), thus enabling a structural description of the working catalyst. Using the *in situ* XAS technique, Clausen et al. [6,93] showed that, in typical sulfided Mo/Al_2O_3 catalysts, the Mo atoms are predominantly present as MoS_2-like structures. No significant differences in the Mo structures were found between unpromoted and promoted catalysts, suggesting that the Mo phases in the two systems are basically identical. EXAFS studies allowed to determine the Co(Ni)-S distance (2.21 Å) [6,94-97], that is much shorter than the Mo-S distance in bulk MoS_2 (2.41 Å). This indicates that although the promoter atoms are located in the Mo plane of the S-Mo-S slab, the Co and Ni atoms do not occupy perfect edge substitutional Mo positions but are relaxed in towards the S (and Mo) atoms [6, 98,99]. The EXAFS results, which indicate a Co-Mo distance of about 2.85 Å [100] and a Ni-Mo distance of about 2.86 Å [101-103] are also in support of this, since a perfect edge substitutional Mo position would yield a distance of 3.16 Å. For XAS experiments, the development of new beamline allowing quick-EXAFS and then time resolved experiments allows now to follow the sulfidation process of metallic atoms of the catalysts. Indeed, the sulfidation mechanism of supported NiW [35,43], NiW/Al_2O_3–F [104], $NiMo/Al_2O_3$ [105], $NiMo/SiO_2$ [106], $NiMoW/Al_2O_3$ [11,10], Co–Mo/B_2O_3/Al_2O_3 [107], $CoMo/Al_2O_3$ [108,109] hydrotreating catalysts was studied using *in situ* XAS characterization.

HAADF is also a powerful technique for characterization of the sulfided catalysts recently developed. HAADF-STEM studies have provided detailed morphological insight regarding nanostructures of sulfided active phase. Thus, the differences in the morphology of the MoS_2 and Co(Ni)–Mo–S nanoparticles supported on carbon and sulfided at 800 °C were found by HAADF-STEM studies [37]. The unpromoted MoS_2 structures, we find that the predominant shape is a truncated hexagon, while the promotion changes the morphology of the nanoclusters and that their shape becomes significantly more hexagonal. Moreover, the Ångstrom resolution

of this tool allows estimating the distributions of metal atoms in slabs [18,70,111,112]. This technique allows the catalytically active edges sulfide structures to be imaged [37]. The current approach also allows to study the effects of the nature of the active metal precursors, to estimate the influence of different sulfiding agents on the morphology of the catalytic nanostructures, which, in turn will help to choice of preparation and sulfidation conditions.

1.5. Heteropolyanions as effective precursors of hydrotreating catalysts

Industrially preparation methods of HDT catalysts are based on the sulfidation of an oxidic precursor that is generally prepared by incipient wetness impregnation of an alumina support. The most commonly used oxide precursors are ammonium heptamolybdate $(NH_4)_6Mo_7O_{24}$ (AHM), ammonium metatungstate $(NH_4)_6H_2W_{12}O_{40}$ (AMT) and cobalt or nickel nitrate [9,73,86-88]. After impregnation obtained solids are dried and calcined in order to mainly remove water and the nitrate and ammonium counterions present in these conventional preparations.

Nowadays heteropolycompounds (HPCs) as starting oxidic precursor of an active phase of HDS catalysts with improvement of the catalytic properties attract special attention of researchers [113-128]. Heteropolyanions are a large group of complex inorganic compounds, which composition can be described as an assembly of oxygen polyhedra (octahedra and tetrahedra) of limited extent obtained by sharing one or more oxo (or hydroxo) ligands, the polyhedra being joined at their corners, edges or faces [129].

Heteropolyanions salts with Keggin $[XM_{12}O_{40}]^{n-}$(Fig.13 (b)), Anderson $[XM_6O_{24}H_6]^{n-}$ (Fig.13 (a)) and its dimeric structures (Fig. 13 (c)) are more frequently used as alternatives to classical AHM and AMT precursors. The main advantage of HPCs of Anderson type is the presence of a 3d-metal (Ni and Co included) as a heteroatom in heteropolyanion. The proximity of atoms in starting material results to synergetic effect between the atoms of the promoter and the main active compound [130]. Moreover, HPCs structure produces a good adsorptive interaction with the support and a uniform distribution of active sites on the catalysts surface [121]. The ammonium salts of heteropolyanion have several advantages over conventional precursors because they can be employed not only in solution to impregnate supports, but also in solid state as starting materials for the formation of bimetallic oxides [122]. Catalytic activity strongly depends on the nature of HPCs used for the preparation of the oxide precursors.

$[Al(OH)_6Mo_6O_{18}]^{3-}$ $[PMo_{12}O_{40}]^{3-}$ $[Co_2Mo_{10}O_{38}H_4]^{6-}$ $[P_2Mo_5O_{23}]^{6-}$

(a)   **(b)**   **(c)**   **(d)**
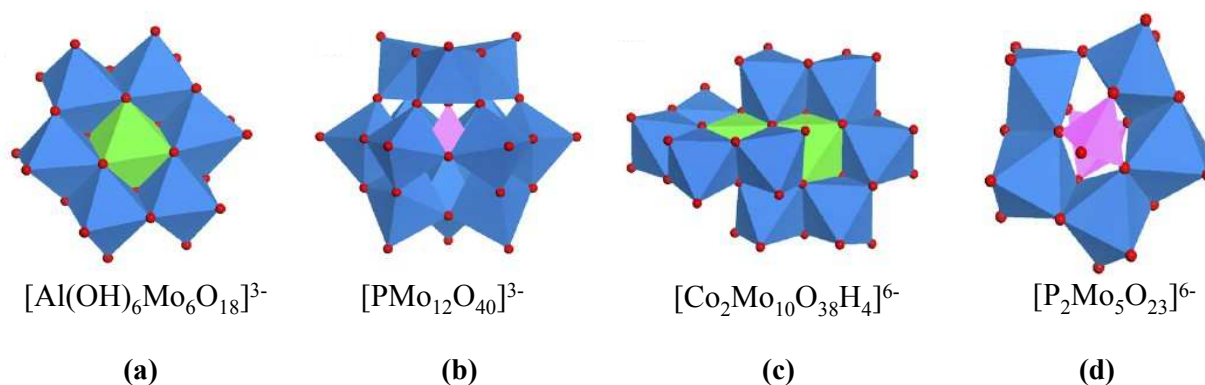
Fig. 13. The most commonly used heteropolyanions for a synthesis of HDT catalysts. Color scheme: Mo (blue); O (red); P (pink); Co (green).

Thus, the use of HPCs with higher Co/Mo ratio than in Anderson type XMo_6HPA leads to enhance of the promoting effect of the cobalt in the HDS reactions [117,119,125,126,131,132]. The advantage of the catalysts prepared from Co (Ni) salts of HPAs has been established in [125,126,131,133], these samples are more effective than the samples synthesized from ammonium salts with cobalt (nickel) nitrate by conventional methods.

Keggin type heteropolyanion (HPA) and its derivatives (Fig. 13 b) are the most stable, accessible and important for catalysis [134-136]. The Keggin type heteropolyanion with general formula $XM_{12}O_{40}^{n-}$, where M is transition metal atom (Mo^{VI}, W^{VI}, V^V) in oxygen environment and X a non-metallic atom (Si^{IV}, P^V, Ge^{IV}, As^V, etc.) consists in a regular XO_4 tetrahedron surrounded by 12 MO_6 octahedra, which are connected by shared edges to form trimetallic M_3O_{13} groups joined together by their vertices [137]. Depending on the synthesis conditions, various isomers (α, β) can be isolated. Four different types of oxygen atoms are present in this structure: 4 oxygen atoms (O_a) common to the central tetrahedron and to the three octahedra of a single M_3O_{13} group; 12 oxygen atoms (O_b) common to the octahedra of two different M_3O_{13} groups; 12 oxygen atoms (O_c) common to the octahedral of a single M_3O_{13} group; 12 oxygen atoms (O_d) linked to a single metal atom (Fig. 14) [129].
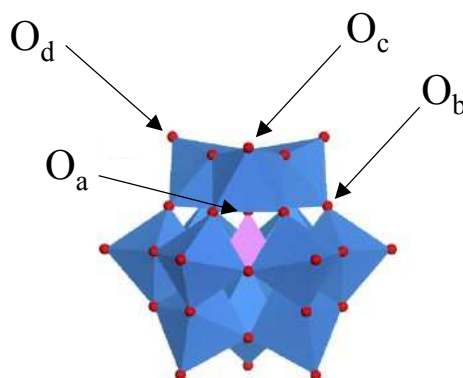
Fig. 14. Keggin type heteropolyanion (α isomer).

The "lacunary" Keggin structure corresponds to a Keggin structure, in which one or more sites previously occupied by molybdenum or tungsten atoms are vacated. This new family corresponds to an M/X ratio of 11 obtained by extracting one atom [137,138] or 9 [139,140], obtained by extracting three metal atoms from different M_3O_{13} groups. These monovacant or polyvacant heteropolyanions can be synthesized directly depending on the medium pH. It is also possible to prepare substituted derivatives, in which one or more metal atoms (Mo, W, etc.) of the dodeca-condensed structure are replaced by different atoms. Substitution can take place with an element whose oxidation number is much lower than that of the metal atom it is replacing (e.g. Co^{II}, Ni^{II}, Fe^{III}) [134,141] or with an element that can have similar properties to that of the substituted atom, as with vanadium-V in the case of the acid $H_4PMo_{11}VO_{40}$ [142].

However, due to low specific surface area (1-5 m^2 g^{-1}) supported HPAs have been most widely applied. In the field of hydrotreatment catalysis, Keggin and Keggin-derivated heteropolymolybdate and heteropolytungstate structures have been successfully used to replace conventional precursors. Thus, Ni promoted molybdenum and tungsten HPA-based catalysts showed better performance in deep HDS of 4,6-DMDBT [143] and diesel hydrotreating [144] than the counterparts prepared from traditionally used Mo (W) ammonium salts. The use of NiW Keggin type HPA with a different Ni/W ratio as precursors of hydrocracking catalysts was reported in [145]. In was reported that $CoMo/Al_2O_3$ catalysts obtained from cobalt salts of PMo_{12} HPA were more efficient than those prepared from AHM and H_3PO_4 due to a better metal dispersion and the absence of ammonium counterions. [117]. No influence of heteroatom nature of $SiMo_{12}$ and PMo_{12} HPAs on the thiophene conversion was hound in [146].

Simultaneous use of Keggin HPAs and Co(Ni)-chelates for the preparation of HDT catalysts was investigated in several studies [147-150].

From a catalytic point of view, the use of mixed metals Keggin-type HPAs may enhance activity due to the introduction of a second metal in the HPA cluster. Mixed HPA precursors $PMo_{(12-x)}V_xO_{40}^{(3+x)-}$ generally used in the field of mild oxidation catalysis have been prepared for their use in hydrodemetallation catalysis [128] or diesel hydrotreatment [144]. The synthesis of cobalt salt of substituted $PCoMo_{11}O_{40}H^{6-}$ has been developed leading to HDS catalysts with improved catalytic performances compared to those of conventional catalysts prepared from AHM and cobalt nitrate [151]. For hydrocracking catalytic application, NiW ASA (Amorphous Silica Alumina) supported sulfide catalysts were also prepared from heteropolytungstate Ni salts as the substituted $Ni_3PW_{11}NiO_{40}H$ or the lacunary $Ni_4SiW_{11}O_{39}$ salt [145]. For the CoMo system as well as for the NiW one, the vicinity of both elements in the HPA salt at the molecular level

was able to generate a great amount of Co-MoS$_2$ or Ni-WS$_2$ active phase after sulfidation leading to improved catalytic performances [117,152].

Conclusion

Literature review has shown that promoted and unpromoted bimetallic (Ni)MoW sulfides catalysts are efficient catalysts that revealed most of the time better catalytic performances than that of their monometallic counterpart. Due to their low cost and facility for regeneration, the use of supported (Ni)MoW catalysts should preferable than that of the bulk ones. All previously reported MoW mixed supported catalysts were prepared by impregnating a support with classical precursors (together or sequentially) such as ammonium heptamoybdate and ammonium metatungstate [9,11,70,82] or ammonium thiomolybdate (NH$_4$)$_2$MoS$_4$ and ammonium thiotungstate (NH$_4$)$_2$WS$_4$ [68]. Mechanical mixture of supported NiMo-NiW catalysts has also been proposed [85]. The efficiency of the mixed MoW was generally proven in HDS except in the case of mechanical mixture.

Taking into account the advantages and potential of using trimetallic NiMoW systems for hydrotreating of petroleum feedstock, a new approach to prepare (Ni)MoW catalysts is proposed in the present study. The (Ni)MoW/Al$_2$O$_3$ catalysts will be prepared using mixed MoW heteropolyacids H$_4$SiMo$_n$W$_{12-n}$O$_{40}$. The use of MoW HPAs will allow to start from a single molecular entity to introduce together Mo and W. As suggested by literature, this initial nanoscale proximity of Mo and W could induce and facilitate after sulfidation the formation of the mixed (MoW)S$_2$ phase whose formation was claimed by different authors to explain better catalytic performances of MoW catalysts. Catalytic performances will be investigated in HDS and hydrogenation reactions, the effect of nitrogen compound will be also studied. Besides classical characterizations, we propose also the innovative use of advanced characterization techniques such as XAS to investigate the environment of Mo and W during the catalyst in situ sulfidation together with HAADF-STEM to study the sulfided samples at the atomic scale in order to deeply investigate the possible formation of mixed (Ni)(MoW)S$_2$ phase.

References

1 P. Grange, X. Vanhaeren, Hydrotreating catalysts, an old story with new challenges // *Catal. Today* – 1997. –V. 36. –P. 375.

   R.G. Leliveld, S.E. Eijsbouts. How a 70-year-old catalytic refinery process is still ever dependent on innovation // *Catalysis Today* –2008. –V.130. –P.183–189.

2 C. Song, X. Ma. New design approaches to ultra-clean diesel fuels by deep desulfurization and deep dearomatization // *Appl. Catal. B* –2003. –V.41. –P. 207.

3 A. Stanislaus, A. Marafi, M. S. Rana. Recent advances in the science and technology of ultra low sulfur diesel (ULSD) production // *Catalysis Today* –2010. –V.153. –P.1–68.

4 E.B. Fox, Zhong-Wen Liu, Zhao-Tie Liu. Ultraclean Fuels Production and Utilization for the Twenty-First Century: Advances towards Sustainable Transportation // *Energy Fuels* –2013.

5 P. Raybaud. Understanding and predicting improved sulfide catalysts: Insights from first principles modeling // *Applied Catalysis A: General* –2007. –V.322. –P.76–91.

6 H. Topsøe, B.S. Clausen, F.E. Massoth (Eds.), Springer Verlag, Berlin, // *Hydrotreating Catalysis-Science and Technology* –1996. –V.11. –P.1-269.

7 H. Topsøe. The role of Co–Mo–S type structures in hydrotreating catalysts // *Appl. Catal. A* –2007. –V.322. –P.3–8.

8 S. Eijsbouts, F. Plantenga, B. Leliveld, Y. Inoue, K. Fujita. STARS and NEBULA–new generations of hydroprocessing catalysts for the production of ultra low sulfur diesel, Prepr. Pap. //*Am. Chem. Soc., Div. Fuel Chem.* –2003. –V.48(2). –P.494–495.

9 C. Thomazeau, C. Geantet, M. Lacroix, M. Danot, V. Harle, P. Raybaud. Predictive approach for the design of improved HDT catalysts: γ-Alumina supported (Ni, Co) promoted $Mo_{1-x}W_xS_2$ active phases // *Appl. Catal., A* –2007. –V.322. –P.92–97.

10 A. Olivas, D.H. Galván, G. Alonso, S. Fuentes. Trimetallic NiMoW unsupported catalysts for HDS // *Appl. Catal., A* –2009. –V.352. –P. 10–16.

11 L. van Haandel, M. Bremmer, P.J. Kooyman, J.A. Rob van Veen, T. Weber, E. J. M. Hensen. Structure−activity correlations in hydrodesulfurization reactions over Ni-promoted $Mo_xW_{(1-x)}S_2/Al_2O_3$ catalysts // *ACS Catal.* –2015. –V.5. –P.7276-7287.

12 J. G. Speight // *The Desulfurization of Heavy Oils and Residua.* –1999.

13 J. G. Speight // *The Refinery of the Future.* –2011.

14 P. Michaud, J.L. Lemberton, G. Pérot. Hydrodesulfurization of dibenzothiophene and 4,6-dimethyldibenzothiophene: Effect of an acid component on the activity of a sulfided NiMo on alumina catalyst //*Applied Catalysis A: General* –1998. –V.169. –P.343-353.

15 X. Ma, K. Sakanishi, I. Mochida. Hydrodesulfurization reactivities of various sulfur compounds in diesel fuel // *Ind. Eng. Chem. Res.* –1994. –V.33. –P.218-222.

16 M. Houalla, Broderick, D. H., Sapre, A. V., Nag, N. K., de Beer, V. H. J., Gates, B. C., and Kwart, H.,

J. Hydrodesulfurization of methyl-substituted dibenzothiophenes catalyzed by sulfided Co-Mo/γ-Al₂O₃ // *Catalysis* –1980. –V.61. –P.523.

17   V. Meille, E. Schulz, M. Lemaire, and Michel Vrinat Hydrodesulfurization of Alkyldibenzothiophenes over a NiMo/Al₂O₃ Catalyst: Kinetics and Mechanism // *Journal of catalysis* –1997. –V.170. –P.29–36.

18   H. Topsøe, B. Hinnemann, J. K. Nørskov, J. V. Lauritsen, F. Besenbacher, P. L. Hansen, G. Hytoft, R. G. Egeberg, K. G. Knudsen The role of reaction pathways and support interactions in the development of high activity hydrotreating catalysts // *Catalysis Today* –2005. –V.107–108 –P.12–22.

19   X.-L. Ma, K. Sakaanishi, I. Mochida. Hydrodesulfurization Reactivities of Various Sulfur Compounds in Vacuum Gas Oil // *Ind. Eng. Chem. Res.* V. 35 (1996) P. 2487

20   C. Botchwey, Dalai A.K., Adjaye J. Two-Stage Hydrotreating of Athabasca Heavy Gas Oil with Interstage Hydrogen Sulfide Removal: Effect of Process Conditions and Kinetic Analyses // *Industrial and Engineering Chemistry Research* –2004. –V.43. –P.5854-5861.

21   T. Koltai, M. Macaud, A. Guevara, E. Schulz, M. Lemaire, R. Bacaud, M. Vrina Comparative inhibiting effect of polycondensed aromatics and nitrogen compounds on the hydrodesulfurization of alkyldibenzothiophenes // *Applied Catalysis A: General* –2002. –V.231. –P.253–261.

22   M.J. Girgis, B.C. Gates. Reactivities, reaction networks, and kinetics in high-pressure catalytic hydroprocessing // *Industrial & Engineering Chemistry Research* –1991. –V.30. –P.2021.

23   A. Stanislaus, B.H. Cooper. Aromatic Hydrogenation Catalysis: A Review // *Catal. Rev.-Sci. Eng.,* –1994. –V.36(1). –P. 75-123.

24   F. van Looij, P. van der Laan, W.H.J. Stork, D.J. DiCamillo, J. Swain. Key parameters in deep hydrodesulfurization of diesel fuel // *Applied Catalysis A: General* –1998. –V.170. –P.1-12.

25   C. Aubert, R. Durand, P. Geneste, C. Moreau, Factors affecting the hydrogenation of substituted benzenes and phenols over a sulfided NiO-MoO₃/γ-Al₂O₃ catalyst // *Journal of Catalysis* –1988. –V.112. –P.12.

26   P. Zeuthen, K. G. Knudsen, D.D. Whitehurst. Organic nitrogen compounds in gas oil blends, their hydrotreated products and the importance to hydrotreatment // *Catalysis Today* –2001. –V.65. –P.307–314.

27   M.S. Rana, Navarro, R.; Leglise, J. Organic nitrogen compounds in gas oil blends, their hydrotreated products and the importance to hydrotreatment // *Catalysis Today* –2004. –V.98. –P.67-74.

28   V. La Vopa, C.N. Satterfield. Poisoning of thiophene hydrodesulfurization by nitrogen compounds // *Journal of Catalysis* –1988. –V.110 –P.375.

29   C. Kwak, J.J. Lee, J.S. Bae, S.H. Moon. Poisoning effect of nitrogen compounds on the performance of CoMoS/Al₂O₃ catalyst in the hydrodesulfurization of dibenzothiophene, 4-methyldibenzothiophene, and 4,6-dimethyldibenzothiophene // *Appl. Catal. B: Environ.* –2001. –V.35 –P.59–68.

30   G. C. Laredo, A. Montesinos, J. A. De los Reyes. Inhibition effects observed between dibenzothiophene and carbazole during the hydrotreating process // *Applied Catalysis A: General* –2004. –V.265. –P.171–183.

31   X. Tao, Y. Zhou, Q. Wei, S. Ding, W. Zhou, T. Liu, X. Li. Inhibiting effects of nitrogen compounds on deep hydrodesulfurization of straight-run gas oil over a NiW/Al$_2$O$_3$ catalyst // *Fuel* –2017. –V.188. – P.401–407.

32   H. Topsøe, R. Candia, N.-Y. Topsøe, B. S. Clausen. On the state of Co-Mo-S model // *Bull. Soc. Chim. Belg.* –1984. –V.93. –P.783-805.

33   Teh C. Ho Hydrodenitrogenation Catalysis// *Catalysis Reviews – Science and Engineering*. –1988. – V.30(1). –P.117-160.

34   N.-Y. Topsøe and H. Topsøe. Characterization of the structures and active sites in sulfided Co-MoAl$_2$O$_3$ and Ni-MoAl$_2$O$_3$ catalysts by NO chemisorption// *Journal of catalysis* –1983. –V.84. –P.386-401.

35   S.D. Kelly, N. Yang, G.E. Mickelson, N. Greenlay, E. Karapetrova, W. Sinkler, Simon R. Bare. Structural characterization of Ni–W hydrocracking catalysts using in situ EXAFS and HRTEM // *Journal of Catalysis* –2009. –V.263 –P.16–33.

36   S. Kasztelan, H. Toulhoat, J. Grimblot, J. P. Bonnelle. A geometrical model of the active phase of hydrotreating catalysts. // *Appl. Catal.* –1984. –V.13. –P.127–159.

37   M. Brorson, A. Carlsson, H. Topsøe. The morphology of MoS$_2$, WS$_2$, Co–Mo–S, Ni–Mo–S and Ni–W–S nanoclusters in hydrodesulfurization catalysts revealed by HAADF-STEM // Catalysis Today – 2007. –V.123 P.31–36.

38   M. Breysse, M. Cattenot, T. Decamp, R. Frety, C. Gachet, M. Lacroix, C. Leclerq, L. de Mourques, J. L. Portefaix, M. Vrinat, M. Houari, J. Grimblot, S. Kasztelan, J. P. Bonnelle, S. Housni, J. Bachelier and J. C. Duchet. Influence of sulphidation conditions on the properties of NiW/Al$_2$O$_3$ hydrotreating catalysts // *Catalysis Today* –1988. –V.4. –P.39.

39   Menno W. J. Craje, Stefan P. A. Louwers, Vincent H. J. De Beer, Roel Prins, and Adri M. Van der Kraan. An EXAFS study on the so-called "cobalt-molybdenum-sulfur" phase in cobalt/carbon and cobalt-molybdenum/carbon, compared with a Moessbauer emission spectroscopy study // *Journal of Physical Chemistry*. –1992. –V.96. –P.5445.

40   M. Breysse, J. Bachelier, J.P. Bonnelle, M. Cattenot, D. Cornet, T. Decamp, J.C. Duchet, P. Engelhard, R. Frety, C. Gachet, P. Geneste, J. Grimblot, C. Gueguen, S. Kasztelan, M. Lacroix, J.C. Lavalley, C. Leclercq, C. Moreau, L. De Mourgues, J.L. Olive, E. Payen, J.L. Portefaix, H. Toulhoat, M. Vrinat. New Developments in Hydrotreating Catalysis : Characterization and Optimization of Niw/A12O3 Catalysts // *Bull. Soc. Chim. Belg.* –1987. –V.96 –P.829.

41   R. Prins. Catalytic hydrodenitrogenation // *Advances In Catalysis*. –2001. –V.46 –P. 339.

42   M.J. Vissenberg, Y. van der Meer, E. J. M. Hensen, V. H. J. de Beer, A. M. van der Kraan, R. A. van Santen, J. A. R. van Veen. The Effect of Support Interaction on the Sulfidability of Al$_2$O$_3$- and TiO$_2$-Supported CoW and NiW Hydrodesulfurization Catalysts // *Journal of Catalysis* –2001. –V.198. – P.151–163.

43   E.J.M. Hensen, Y. van der Meer, J.A.R. van Veen, J.W. Niemantsverdriet. Insight into the formation of the active phases in supported NiW hydrotreating catalysts // *Applied Catalysis A: General* –2007. –

V.322 –P.16–32.

44 H. Toulhoat, P. Raybaud. Kinetic interpretation of catalytic activity patterns based on theoretical chemical descriptors // *Journal of Catalysis* –2003. –V.216 –P.63.

45 T.A.Pecoraro, R.R.Chianelli. Hydrodesulfurization catalysis by transition metal sulfides // *Journal of Catalysis* –1981. –V.67. –P.430-445.

46 P. Raybaud, G. Kresse, J. Hafner, and H. Toulhoat. Ab initio density functional studies of transition-metal sulphides: II. Electronic structure // *J.Phys.-Condens. Mat.* –1997. –V.9. –P.11085.

47 S. Eijsbouts. On the flexibility of the active phase in hydrotreating catalysts // *Applied Catalysis A: General.* –1997. –V158. –P.53-92.

48 J.G. Speight The chemistry and technology of petroleum // *4. ed. Boca Raton, Fla.: Taylor & Francis.* – 2006. –P.36.

49 M. Guisnet, Gilson J.P. Zeolites for cleaner technologies // *Imperial College Press London.* –2002. – V.3.

50 T. Kabe, Y.Aoyama, D. Wang, A. Ishihara, W. Qian, M. Hosoya, Q. Zhang. Effects of H_2S on hydrodesulfurization of dibenzothiophene and 4,6-dimethyldibenzothiophene on alumina-supported NiMo and NiW catalysts// *Applied Catalysis A: General.* –2001. –V.209. –P.237–247.

51 W.R.A. Mrobinson, J.A.R van Veen, V.H.J de Beer, R.A van Santen. Development of deep hydrodesulfurization catalysts: II. NiW, Pt and Pd catalysts tested with (substituted) dibenzothiophene // *Fuel Process. Technol.* –1999. –V.61. –№1. –P.103–116.

52 H.R. Reinhoudta, R.Troosta, A.D.van Langevelda, S.T. Siea, J.A.R. van Veenb, J.A. Moulijna. Catalysts for second-stage deep hydrodesulfurisation of gas oils // *Fuel Process. Technol.* –1999. –V.61. –№1. –P.133–147.

53 F.L. Plantenga, R. Cerfontain, S. Eijsbouts, F. van Houtert, G.H. Anderson, S. Miseo, S. Soled, K. Riley, K. Fujita, Y. Inoue. A novel catalyst for heavy oil hydrocracking //*Science and Technology in Catalysis.* –2002. –P.407-410.

54 Y. Gochi, C. Ornelas, F. Paraguay, S. Fuentes, L. Alvarez, J.L. Rico, G. Alonso- Núñez. Effect of sulfidation on Mo–W–Ni trimetallic catalysts in the HDS of DBT // *Catal. Today.* –2005. –V107–108. – P.531–536.

55 S.L. Soled, S. Miseo, R. Krikak, H. Vroman, T.H. Ho, K.L. Riley // US Patent 6,299,760 B1 (2001).

56 C. Yin, H. Liu, L. Zhao, B. Liu, S. Xue, N. Shen, Y. Liu,Y. Li, C. Liu. Study for the production of ultra-low sulfur gas oils on a highly loaded NiMoW catalyst // *Catalysis Today.* –2016. –V.259. –P.409–416.

57 C. Yin, Y. Wang, S. Xue, H. Liu, He Li, C. Liu. Influence of sulfidation conditions on morphology and hydrotreating performance of unsupported Ni–Mo–W catalysts // *Fuel.* –2016. –V.175 –P.13–19.

58 L. Wang, Y. Zhang, Y. Zhang, Z. Jiang, C. Li. Ultra-Deep Hydrodesulfurization of Diesel Fuels on Trimetallic NiMoW Sulfide Catalysts// *Chem. Eur. J.* –2009. –V.15. –P.12571–12575.

59 G. Alonso, G. Berhault, A. Aguilar, V. Collins, C. Ornelas, S. Fuentes, R. R. Chianelli. Characterization and HDS Activity of Mesoporous MoS2 Catalysts Prepared by in Situ Activation of

Tetraalkylammonium Thiomolybdates // *Journal of Catalysis*. –2002. –V.208 –P.359–369.

60   J. Bocarando, R. Huirache-Acuña, W. Bensch, Z.-D. Huang, V. Petranovskii, S. Fuentes, G. Alonso-Núñez. Unsupported Ni-Mo-W sulphide HDS catalysts with the varying nickel concentration // *Applied Catalysis A: General.* –2009. –V.363 –P.45–51.

61   J. Bocarando, G. Alonso- Núñez, W. Bensch, R. Huirache- Acuña, M. Del Valle, J. Cruz-Reyes. Comparative Study of In situ/Ex situ Activated Trimetallic NiMoW Sulfide Catalysts Prepared from Ammonium Thiomolybdotungstates // *Catal. Lett.* –2009. –V.130 –P.301–307.

62   Y.Yi, B. Zhang, X. Jin, L. Wang, C.T. Williams, G. Xiong, D. Su, C. Liang. Unsupported NiMoW sulfide catalysts for hydrodesulfurization of dibenzothiophene by thermal decomposition of thiosalts // *Journal of Molecular Catalysis A: Chemical* –2011. –V.351 –P.120–127.

63   R. Huirache-Acuña, M.A. Albiter, J. Espino, C. Ornelas, G. Alonso-Nunez,F. Paraguay-Delgado, J.L. Rico, R. Martınez-Sanchez. Synthesis of Ni–Mo–W sulphide catalysts by ex situ decomposition of trimetallic precursors // *Applied Catalysis A: General*. –2006. -V.304 –P.124–130.

64   R. Huirache-Acuña, M.A. Albiter, C. Ornelas, F. Paraguay-Delgado, R. Martınez-Sanchez, G. Alonso-Nunez. Ni(Co)-Mo-W sulphide unsupported HDS catalysts by ex situ decomposition of alkylthiomolybdotungstates // *Applied Catalysis A: General* –2006. –V.308 –P.134–142.

65   H. Nava, F. Pedraza, G. Alonso. Nickel-Molybdenum-Tungsten sulfide catalysts prepared by in situ activation of tri-metallic (Ni-Mo-W) alkylthiomolybdotungstates // *Catalysis Letters* –2005. –V.99 – P.65–71.

66   H. Nava, J. Espino, G. Berhault, G. Alonso-Nunez. Effect of phosphorus addition on unsupported Ni–Mo–W sulfide catalysts prepared by the in situ activation of nickel/tetramethylammonium thiomolybdotungstate // *Applied Catalysis A: General* –2006. –V.302. –P.177–184.

67   C. Thomazeau, C. Geantet, M. Lacroix, M. Danot, V. Harle. EXAFS Characterization of New Active Phases for Catalytic Hydrotreatment: Two Cations Disulfide Layers in the $Mo_xW_{(1-x)}S_2$ Lamellar Solid Solution // *Oil & Gas Science and Technology*. –2005. –V.60 –P.781-790.

68   C. Thomazeau, C. Geantet, M. Lacroix, V. Harle, S. Benazeth, C. Marhic, A M. Danot. Two Cation Disulfide Layers in the $W_xMo_{(1-x)}S_2$ Lamellar Solid Solution // *Journal of Solid State Chemistry*. –2001. –V.160. –P.147-155.

69   Y.E. Licea, R. Grau-Crespo, L.A. Palacio, A.C. Faro. Unsupported trimetallic Ni(Co)-Mo-W sulphide catalysts prepared from mixed oxides: Characterisation and catalytic tests for simultaneous tetralin HDA and dibenzothiophene HDS reactions // *Catalysis Today*. –2017. –V.292. –P.84-96.

70   J. Hein, O. Y. Gutierrez, E. Schachtl, P. Xu, N. D. Browning, A. Jentys, J. A. Lercher. Distribution of Metal Cations in Ni-Mo-W Sulfide Catalysts // *ChemCatChem*. –2015. –V.7. –P.3692 – 3704.

71   A. Gutiérrez-Alejandre, J. Ramírez, I. Jiménez-del Val, M. Peñuelas-Galaz, P. Sánchez-Neri, P.Torres-Mancera. Activity of NiW catalysts supported on TiO_2-Al_2O_3 mixed oxides: Effect of Ti incorporation method on the HDS of 4,6-DMDBT // *Catalysis Today*. –2005. –V.107–108. –P.879–884.

72   G. An, C. Liu, C. Xiong, C. Lu. A study on the morphology of unsupported Ni-Mo-W sulfide

hydrotreating catalysts through high-resolution transmission electron microscopy// *Petroleum Science and Technology*. –2012. –P.1599–1608.

73   S. Sigurdson, V. Sundaramurthy, A.K. Dalai, J. Adjaye Phosphorus promoted trimetallic NiMoW/γ-Al$_2$O$_3$ sulfide catalysts in gas oil hydrotreating // *Journal of Molecular Catalysis A: Chemical*. –2008. –V.291 –P.30–37.

74   L. Lan, S. Ge, K. Liu, Y. Hou, X. Bao. Synthesis of Ni$_2$P promoted trimetallic NiMoW/γ-Al$_2$O$_3$ catalysts for diesel oil hydrotreatment // *Journal of Natural Gas Chemistry*. –2011. –V.20 –P.117–122.

75   M. Cervantes-Gaxiola, M.-Albiter, A. Pérez-Larios, P. Balbuena, J. Espino-Valencia. Experimental and theoretical study of NiMoW, NiMo, and NiW sulfide catalysts supported on an AlTiMg mixed oxide during the hydrodesulfurization of dibenzothiophene // *Fuel*. –2013. –V.113 –P.733–743.

76   S. L. Soled; S. Miseo, R. Krycak, Hilda Vroman, T. C. Ho, K. L. Riley // US Patent 6,156,695 (2000).

77   S. Amaya, G. Alonso- Núñez, T.A. Zepeda, S. Fuentes, A. Echavarria. Effect of the divalent metal and the activation temperature of NiMoW and CoMoW on the dibenzothiophene hydrodesulfurization reaction // *Applied Catalysis B: Environmental*. –2014. –V.148–149 –P.221–230.

78   S. Amaya, G. Alonso-Núñez , J. Cruz-Reyes, S. Fuentes, A. Echavarría. Influence of the sulfidation temperature in a NiMoW catalyst derived from layered structure (NH$_4$)Ni$_2$OH(H$_2$O)(MoO$_4$)$_2$ // *Fuel*. –2015. –V.139 –P.575–583.

79   Z. Le, L. Xiangyun, L. Dadong, G. Xiaodong. Study on high-performance unsupported Ni–Mo–W hydrotreating catalyst // *Catalysis Communications*. –2011. –V.12 –P.927–931.

80   M. Absi-Halabi, A. Stanislaus and K. Al-Dolama Performance comparison of alumina-supported Ni-Mo, Ni-W and Ni-Mo-W catalysis in hydrotreating vacuum residue // *Fuel*. –1998. –V.77 –P.787–790.

81   H. Liu, C. Liu, C. Yin, B. Liu, X. Li, Y. Li, Y. Chai, Y. Liu. Low temperature catalytic hydrogenation naphthalene to decalin over highly-loaded NiMo, NiW and NiMoW catalysts // *Catalysis Today*. –2016. –V.276 –P.46–54.

82   S.L. González-Cortés, S. Rugmini, T. Xiao, M.L.H. Green, S.M. Rodulfo-Baechler and F.E. Imbert. Deep hydrotreating of different feedstocks over a highly active Al$_2$O$_3$-supported NiMoW sulfide catalyst // *Applied Catalysis A: General*. –2014. –V.475 –P.270–281.

83   H. Yu, S. Li, G. Jin. Catalytic Hydrotreating of the Diesel Distillate from Fushun Shale Oil for the Production of Clean Fuel // *Energy Fuels* –2010. –V.24 –P.4419–4424.

84   Di Liu, L. Liu, G. Li, C. Liu. Synthesis, characterization and hydrodesulfurization activity of silica-dispersed NiMoW trimetallic catalysts // *Journal of Natural Gas Chemistry*. –2010. –V.19 –P.530–533.

85   J. A. Mendoza-Nieto, O. Vera-Vallejo, L. Escobar-Alarcón, D. Solís-Casados, T. Klimova. Development of new trimetallic NiMoW catalysts supported on SBA-15 for deep hydrodesulfurization // *Fuel*. –2013. –V.110 –P.268–277.

86   J. Mendoza-Nieto, F. Robles-Méndez, T. Klimova. Support effect on the catalytic performance of trimetallic NiMoW catalysts prepared with citric acid in HDS of dibenzothiophenes // *Catalysis Today*. –2015. –V.250 –P.47-59.

87   M.A. Guzmán, R. Huirache-Acuña, C.V. Loricera, J.R. Hernández, J.N. Díaz de León, J.A. de los Reyes, B. Pawelec. Removal of refractory S-containing compounds from liquid fuels over P-loaded NiMoW/SBA-16 sulfide catalysts // *Fuel*. –2013. –V.103 –P.321–333.

88   R. Huirache-Acuña, B. Pawelec, C.V. Loricera, E.M. Rivera-Muñoz, R. Nava, B. Torres, J.L.G. Fierro. Comparison of the morphology and HDS activity of ternary Ni(Co)-Mo-W catalysts supported on Al-HMS and Al-SBA-16 substrates // *Applied Catalysis B: Environmental*. –2012. –V.125 –P.473-485.

89   N.N. Tomina, P.C. Solmanov, N.M. Maksimov, A.A. Pimerzin. Hydrotreatment of petroluem on Ni_6-$PMo_nW_{(12-n)}(S)/Al_2O_3$ catalysts // *Catalysis in Industry*. –2015. –V.7 –P.307–313.

90   Y. Wang, C. Yin, X. Zhao, C. Liu. Synthesis of bifunctional highly-loaded NiMoW catalysts and their catalytic performance of 4,6-DMDBT HDS // *Catalysis Communications*. –2017. –V.88 –P.13–17.

91   S. Arias, Y. E. Licea, D. Soares, J.G. Eon, L.A. Palacio, A.C. Faro Jr. Mixed NiMo, NiW and NiMoW sulfides obtained from layered double hydroxides as catalysts in simultaneous HDA and HDS reactions // *Catalysis Today* –2017.–V.296 –P.187–196.

92   S. Shan, H. Liu, Y. Yue, G. Shi, X. Bao. Trimetallic WMoNi diesel ultra-deep hydrodesulfurization catalysts with enhanced synergism prepared from inorganic–organic hybrid nanocrystals // *Journal of Catalysis*. –2016. –V.344 –P.325–333.

93   B. S. Clausen, H. Topsøe, R. Candia, J. Villadsen, B. Lengeler, J. Als-Nielsen, F. Christensen. Extended x-ray absorption fine structure study of the cobalt-molybdenum hydrodesulfurization catalysts // *J. Phys. Chem.* –1981. –V.85 –P.3868.

94   B.S. Clausen, B. Lengeler, R. Candia, J. Als-Nielsen, H. Topsøe. Exafs Studies of Calcined and Sulfided CO-Mo HDS Catalysts // *Bulletin des Sociétés Chimiques Belges*. –1981. –V.90 –P.1249.

95   Kulkarni G.U., Rao C.N.R. Exafs investigations of Fe-, Ni-, Co- and Cu- MoS_2/γ-Al_2O_3 hydrodesulphurization catalyst systems // *Catal. Lett.* –1991. –V.9 –P.427.

96   G. Sankar, P.R. Sarode, A. Srinivasan, C.N.R. Rao, S. Vasudevan, J.M. Thomas. A study of $Co/Mo/Al_2O_3$ hydrodesulphurization catalysts and related model compounds by XPS and x-ray absorption spectroscopy (XANES and EXAFS) // *Proceedings of the Indian Academy of Sciences - Chemical Sciences* –1984. –V.93 –P.321.

97   H. Topsøe, B.S. Clausen, H. Heinemann, G.A. Somorjai // *Catalysis and Surface Science* – 1985 – V. 21, P. 95.

98   H. Topsøe, B.S. Clausen, N-Y. Topsøe, P. Zeuthen. Progress in the design of hydrotreating catalysts based on fundamental molecular insight // *Catalysts in Petroleum Refining* – 1989. P.77–102.

99   W. Niemann, B.S. Clausen, H. Topsøe. X-Ray absorption studies of the Ni environment in Ni-Mo-S // *Catal. Lett.* –1990. –V.4 –P.355.

100   S.M.A.M. Bouwens, J.A.R. van Veen, D.C. Koningsberger, V.H.J. de Beer, R. Prins. Extended X-ray absorption fine structure determination of the structure of cobalt in carbon-supported Co and Co-Mo sulfide hydrodesulfurization catalysts. // *Journal of Physical Chemistry*. –1991. –V.95 –P.123.

101   A.S. Bommannavar, P.A. Montano. In situ study of the hydrogenation of quinoline over a Ni-Mo

supported catalyst // *Applications of Surface Science*. –1984. –V.19 –P.250.

102 S. M. A. M. Bouwens, D. C. Koningsberger, V. H. J. De Beer, S. P. A. Louwers, R. Prins. Exafs study of the local structure of Ni in Ni-MoS2/C hydrodesulfurization catalysts // *Catalysis Letters*. –1990. –V.5 –P.273.

103 S.P.A. Louwers, R. Prins. Ni EXAFS studies of the Ni-Mo-S structure in carbon-supported and alumina-supported Ni-Mo catalysts // *Journal of Catalysis*. –1992. –V.133 –P.94.

104 M. Sun, T. Bürgi, R. Cattaneo, D. Langeveld, R. Prins. TPS, XPS, QEXAFS, and XANES Investigation of the Sulfidation of NiW/Al$_2$O$_3$–F // *Journal of Catalysis*. –2001. –V.201 –P.258–269 .

105 N. Koizumi, Y. Hamabe, S. Jung, Y. Suzuki, S. Yoshida and M. Yamada. In situ observation of Ni-Mo-S phase formed on NiMo/Al$_2$O$_3$ catalyst sulfided at high pressure by means of Ni and Mo K-edge EXAFS spectroscopy // *J. Synchrotron Rad*. –2010. –V.17 –P.414–424.

106 Riccardo Cattaneo, Thomas Weber, Takafumi Shido, and Roel Prins. A Quick EXAFS Study of the Sulfidation of NiMo/SiO$_2$ Hydrotreating Catalysts Prepared with Chelating // *Journal of Catalysis*. –2000. –V.191 –P.225–236.

107 T. Kubota et al. In situ XAFS study of the sulfidation of Co–Mo/B$_2$O$_3$/Al$_2$O$_3$ hydrodesulfurization catalysts prepared by using citric acid as a chelating agent // *Applied Catalysis A: General*. –2010. –V. 373 –P.214–221.

108 D. Nicosia, R. Prins. The effect of phosphate and glycol on the sulfidation mechanism of CoMo/Al$_2$O$_3$ hydrotreating catalysts: an in situ QEXAFS study // *Journal of Catalysis*. –2005.–V.231 –P. 259–268.

109 A. Rochet, B. Baubet, V. Moizan, C. Pichon, V.Briois. Co-K and Mo K edges Quick-XAS study of the sulphidation properties of Mo/Al$_2$O$_3$ and CoMo/Al$_2$O$_3$ catalysts // Comptes Rendus Chimie –2016. –V.19–P. 1337-1351.

110 F. Besenbacher, M.Brorson, B.S.Clausen, S.Helveg, B.Hinnemann, J.Kibsgaard, J.V.Lauritsen, P.G.Moses, J.K.Nørskov, H.Topsøe Recent STM, DFT and HAADF-STEM studies of sulfide-based hydrotreating catalysts: Insight into mechanistic, structural and particle size effects // *Catalysis Today*. –2008. –V.130 –P.86–96.

111 D. O. Dumcenco, H. Kobayashi, Z. Liu, Y.-S. Huang, K. Suenaga. Visualization and quantification of transition metal atomic mixing in Mo$_{1-x}$W$_x$S$_2$ single layers// *Nature Communications*. –2013.

112 T. Alphazan, A. Bonduelle-Skrzypczak, C. Legens, Z. Boudene, A.-L. Taleb, A.-S. Gay, O. Ersen, C. Copéret, P. Raybaud. Improved promoter effect in NiWS catalysts through a molecular approach and an optimized Ni edge decoration // *Journal of Catalysis*. –2016. –V.340 –P.60–65.

113 A. Spojakina, E. Kraleva, K. Jiratova, L. Petrov. TiO*2*-supported iron–molybdenum hydrodesulfurization catalysts // *Applied Catalysis A: General*. –2005. –V.288 –P.10.

114 E. Kraleva, A. Spojakina, K. Jiratova, L. Petrov. Support effect on the properties of iron–molybdenum hydrodesulfurization catalysts // *Catalysis Letters*. –2006. –V.112 –V.203.

115 R. Shafi, M.R.H. Siddiqui, G.J. Hutchings, E.G.I.V. Derouane, Kozhevnikov. Heteropoly acid precursor to a catalyst for dibenzothiophene hydrodesulfurization // *Applied Catalysis A: General*. –2000. –V.204

–P.251.

116   B. Pawelec, R. Mariscal, J.L.G. Fierro, A. Greenwood, P.T. Vasudevan. Carbon-supported tungsten and nickel catalysts for hydrodesulfurization and hydrogenation reactions // *Applied Catalysis A: General.* – 2001. –V.206 –P.295

117   P. Blanchard, C. Lamonier, A. Griboval, E. Payen. New insight in the preparation of alumina supported hydrotreatment oxidic precursors: a molecular approach // *Applied Catalysis A: General.* –2007. –V.322 –P.33.

118   P.A. Nikulshin, N.N. Tomina, A.A. Pimerzin, A.V. Kucherov, V.M. Kogan. Investigation into the effect of the intermediate carbon carrier on the catalytic activity of the HDS catalysts prepared using heteropolycompounds // *Catal.Today.* –2010. –V.149 –V.82.

119   P.A. Nikulshin, N.N. Tomina, A.A. Pimerzin, A.Yu. Stakheev, I.S. Mashkovsky,V.M. Kogan. Effect of the second metal of Anderson type heteropolycompounds on hydrogenation and hydrodesulphurization properties of $XMo_6(S)/Al_2O_3$ and $Ni_{3-x}Mo_6(S)/Al_2O_3$ catalysts // *Applied Catalysis A: General.* –2011. – V.393 –P.146.

120   P.A. Nikulshin, V.A. Salnikov, A.V. Mozhaev, P.P. Minaev, V.M. Kogan, A.A.Pimerzin. Relationship between active phase morphology and catalytic properties of the carbon–alumina-supported Co(Ni)Mo catalysts in HDS and HYD reactions // *Journal of Catalysis.* –2014. –V.309 –P.386.

121   C.I. Cabello, F.M. Cabrerizo, A. Alvarez, H.J. Thomas. Decamolybdodicobaltate (III) heteropolyanion: structural, spectroscopical, thermal and hydrotreating catalytic properties // *Journal of Molecular Catalysis A: Chemical.* –2002. –V.186 –P.89.

122   I.L. Botto, C.I. Cabello, H.J. Thomas. $(NH_4)_6[TeMo_6O_{24}]·7H_2O$ Anderson phase as precursor of the $TeMo_5O_{16}$ catalytic phase: thermal and spectroscopic studies // *Materials Chemistry and Physics.* –1997. –V.47 –P.37.

123   C.I. Cabello, I.L. Botto, H.J. Thomas. Anderson type heteropolyoxomolybdates in catalysis: $(NH_4)_3[CoMo_6O_{24}H_6]·7H_2O/\gamma$-Al2O3 as alternative of Co-Mo/γ-Al_2O_3 hydrotreating catalysts // *Applied Catalysis A: General.* –2000. –V.197 –P.79.

124   I. Pettiti, I.L. Botto, C.I. Cabello, S. Colonna, M. Faticanti, G. Minelli, P. Porta, H.J.Thomas. Anderson-type heteropolyoxomolybdates in catalysis: 2. EXAFS study on γ-Al_2O_3-supported Mo, Co and Ni sulfided phases as HDS catalysts // *Applied Catalysis A: General.* –2001. –V.220 –P.113.

125   J. Mazurelle, C. Lamonier, E. Payen, D. Guillaume Use of the cobalt salt of the heteropolyanion $[Co_2Mo_{10}O_{38}H_4]_6$– for the preparation of CoMo HDS catalysts supported on Al_2O_3, TiO_2 and ZrO_2 // *Catal. Today.* –2008. –V.130 –P.41.

126   C. Lamonier, C. Martin, J. Mazurelle, V. Harlé, D. Guillaume, E. Payen. Molybdocobaltate cobalt salts: New starting materials for hydrotreating catalysts // *Applied Catalysis B: Environmental.* –2007. –V.70 –P.548.

127   A. Griboval, P. Blanchard, E. Payen, M. Fournier, J.L. Dubois. Alumina supported HDS catalysts prepared by impregnation with new heteropolycompounds. Comparison with catalysts prepared by

conventional Co–Mo–P coimpregnation // *Catal. Today.* –1998. –V.45 –P.277.

128   D. Soogund, Ph. Lecour, A. Daudin, B. Guichard, Ch. Legens, C. Lamonier, E. Payen. New Mo–V based oxidic precursor for the hydrotreatment of residues // *Applied Catalysis B: Environmental.* –2010. –V.98 –P.39.

129   H. Toulhoat, P. Raybaud. Catalysis by Transition Metal Sulphides // Editions Technip, Paris, 2013.

130   J.A.R. Van Veen, P.A.J.M. Hendriks, R.R. Andrea, E.J.G.M. Romers, A.E. Wilson. All Optical Determination of Microscopic and Macroscopic Structure of Chiral, Polar Microcrystals from Achiral, Nonpolar Molecules // *J. Phys. Chem.* –1990. –V.94 –P.5275.

131   A.V. Mozhaev, P.A. Nikul'shin, Al.A. Pimerzin, V.V. Konovalov, A.A. Pimerzin. Activity of Co(Ni)MoS/Al_2O_3 catalysts, derived from cobalt(nickel) salts of $H_6[Co_2Mo_{10}O_{38}H_4]$, in hydrogenolysis of thiophene and hydrogen treatment of diesel fraction // *Petrol. Chem.* –2012. –V.52 (1). –P.41.

132   P.A. Nikulshin et al. Genesis of HDT catalysts prepared with the use of Co_2Mo_{10}HPA and cobalt citrate: Study of their gas and liquid phase sulfidation // *Applied Catalysis B: Environmental* –2014. –V.158–159. –P.161.

133   P.A. Nikul'shin, A.V. Mozhaev, A.A. Pimerzin, N.N. Tomina, V.V. Konovalov, V.M.Kogan. Cobalt salts of decamolybdodicobaltic acid as precursors of the highly reactive type II CoMoS phase in hydrorefining catalysts // *Kinet. Catal.* –2012. –V.52(6) –P.862.

134   M.T. Pope. *Heteropoly and Isopoly Oxometalates, Springer,Heidelberg.* –1983.

135   Ivan V. Kozhevnikov. Catalysis by Heteropoly Acids and Multicomponent Polyoxometalates in Liquid-Phase Reactions //*Chem. Rev.* –1998. –V.98 –P.171-198

136   I.V. Kozhevnikov. Sustainable heterogeneous acid catalysis by heteropoly acids // *Journal of Molecular Catalysis A: Chemical.* –2007. –V.262 –P.86–92.

137   J.F. Keggin. The structure and formula of 12-phosphotungstic acid // *Proc. Royal Soc. A.* –1934. –V.144. –P.75-100

138   N. Mizuno and M. Misono. Heteropolyanions in catalysis // *Journal of Molecular Catalysis.* –1994. –V.86. –P.1-3, 319-342

139   G.M. Brown, M.R. Noe-Spirlet, W.R. Busing, H.A. Levy. Dodecatungstophosphoric acid hexahydrate, $(H_5O^{2+})_3(PW_{12}O_{40}{}^{3-})$. The true structure of Keggin's pentahydrate' from single-crystal X-ray and neutron diffraction data // *Acta Crystallographica Section B.* –1977. –B33. –P.1038-1046

140   A. Téazéa, G. Hervéa, R. Finke, G. David, K. Lyon. α-, β-, and γ-Dodecatungstosilicic Acids: Isomers and Related Lacunary Compounds // *Inorganic Syntheses.* –1990. –V.27. –P.85-96.

141   P. Souchay. Ions minéraux condensés // Masson et Cie, 1969.

142   P. Courtin. Heteropolyanions molybdiques et tungstiques substitues par le vanadium (V) // *Rev.Chim.Mineral.* –1971. –V.8. –P.75.

143   L. Lizama, T. Klimova. L. Lizama, T. Klimova / Applied Catalysis B: Environmental 82 (2008) 139–150 // *Applied Catalysis B: Environmental.* –2008. –V.82 –P.139–150.

144   N.N. Tomina, P.A. Nikul'shin, A.A. Pimerzin. Influence of Anderson and Keggin heteropoly

compounds as precursors of oxide phases in hydrotreating catalysts on their performance // *Petroleum Chemistry*. –2008. –V.48 (2) –P.92.

145   K. Ben Tayeb, C. Lamonier, C. Lancelot, M.Fournier, E. Payen, A. Bonduelle, F. Bertoncini. Study of the active phase of NiW hydrocracking sulfided catalysts obtained from an innovative heteropolyanion based preparation // *Catalysis Today*. –2010. –V.150 –P.207–212.

146   A. Griboval, P. Blanchard, E. Payen, M. Fournier, J.L. Dubois, J.R. Bernard. Characterization and catalytic performances of hydrotreatment catalysts prepared with silicium heteropolymolybdates: comparison with phosphorus doped catalysts // *Applied Catalysis A: General*. –2001. –V.217 –P.173.

147   J. Ramírez, A. Gutieìrrez-Alejandre, F. Saìnchez-Minero, V. Macías-Alcaìntara, P. Castillo-Villaloìn, L. Oliviero, F. Maugeì. HDS of 4,6-DMDBT over NiMoP/(x)Ti-SBA-15 catalysts prepared with $H_3PMo_{12}O_{40}$ // *Energy Fuels* –2012. –V.26 –P.773.

148   P.P. Minaev, P.A. Nikulshin, M.S. Kulikovaa, A.A. Pimerzina, V.M. Kogan. $NiWS/Al_2O_3$ hydrotreating catalysts prepared with 12-tungstophosphoric heteropolyacid and nickel citrate: Effect of Ni/W ratio // *Applied Catalysis A: General*. –2015. –V.505 –P.456-466.

149   P.A. Nikulshin, P.P. Minaev, A.V. Mozhaev, K.I. Maslakov, M.S. Kulikova, A.A. Pimerzin. Investigation of co-effect of 12-tungstophosphoric heteropolyacid, nickel citrate and carbon-coated alumina in preparation of NiW catalysts for HDS, HYD and HDN reactions // *Applied Catalysis B: Environmental*. –2015. –V.176 –P.374.

150   P.A. Nikulshin, V.A. Salnikov, A.N. Varakin, V.M. Kogan. The use of CoMoS catalysts supported on carbon-coated alumina for hydrodeoxygenation of guaiacol and oleic acid // *Catal. Today*. –2016. – V.271. –P.45-55.

151   A. Griboval, P. Blanchard, E. Payen, M. Fournier, J.L. Dubois and J.R. Bernard. Direct preparation of Co-Mo-P impregnating solutions for the preparation of hydrodesulfurization catalysts // *Phosphorus research bulletin*. –1999. –V.10. –P.436-441.

152   K. BenTayeb, C. Lamonier, C. Lancelot, M. Fournier, A. Bonduelle-Skrzypczak and F. Bertoncini. Active phase genesis of NiW hydrocracking catalysts based on nickel salt heteropolytungstate: Comparison with reference catalyst // *Applied Catalysis B: Environmental*. –2012. –V.126. –P.56-63.

Chapter 2

Synthesis of $H_4SiMo_nW_{12-n}O_{40}$ heteropolyacids

Introduction

Bibliographic part has shown the potential of supported MoW sulfide catalysts for hydrotreatment reactions. Moreover, the use of heteropolyanions salts containing together CoMo or NiW as precursors for HDT catalysts has proven significantly enhanced catalytic activity by comparison with the use of classical precursors. This beneficial effect was attributed to the simultaneous introduction of both metals in the same cluster. We propose here an innovative preparation way to prepare mixed MoW sulfide catalysts starting from mixed MoW heteropolyacids $H_4SiMo_nW_{12-n}O_{40}$, allowing to introduce together Mo and W in a single molecular entity. It opens new opportunity to achieve high synergetic effect between Mo-W metals in sulfide catalysis.

This chapter describes the preparation of two MoW heteropolyacids α-$H_4[SiMo_1W_{11}O_{40}]$ and β-$H_4[SiMo_3W_9O_{40}]$ prepared via the addition of one or three Mo atoms to lacunary Keggin heteropolytungstates anions $SiW_{11}O_{39}^{8-}$ and $SiW_9O_{34}H^{9-}$. Obtained crystals will be extensively characterized at the solid state combining single crystal X-Ray Diffraction and X-Ray Absorption Spectroscopy (XAS) at the Mo K and W L_{III} edges. Purity of these mixed heteropolyacids together with their stability in aqueous solution will be checked by Raman spectroscopy and polorography. Characterizations by Raman and XAS will also be performed after deposition on alumina support in order to check the preservation of the mixed heteropolyacids. For comparison purposes, MoW catalysts with the same Mo and W loadings will also be prepared using impregnating solutions prepared from a mixture of $H_4[SW_{12}O_{40}]$ and $H_4[SiMo_{12}O_{40}]$ as well as monometallic catalysts.

This part of the study will be submitted for publication to Catalysis Science and technology Journal (Royal Society of Chemistry).

Conclusion

Two MoW heropolyacids (HPA) α-$H_4[SiMo_1W_{11}O_{40}]$ and β-$H_4[SiMo_3W_9O_{40}]$ have been successfully synthesized from their corresponding mixed potassium salts starting from mono and tri-vacant heteropolytungstates. Composition and structure of the obtained crystals have been confirmed by IR-, Raman, Single crystal X-Ray diffraction and XAS methods.

Some features of the HPAs structure were shown. Using X-Ray diffraction it was proved for the first time that in the β structure where one W_3O_{13} is rotated by 60°, ordered W substitution by Mo in each of the three other W_3O_{13} groups takes place. These results have been confirmed by EXAFS at the Mo K edge showing typical Mo-second neighbours distances with successful fits for both mixed heteropolyacids.

The purity of the samples and their stability in aqueous solution checked by characterization at the liquid state using Raman spectroscopy and polarography have allowed the preparation of impregnating solution. Alumina supported catalysts were prepared with a loading corresponding to a total density set at 4(Mo+W) /nm^2

After impregnation and drying, Raman and EXAFS experiments at the WL_{III} and MoK edges of oxide catalyst have been performed. After deposition on alumina, both heteropolyanions are preserved as clearly demonstrated by EXAFS and can ensure the nanoscale proximity between W and Mo after deposition on alumina. It has been shown that for $SiMo_{12}/Al_2O_3$, the corresponding $H_4SiMo_{12}O_{40}$ HPA was not preserved on alumina surface after drying.

First catalytic results have been obtained in dibenzothiophene HDS and naphthalene HYD showing clearly that catalysts prepared from mixed HPA are much more active than their MoW counterparts prepared from a mixture a HPA. These improved catalytic performances together with similar Mo and W sulfidation rate evaluated by XPS support the formation of more efficient active phase when using mixed HPA. For the most efficient MoW catalyst, EXAFS refinements after sulfidation revealed besides the W-W contribution at 3.17 Å another W-Mo contribution at 3.15 Å evidencing the presence of a mixed sulphide $MoWS_2$ phase.

The chapter 3 will be devoted to further characterization of these mixed phase and its genesis. Catalytic properties of prepared catalysts activated by liquid phase sulfidation will also be evaluated in HDT of model feed.

Chapter 3

Unpromoted alumina supported MoWS$_2$ hydrotreating catalysts

In the previous chapter, we have prepared and characterized mixed MoW heteropolyacids further used as precursors for the synthesis of Mo-W alumina supported hydrotreating catalysts. In the HDS of DBT and HYD of naphthalene, after activation under H_2S, these catalysts were found more efficient than their counterparts obtained by a mixture of monometallic HPAs with the same Mo/W ratio, which was related to the formation of a mixed Mo-W sulfided phase when using mixed HPA as precursor. Indeed in this case XAS study at the final state of sulfidation step evidenced a Mo-W contribution at the Mo and W edges, indicating that the MoW nanoscale proximity in the structure of mixed HPAs could favor the formation of the mixed phase.

For a better understanding of the behavior of our solids, we thus propose in the first part of this chapter to deepen the characterization of the mixed sulfided phase. Genesis of the active phase was followed by in-situ monitoring of the sulfidation of the catalysts by Quick-XAS, in order to evidence the formation of sulfidation intermediates and their temperature of appearance depending on the solids. High Angle Annular Dark Field (HAADF) was used to visualize the repartition of Mo and W in the sulfided slabs, as this technique is sensitive to difference in atomic number of the atoms.

In the second part of this chapter, activation by dimethyl disulfide (DMDS) during liquid phase sulfidation was performed instead of gas phase sulfidation. Investigation of the physicochemical properties and of the catalytic performance of these Mo-W based solids in HDS of DBT and naphthalene HYD after this different activation was conducted. This part of study was published in [Applied Catalysis B: Environmental 224 (2018) 951–959].

The third part of this chapter is dedicated to the comparison between the properties of the solids depending on the activation, under gas or liquid phase.

3.1 Application of Advanced Characterization Techniques for characterization of (Mo)W/Al₂O₃ catalysts

3.1.1. Quick-XAS study of evolution of (Mo)W/Al₂O₃ catalysts during *in situ* gas phase sulfidation

The aim of the study was to explore the genesis of mixed sulfides during *in situ* H_2S/H_2 sulfidation of Mo_3W_9/Al_2O_3 catalyst as well as two monometallic references (prepared from $SiMo(W)_{12}$ HPA) and bimetallic $(Mo_3+W_9)/Al_2O_3$ ones prepared using the mixtures of monometallic HPA by Quick X-ray absorption spectroscopy at the ROCK beamline at SOLEIL. Powered dried oxide catalysts were loaded in the catalytic cell [1] and the *in situ* sulfidation was performed in a flow of 10 % H_2S in H_2 at atmospheric pressure from room temperature (RT) to 400 °C followed by a plateau of 2 h with a heating rate of 3 °C/min and. Both Mo K edge and W L edges of the bimetallic catalyst were characterized during the same *in situ* treatment. The sequence of acquisition and scheme of the heating of the (Mo)W/Al₂O₃ catalysts used in this work is presented in Fig. 1. For the whole measurements, XAS spectra were obtained in transmission mode with ionization chambers as X-Ray detectors. The ionization chambers were filled with a mixture of argon and nitrogen (50:50) for measurements at the Mo K edge and (73:27) at the W L_{III} edge.
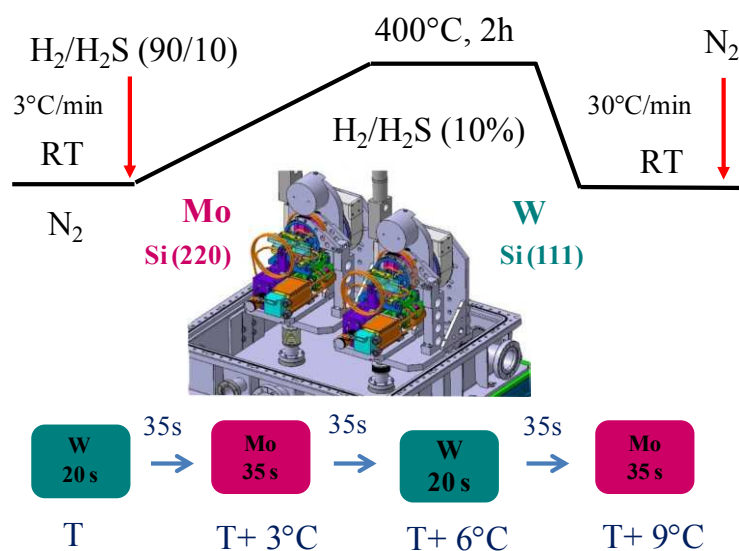

Fig. 1. XAS data acquisition sequence switching between Mo K edge and W L_{III} edge (with the time required for edge jump, changing the monochromator, reference metallic foil, amplifier gains and gases filling the ionization chambers) and scheme of the heating.

Mo K edge QEXAFS spectra collected during the sulfidation are presented in Fig. 2. In the Fourier transform of the spectrum at RT, the signal between 0.5 and 2 Å (not phase corrected) can be assigned to the octahedral coordination of the Mo absorber atom with oxygen atoms. [2,3]. The signal at 3 Å (not phase corrected) can be associated with a Mo–metal contribution [2,4]. Mo atoms are mainly in oxygen surrounding for Mo_{12}/Al_2O_3, Mo_3W_9/Al_2O_3 and $(Mo_3+W_9)/Al_2O_3$ catalysts at RT. Mo-S shoulder at 1.8 Å (not shift corrected) was not significant in all samples. However, the behaviors of the catalysts differed at 100 °C of sulfidation. $(Mo_3+W_9)/Al_2O_3$ catalyst showed higher Mo-S contribution than Mo-O contribution while the reverse is observed on Mo_3W_9/Al_2O_3. This can be related to higher stability against sulfidation of Mo in Mo_3W_9 HPA compared to that of Mo in separate $SiMo_{12}$ HPA. These differences are maintained at 200 °C, with almost all Mo in $(Mo_3+W_9)/Al_2O_3$ catalyst in sulfide form. At 400 °C, the majority of Mo atoms in Mo_3W_9/Al_2O_3 are present at the sulfidic state with a small Mo-M (M-metal) component. In opposite, for $(Mo_3+W_9)/Al_2O_3$ catalyst a peak at ~ 3 Å (not shift corrected) is clearly seen indicating the formation of larger MoS_2 clusters. At final sulfidation state after 2h of plateau at 400 °C this Mo-M contribution kept on evolving for both solids, ending with a higher Mo-Mo contribution in $(Mo_3+W_9)/Al_2O_3$ than that of Mo_{12}/Al_2O_3 in Mo_3W_9/Al_2O_3. Thus, mechanisms of MoO_x sulfidation of the catalysts are different as well as final state of Mo clusters.
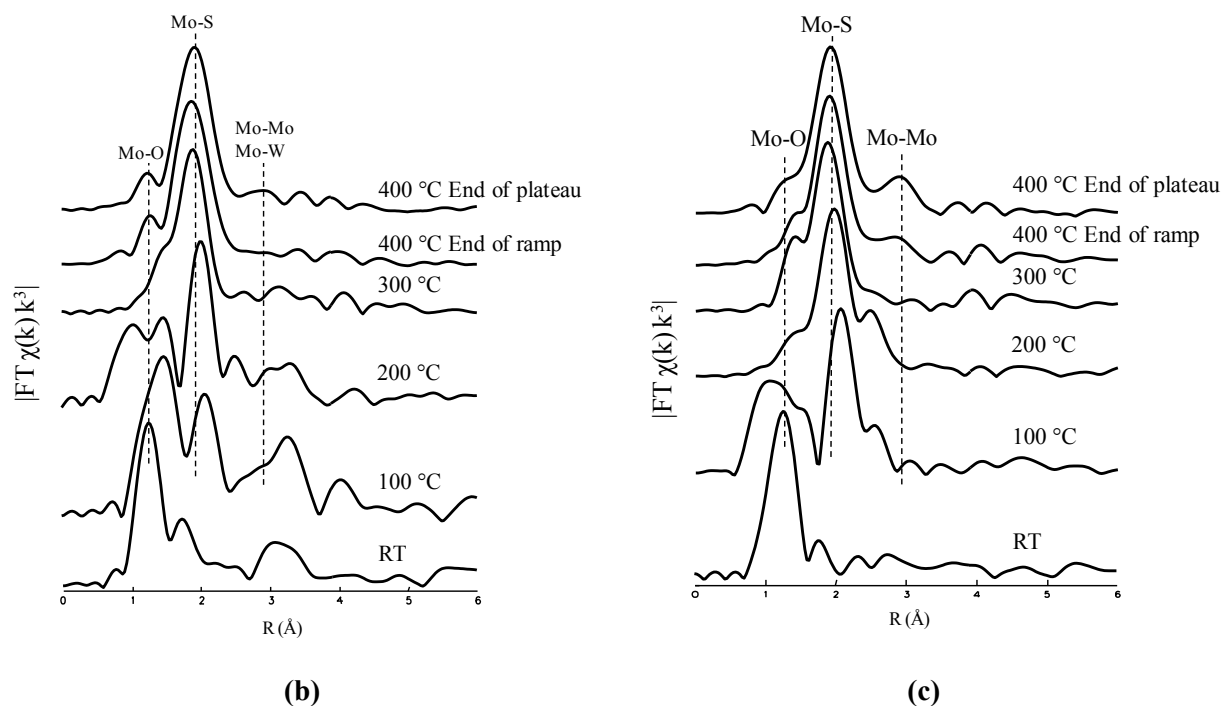

(a)

(b)   **(c)**
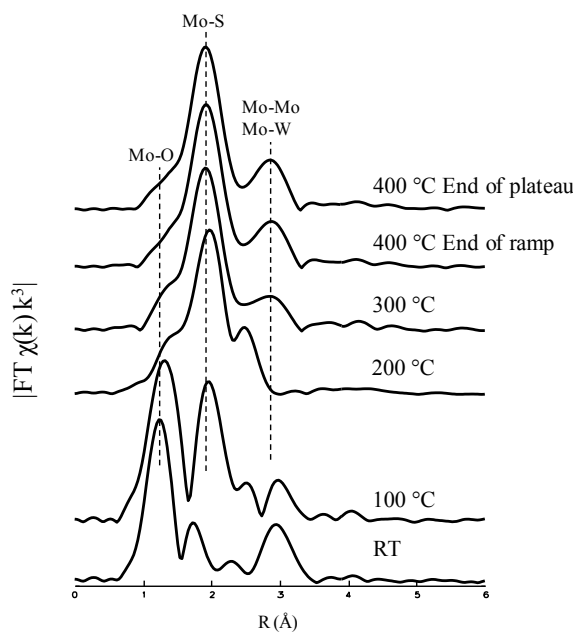
Fig. 2. Fourier transforms of the Mo *K*-edge k^3-weighted Quick EXAFS functions measured during the sulfidation of Mo_{12}/Al_2O_3 (a), Mo_3W_9/Al_2O_3 (b) and $(Mo_3+W_9)/Al_2O_3$ (c), *k* range 3.2–12 Å^{-1}.

Fig. 3 shows the $\chi(k)k^3$ FT of the W L_{III} edge EXAFS spectra collected during the in situ sulfidation of the catalysts. The first peak in all spectra recorded at RT between 1 and 1.7 Å (not shift corrected) is attributed to the W-O bonds [5-7], second peak ~ 3.4 Å (not shift corrected) is associated with W-M bonds [7].

It can be seen from Fig. 3 that, despite the sulfidation treatment, the oxidic phase is presented up to about 400 °C (end of the heating ramp) for both bimetallic samples, while in monometallic catalyst W-O signal disappears only to end of plateau. The most significant changes in the first coordination shell start after 200 °C in W_{12}/Al_2O_3 and $(Mo_3+W_9)/Al_2O_3$. Transformation of the oxidic phase of mixed HPA based catalysts Mo_3W_9/Al_2O_3 begins after 100 °C. The peak located between 1.9 and 2.3 Å (not phase-corrected) which is attributed to the W-S coordination in WS_2, has already appeared up to 300 °C in Mo_3W_9/Al_2O_3 catalyst and only at 400 °C in monometallic and bimetallic references. However, intense of W-S signal increases during plateau for all samples. The appearance of the second metal-metal shell at 2.8-3.3 Å (not phase-corrected) at 400 °C is an indication of the formation of well-developed WS_2 particles is more pronounced for W_{12}/Al_2O_3 and less for Mo_3W_9/Al_2O_3 due to presence of Mo neighbors in this shell.

(a)

(b)

(c)
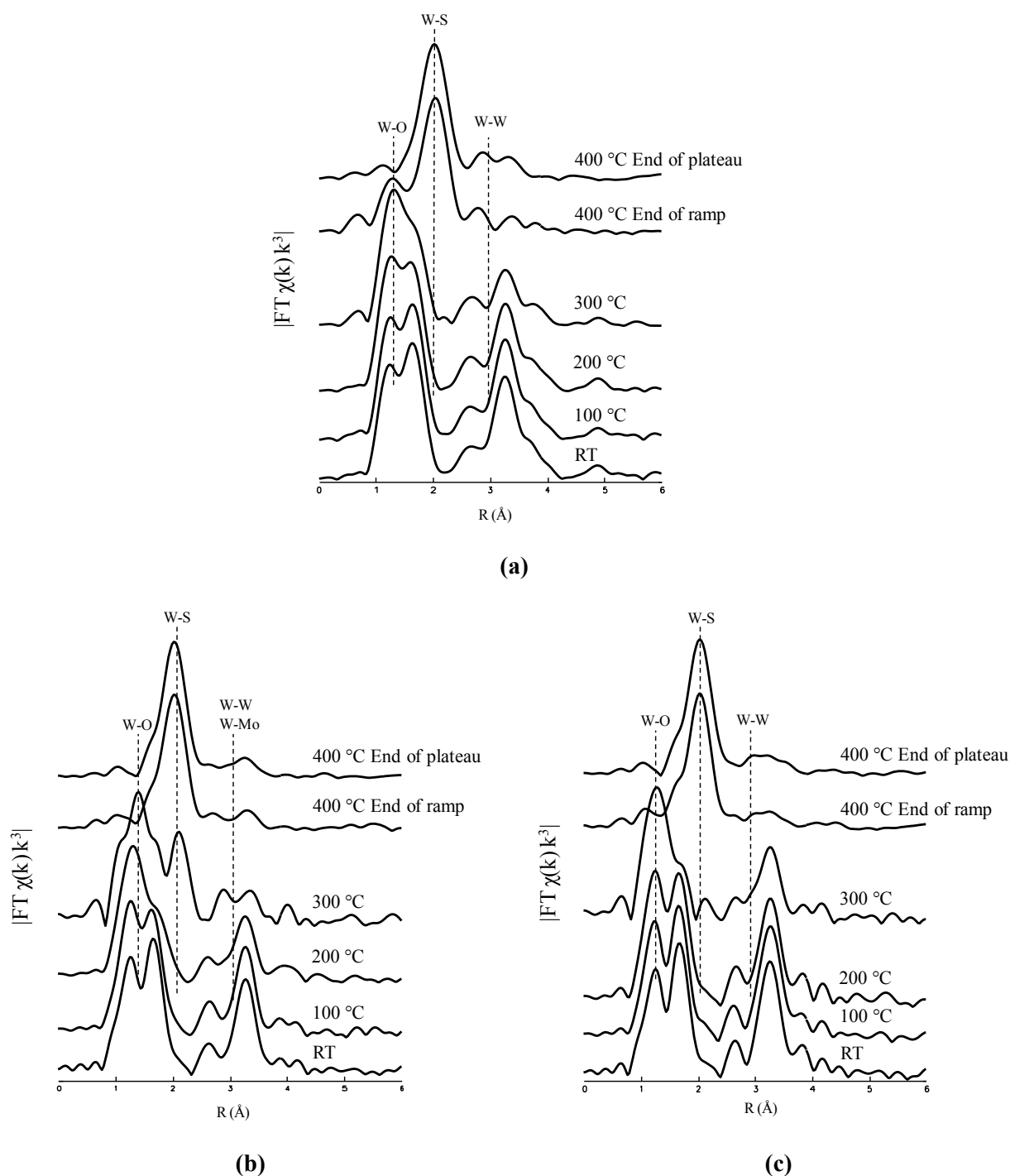
Fig. 3. Fourier transforms of the W *K*-edge k^3-weighted Quick EXAFS functions measured during the sulfidation of W_{12}/Al_2O_3 (a), Mo_3W_9/Al_2O_3 (b) and $(Mo_3+W_9)/Al_2O_3$ (c), *k* range 4–12 $Å^{-1}$.

During the sulfidation process, complex chemical transformations involving several intermediate species occur. The determination of the number of those intermediate species cannot be easily done by visualizing the XAS spectra alone. However, the use of more sophisticated multivariate methods based on linear algebra could help to estimate the number of components in a mixture of unknowns involved in a reaction [3,8]. MCR-ALS (multivariate

curved regression with alternative least squares) is a group of methods, which intend the recovery of the pure spectra and provide a quantitative concentration profile for each component. The key ideas of those methods are to represent the original data matrix "D" containing the "q" spectra recorded along the reaction with a "k" number of energy points by the sum of a product of two matrices "C" and "ST" characterized for each matrix in one direction by a smaller "n" dimensionality than "q" and of a residual matrix "E" containing the experimental noise, as schematized in Fig. 4 [3].
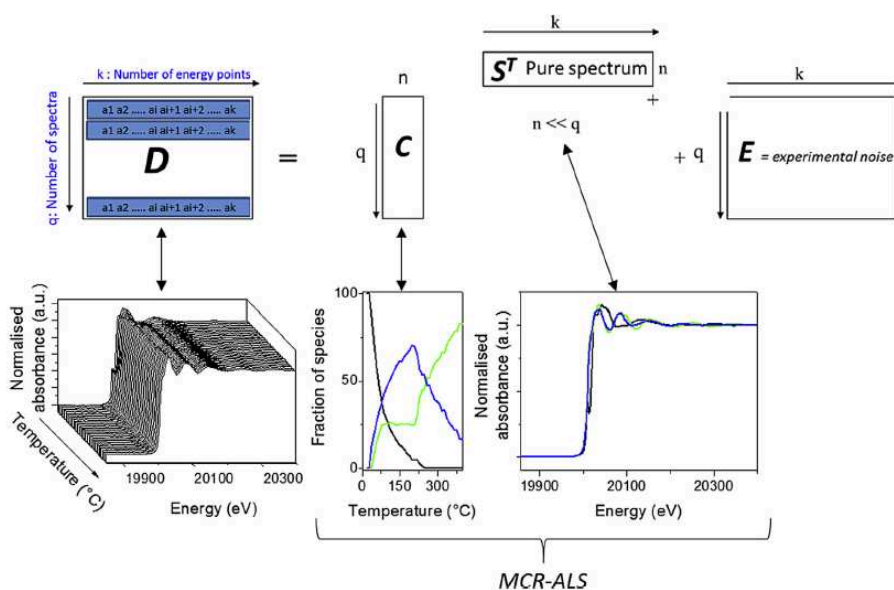
Fig. 4. Fig. 3. Schematic representation of the multivariate curve resolution analysis of the time-resolved experimental XAS data D. In the MCR-ALS method C and S^T are the concentration matrix of the pure species and the pure XAS spectra matrix, respectively. In the PCA analysis, C is the column matrix corresponding to the weight of each principal component described in the row matrix S^T [3].

The basic assumption for applying MCR-ALS method is the inner linear structure of the data set, which is fully verified for spectroscopic techniques following the Beer-Lambert law. In that case, the experimental data are first represented in a matrix form. Taking into account the linear structure of the data set, a bilinear decomposition of the matrix D can be done into the matrix containing pure concentration profiles C and the matrix containing pure spectra S^T of the k species of the unknown mixtures according to relation: $D = CS^T + E,$ where the matrix E contains the residual variation of the data (typically the experimental noise). The superscript T means the transpose of matrix S, where pure spectra are columns. Matrices C and S^T are responsible for the observed data variance. MCR techniques do not require a priori information concerning the data for resolving C and S^T, except an estimation of the number of pure

components. The description of the MCR-ALS methodology applied to XAS has been detailed [9-11].

Prior using the MCR-ALS method the number of components were determined by PCA (principal component analysis). PCA is a dimension-reduction tool that can be used to reduce a large set of variables to a small set that still contains most of the information in the large set.

According to the matrix rank previously determined by PCA, the MCR-ALS minimization of the Mo K edge of all $Mo(W)/Al_2O_3$ catalyst was done with four components (Fig. 5).

Mo_{12}/Al_2O_3

Mo_3W_9/Al_2O_3

$(Mo_3+W_9)/Al_2O_3$

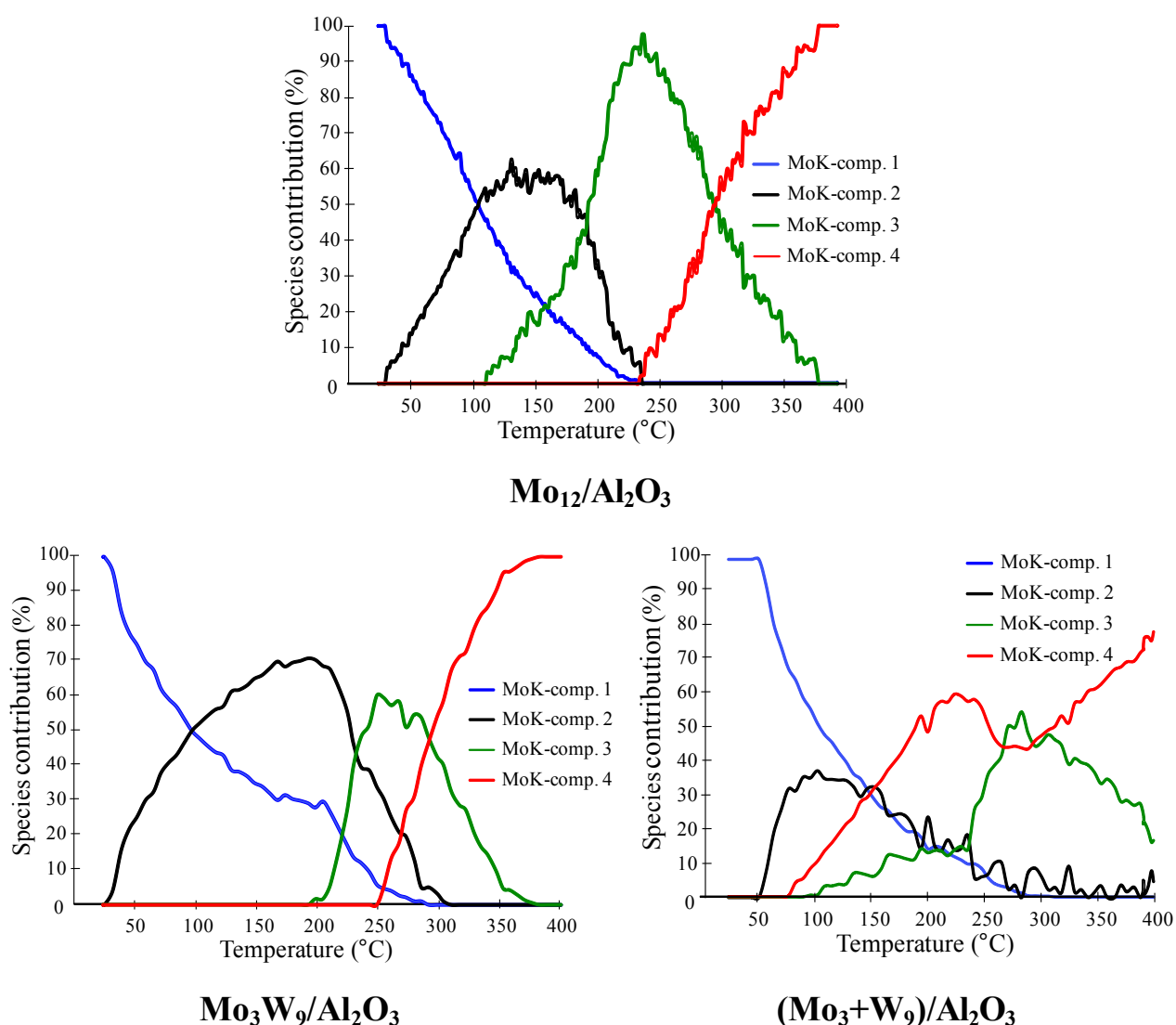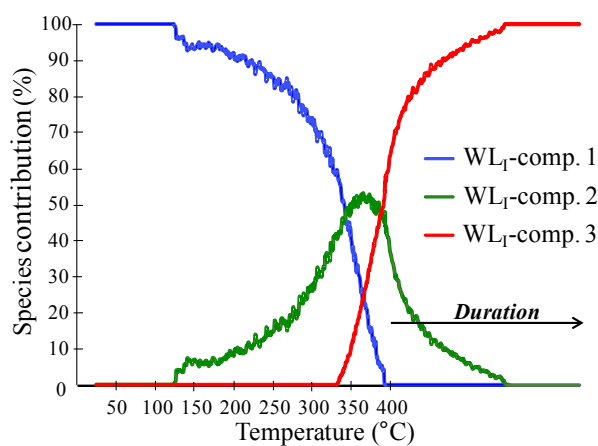**Fig. 5.** Concentration profile of components determined by MCR-ALS for Mo K edge as a function of the temperature during sulfidation.

The data analysis of Mo K edge was done on matrix with spectra collected during the heating ramp. It can be explained by the fact that the most part of Mo atoms transformed to the sulfide state before 400 °C and only the length of the slabs changes during the plateau. The

spectra of the first (MoK-comp.1) and last components (MoK-comp.4) determined by MCR-ALS for each catalyst are superimposable to the respective oxidic catalysts before sulfidation and last spectra of the ramp (as presented in supporting information, Fig. S1). It can be seen from the concentration profile that the nature of starting precursor influences on the sulfidation mechanism (Fig. 5).

Mo species in monometallic catalysts start to sulfide at low temperature around 30 °C (appearance of MoK-comp.2) that is in agreement with the results reported in [3]. MoK-comp.3 appeared at ~ 110 °C. Formation of MoS_2 species (MoK-comp.4) begins to be observed from ~235 °C. Molybdenum is completely sulfided at ~380 °C. Mixed HPA based catalyst begins sulfidation at the same temperature as Mo_{12}/Al_2O_3. However, third and fourth components appeared at higher temperature around 200 °C and 250 °C, respectively. It should be noticed that the final sulfide phase in Mo_3W_9/Al_2O_3 sample is present in parallel with first three components (in the range of 250 – 300 °C), while MoS_2 in monometallic sample appeared when first oxide and second components completely disappeared. Unfortunately, inadequate quality of spectra collected at Mo K edge during $(Mo_3+W_9)/Al_2O_3$ sulfidation prevents their interpretation.

The data analysis of W L_{III} edge was done on matrix with spectra collected during the heating ramp and 2h of plateau, due to the slower sulfidation kinetics of W its complete transformation proceeds during the plateau. The Fig. 6 presents the concentration profiles of components determined by MCR-ALS for WL_{III} edge of W_{12}/Al_2O_3, Mo_3W_9/Al_2O_3, $(Mo_3+W_9)/Al_2O_3$ as a function of the sulfidation temperature. Three components were found for all studied catalysts. The XANES spectrum of the first components isolated by MCR-ALS for all catalysts (Fig. S2) display the shape of the spectrum of initial oxidic catalysts. The spectra of the third are superimposable to that of the fully sulfided catalysts (Fig. S2).

W_{12}/Al_2O_3

Mo_3W_9/Al_2O_3 $(Mo_3+W_9)/Al_2O_3$
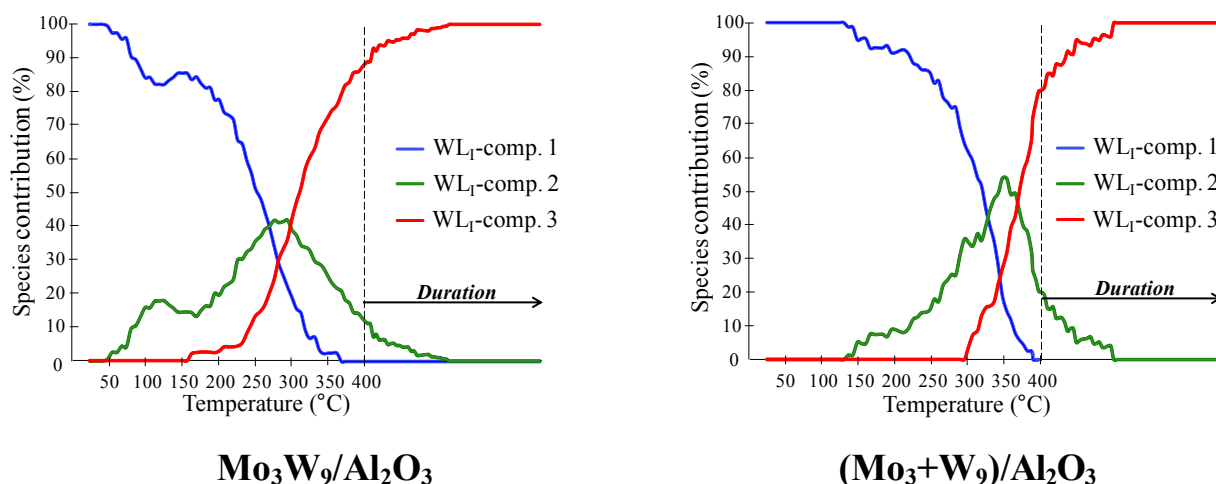
Fig. 6. Concentration profile of components determined by MCR-ALS for WL_{III} edge as a function of the temperature during sulfidation.

For monometallic W_{12}/Al_2O_3 catalyst the formation of tungsten sulfide begins at 330 °C (Fig. 6). Incorporation of Mo into the structure of SiW_{12} HPA led to decrease the startup W sulfidation temperature from 330 °C to 160 °C, while the use of mixture monometallic HPAs allowed only slightly reducing this startup temperature (~300 °C) compared to the monometallic one. For all catalysts tungsten is totally sulfided after the 2h sulfidation plateau. However at 400 °C, the tungsten sulfide contribution reaches 90% and 80% for Mo_3W_9/Al_2O_3 and $(Mo_3+W_9)/Al_2O_3$, respectively, and 65% for monometallic W_{12}/Al_2O_3 catalyst. It is interesting to note that final WS_2 contribution in Mo_3W_9/Al_2O_3 sample appears at 160 ºC but intensively increases only at 230-240 ºC simultaneously with the growth of the MoS_2 in Mo_3W_9/Al_2O_3 (Fig. 5). At 300 ºC, around 60 % of Mo is in molybdenum sulfide whereas percentage of WS_2 is equal to 45-50 %. These results indicate simultaneous sulfidation mechanism of both Mo and W metal in Mo_3W_9/Al_2O_3 catalyst, which may be related to the formation of the mixed Mo-W sulfide slabs.

3.1.2. HAADF characterization of gas phase suldided (Mo)W/Al$_2$O$_3$ catalysts

Bright field TEM observations routinely provide morphological information on the supported Mo(W)S$_2$ slabs and allow to access through statistical analysis to distribution in length and stacking of the sulfided nanoparticles. However only slabs roughly parallel to the electron beam can be observed, as contrast between the thin monolayers and the alumina support is not strong enough to enable the visualization of the basal plane of the slabs. Contrariwise, in the HAADF-STEM detection mode, images are formed by collecting electrons scattered at high angles by an annular dark-field detector and intensities in the images thus depend on the atomic number of the elements. This technique, favorable to the detection of heavy elements supported on light support, was first used to investigate MoS$_2$ and WS$_2$ nanoclusters supported on graphitic carbon, sulfided at high temperature (1073 K) and with a low metal density to ensure optimum visualization (Mo (W) loading around 0.3 wt% (0.6 wt%)) [12]. The authors demonstrated that the HAADF-STEM technique allowed to visualize the complete shape of the MoS$_2$ and WS$_2$ nanoclusters. Development of aberration corrected microscopes made it further possible to obtain atomic resolution on molybdenum disulfide supported on graphite [13]. To gain information on solids supported on carriers more representative of the industrial ones, morphology of WS$_2$ supported on amorphous silica−alumina (ASA) was successfully investigated in [14,15]. The analysis was again performed on samples sulfided at high temperature (600 °C) and for low W coverage (ca. 0.5 to 0.8 W nm^{-2}).

In a recent study [16], a new step has been taken with the study of MoS$_2$ supported on alumina, as MoS$_2$ has a smaller Z than WS$_2$ and thus a weaker contrast with alumina support compared to WS$_2$ on ASA. Again the samples were sulfided under more severe conditions than the ones used to obtain the active phase, at high temperature under H$_2$/H$_2$S or under pure H$_2$S (550 °C and 700 °C), with a lower coverage than in the industrial catalysts (2.3 at.nm^{-2}). The authors observed that increasing the sulfidation temperature from 550 to 700 °C led to the formation of more numerous, symmetrical and larger slabs.

Due to the sensitivity of the technique to atomic number of the elements, we thus proposed to use HAADF for characterization of our mixed Mo-W catalyst, the difference in Z auguring well for possible discrimination between the two atoms (Z(Mo) = 42, Z(W) = 74). Indeed since the annular dark field images are formed by collecting electrons scattered at high angles, the intensities of the atomic columns in the HAADF images increase with the atomic number Z of the atom as approximately Z$^{1.7}$ [17].

Prior to HAADF characterization the catalysts were sulfided by gas phase (GP) procedure under the same conditions as those used for activation of the solids prior to catalytic evaluation (Chapter 1) and during synchrotron measurement sessions.

Typical HAADF images of the sulfided catalysts are presented in Fig. 7. Compared to solids supported on model carriers or sulfided under severe conditions, more irregular shapes are observed, which can be related to the interaction of the active phase with the irregular surface of the alumina. Small clusters (<1 nm) and isolated atoms are also evidenced, which presence is not visible by TEM.
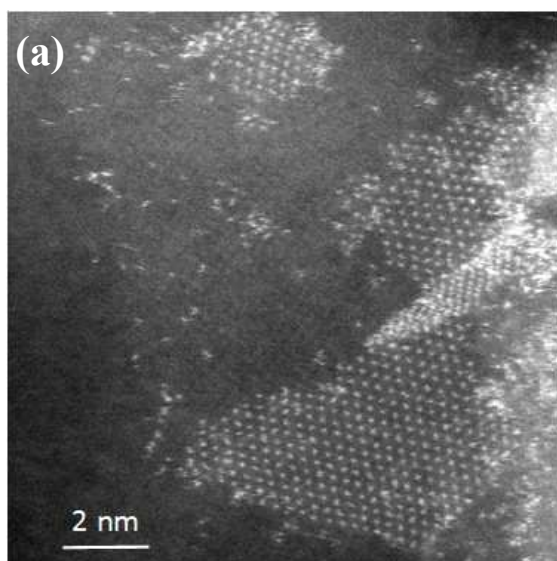
W_{12}/Al_2O_3 GP
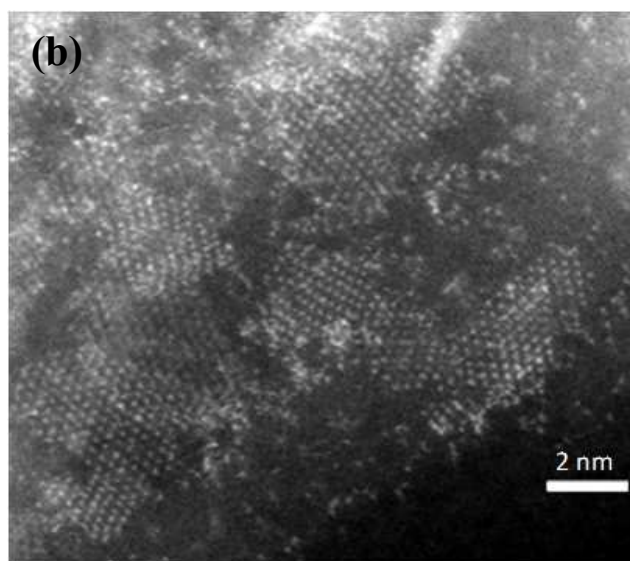
$(Mo_3+W_9)/Al_2O_3$ GP
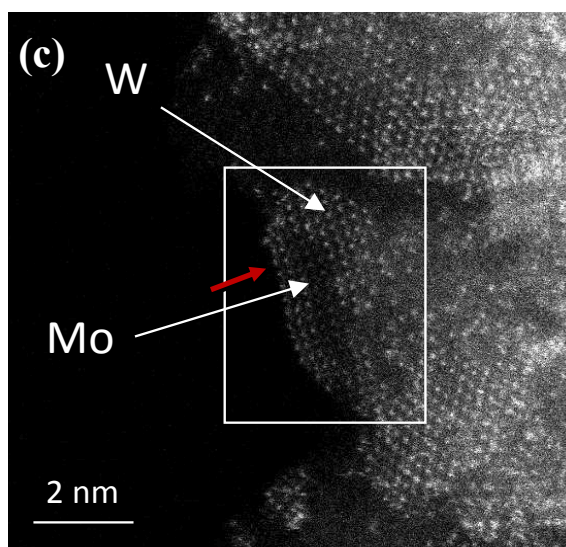
Mo_3W_9/Al_2O_3 GP
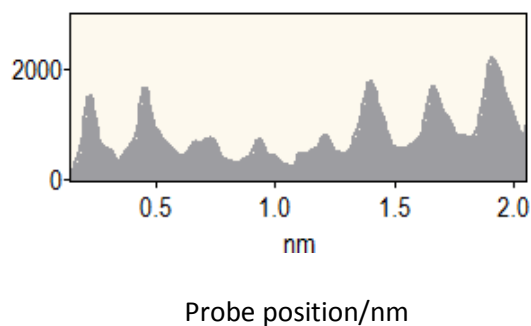
Fig. 7. HAADF images of GP sulfided W_{12}/Al_2O_3 (a), Mo_3+W_9/Al_2O_3 (b), Mo_3W_9/Al_2O_3 (c) catalysts with intensity profiles corresponding to the row of atoms identified by the arrow on Mo_3W_9/Al_2O_3.

All images of W_{12}/Al_2O_3 sample present a very homogeneous intensity of tungsten atoms in the slabs, as illustrated in Fig. 7 (a). On sulfided mixed Mo_3W_9/Al_2O_3 catalysts, differences in contrast between atoms in the slabs are observed, which can be attributed to the difference in Z between Mo and W (Fig. 7 (b)). Differences in thickness of the support cannot explain these differences as they are never observed on the pure WS_2 supported catalyst. This is confirmed by the intensity profiles in a row of atoms, where the ratio of intensity is equal to the ration of the $Z^{1.7}$ (Fig. 7). It is clearly seen that using of mixed MoW HPA contributed to the formation on mixed $Mo_nW_{12-n}S_2$ particles with core-shell structure, where Mo atoms are located predominantly together in core of the WS_2 slab. That is in agreement with EXAFS results reported in Chapter 2. Haandel et al. [18] also evidenced core-shell structures for Ni-Mo-W mixed catalysts prepared from conventional precursors and sulfided under gas phase sulfidation at 400°C. They proposed through EXAFS analysis that in the sulfided slabs, Mo was mostly located in the core and W atoms in the outer rim.

HAADF images of $(Mo_3+W_9)/Al_2O_3$ catalyst prepared from two separate HPAs show a large majority of monometallic MoS_2 and WS_2 slabs with only few bimetallic particles, in agreement with our EXAFS results.

Conclusions

In this part concerning more deepened characterization of MoW based catalyst, we evidenced by HAADF the formation of mixed Mo-W slabs when using mixed MoW HPA as precursor. This technique allowed for the first time to visualize the location of the atoms in the slabs, molybdenum being in the core of WS_2 slabs. The formation of mixed slabs is in agreement with the XAS results of the final sulfided state presented in the previous chapter, evidencing a Mo-W contribution for theses solids. Contrariwise, both techniques showed the presence of monometallics slabs in the Mo+W solids prepared from the mixture of HPA. The in-situ monitoring of the sulfidation of both solids by QXAS evidenced sulfidation intermediates and pointed out differences in the genesis of the active phase. Indeed formation of WS_2 phase was found to start at lower temperature in Mo_3W_9/Al_2O_3 than in $(Mo_3+W_9)/Al_2O_3$ and W catalysts, being thus simultaneous to Mo sulfidation, which appears to be beneficial to the formation of mixed Mo-W slabs.

In the previous chapter, were presented the catalytic performance of these solids in the HDS of DBT and HYD of naphthalene, after activation under the same conditions than prior to the characterizations (Chap 2, Table 1).

Table 1. Catalytic properties of prepared catalysts in DBT HDS and naphthalene HYD.

Catalysts	DBT HDS (%)	$S_{HYD}/_{DDS}$	Rate constant $k_{HDS} \times 10^{-5}$ (mol h^{-1} g^{-1})	Naphthalene HYD (%)	Rate constant $k_{HYD} \times 10^{-5}$ (mol h^{-1} g^{-1})
Mo$_{12}$/Al$_2$O$_3$	51.9	1.7	45.1	40.5	157.3
W$_{12}$/Al$_2$O$_3$	22.2	2.6	15.5	23.8	82.4
Mo$_3$W$_9$/Al$_2$O$_3$	52.9	3.2	46.4	47.5	195.2
(Mo$_3$+W$_9$)/Al$_2$O$_3$	32.1	1.8	23.9	27.3	96.7

Adding three molybdenum atoms into SiW$_9$ HPA structure led to increase the catalytic activity more than 2.6 times for DBT HDS and 2 times for naphthalene HYD compared to W$_{12}$/Al$_2$O$_3$. Moreover, SiMo$_3$W$_9$ HPA based catalyst had the same activity level as Mo$_{12}$/Al$_2$O$_3$ in HDS and a higher activity in HYD. In contrast, the presence of Mo had almost no effect on catalytic properties of the samples obtained by mixture of two HPAs. Taking into account the results of the characterization of sulfide catalysts, it can be concluded that the MoW nanoscale proximity in the structure of mixed HPAs resulted in the formation of mixed Mo$_n$W$_{12-n}$S$_2$ active phase which is at the origin of higher catalytic activity of the mixed HPAs based catalysts compared to their counterparts prepared from mixture of separate HPAs.

3.2. MoW synergetic effect supported by HAADF for alumina based catalysts prepared from mixed SiMo$_n$W$_{12-n}$ heteropolyacids by liquid sulfidation

After characterization and evaluation of the catalytic properties of MoW based catalysts activated by H$_2$S under gas phase, the same solids were investigated in co-hydrotreating of DBT and naphthalene after activation by DMDS using liquid phase sulfidation. The results of this study are presented below, and were published in Applied Catalysis B.

Conclusions

As observed in the case of activation by H_2S, the solids prepared from the mixed HPA activated with DMDS were more efficient than their counterparts obtained from the mixture of $SiMo_{12}$ and SiW_{12} HPAs. Moreover $SiMo_3W_9$ solid was as efficient as $SiMo_{12}$ in the HDS of DBT and significantly more active in the HYD of naphthalene than SiW_{12}. HAADF analysis revealed the formation of mixed MoW slabs with Mo atoms randomly distributed in WS_2 structure in Mo_3W_9, which formation appeared beneficial to HDS and HYD performance.

3.3. Influence of the sulfidation procedures on the structure of active phase, sulfidation degree and catalytic properties of (Mo)W/Al$_2$O$_3$ catalysts

It is known that the sulfidation of commercial hydrotreating catalysts is performed using organosulfide agents (also called "spiking" agents) (dimethyl sulfide, dimethyl disulfide, polysulfides, etc.). This choice is explained by different reasons, like the high toxicity of H$_2$S, but also by the possibility of organosulfide agents to deliver sulfur gradually to the catalyst through a control of their kinetics of decomposition.

As can be seen from the above results, the activation of the catalysts was performed by two procedures: gas phase (GP) and liquid phase (LP) sulfidation by using H$_2$S and DMDS, respectively. The sulfidation behavior and catalytic properties of the unpromoted (Mo)W catalysts were different depending on the sulfiding agent.

It should be noted that the sulfidation procedures using the different sulfidation agents were not performed under the same conditions. LP sulfidation was performed by heating in hydrogen flow at 3.5 MPa with a mixture of DMDS (2 wt.% of sulfur) in decane. First, the samples were heated up to 240 ºC over a holding period of 10 h and then the temperature was raised up to 340 ºC to be kept as such over 6 h. GP activation was carried out in one step under a flow of a mixture of 10 % of H$_2$S into H$_2$ at atmospheric pressure and heating to 400 ºC over a holding period of 2 h. However, the HDT activity tests were performed using the same model feed in identical conditions in both cases.

Effect on morphology:

It was found that the sulfidation conditions had an impact on the structure of sulfide phase and distribution of metals inside the slabs. The use of mixed SiMo$_3$W$_9$ HPA as initial precursor led to the formation on mixed Mo$_n$W$_{12-n}$S$_2$ particles with Mo atoms inside WS$_2$ slabs in both cases. However, GP sulfidation was more preferable to formation of the particles with core−shell structure, while LP one led to more randomly distribution of molybdenum inside the WS$_2$. In the case of GP sulfidation, the sulfiding agent H$_2$S is present from room temperature and may lead to the formation of partly sulfided intermediate at lower temperature than in the case of DMDS, which decomposition occurs at 150 °C. We can imagine that these intermediates growth is favored under H$_2$S and leads to larger Mo entities than in the case of LP.

In the case of GP Mo atoms start sulfiding at room temperature with formation of MoS$_2$ slabs, when tungsten disulfide appears at higher temperature and could then cover the edges of MoS$_2$ particle resulting in core-shell structure. LP sulfidation led to more randomly distribution of molybdenum inside the WS$_2$ particle. In this case Mo starts sulfiding at temperature of DMDS

decomposition ~150 ℃ a temperature close to the startup sulfidation temperature of W that allows to form mixed sulfide particles with more random atoms distribution inside the slabs.

In bimetallic reference catalysts synthesized by using mixture of separate HPAs the major part of sulfide particles were present as separate monometallic sulfides. Nevertheless, mixed $Mo_nW_{12-n}S_2$ slabs were also observed and their percentage increased when LP sulfidation was performed.

Effect on sulfidation degree:

The effect of sulfidation agents on metal sulfidation degree as determined by XPS is shown in Fig. 8.

Except for Mo_3W_9/Al_2O_3 solid, the activation procedure has little effect on the sulfidation rate with variation evaluated below 9 %. A larger difference in metal sulfidation degree (19 % for both Mo and W) is observed for $SiMo_3W_9$ HPA based catalyst. This could be attributed to the formation of the mixed $MoWS_2$ particles with different structure, more strongly affected by the sulfidation agent resulting in different temperatures of H_2S availability.
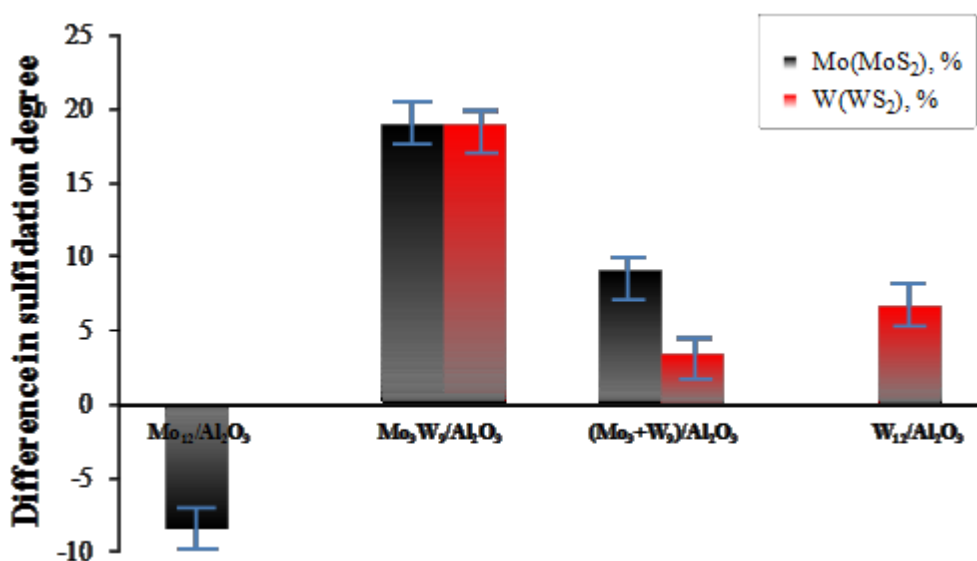
Fig. 8. The effect of sulfidation agents on metal sulfidation degree
(difference between LP and GS sulfidation).

The differences in catalytic properties of the (Mo)W catalysts with respect to the sulfidation procedures are shown in Fig. 9. H_2S activation of all studied samples led to higher HDS and HYD activity than the DMDS activation. Increasing of HDS activity when H_2S was used for sulfidation was reported by Gochi et al. for bulk MoWNi [19] and Nikulshin et al. for

CoMo/Al$_2$O$_3$ catalysts [20]. Conflicting results have been reported in the literature [21] regarding unpromoted Mo/Al$_2$O$_3$.

The greatest effect of the type of sulfidation was observed for monometallic W catalyst, GP activation provides increasing DBT HDS at 9 times and Naphthalene HYD at 7 times compared to this sample activated by LP. HDS activity of bimetallic and monometallic molybdenum catalysts was increased more than 2 times after H$_2$S activation compared to LP sulfidation, while HYD activity increased slightly lower than HDS ~2. However, the trend in distribution of the catalytic properties was kept whatever the activation protocole, and the high efficiency of mixed HPAs based catalysts compared to Mo+W ones can be attributed in both cases to the presence of mixed Mo$_n$W$_{12-n}$S$_2$ active phase, this mixed structure evidenced by HAADF being more favorable for HDS as well HYD catalytic activity.

(a)   (b)
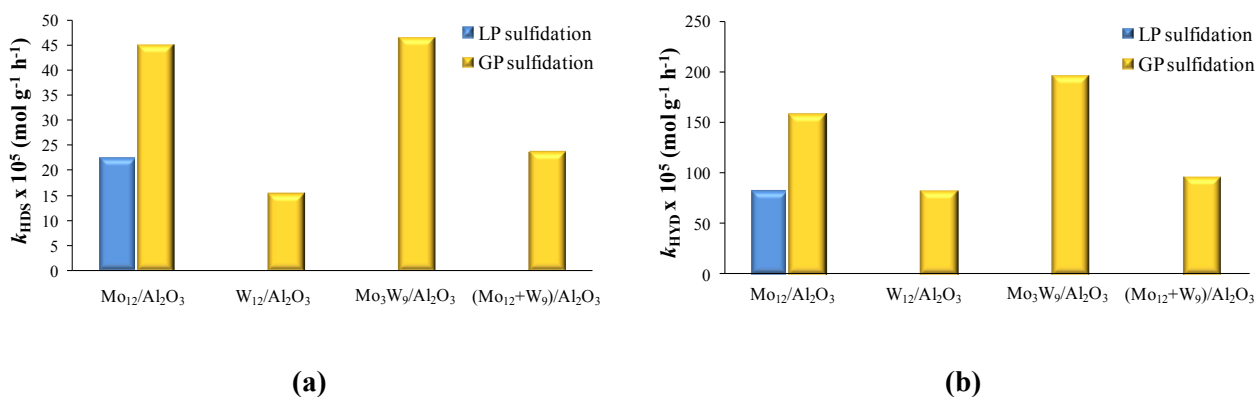
Fig. 9. Rate constants of DBT HDS (a) and naphthalene HYD (b) over (Mo)W/Al$_2$O$_3$ catalysts using GS and LP sulfidation procedures.

Conclusion

Refinement of EXAFS spectra at the Mo and W edges at the end of activation under H_2S evidenced Mo-W contributions at both edges in case of catalysts prepared from mixed $SiMo_3W_9$ HPA, thus demonstrating the formation of a mixed MoW sulfide phase.

HAADF is a relevant technique to visualize Mo and W atoms, as it is based on Z contrast. It allowed for the first time to confirm by direct observation the presence of mixed slabs in the case of Mo_3W_9/Al_2O_3, and moreover to visualize the respective location of Mo and W in the active phase. For mixed Mo_3W_9/Al_2O_3 catalyst sulfided under gas or liquid phase, Mo appeared in both cases inside the WS_2 slabs. A more random distribution of Mo atoms inside the slabs was evidenced for LP sulfidation compared to GP. On $(Mo_3+W_9)/Al_2O_3$, a large majority of separated monometallic slabs is observed, even if some mixed slabs were present particularly under liquid phase activation.

Genesis of the active phase was followed by Quick-XAS in-situ sulfidation, with simultaneous recording of the data at the Mo and W edge. Evolution of sulfidation intermediate was deduced from chemometric method based on multivariate curve regression with alternative least squares. Different evolutions are observed. Formation of WS_2 appears at lower temperature in Mo_3W_9/Al_2O_3 than in $(Mo_3+W_9)/Al_2O_3$, below 200°C against 300°C, inducing a common range of temperature sulfidation for Mo and W in the case of mixed HPA based catalyst favoring the formation of mixed slabs. Structural identification of the sulfidation intermediates is under progress, and will be based on refinement of the corresponding EXAFS data.

Catalytic performances were evaluated in HDS of DBT and naphthalene HYD, after activation under gas and liquid phase. In both case the catalysts prepared from the mixed HPA exhibited significantly higher conversions in the two reactions than their counterparts prepared from mixture of monometallic HPAs. Moreover Mo_3W_9/Al_2O_3, with only 3 atoms of Mo for 9 of W, showed as good performance in HDS as Mo_{12} catalyst with the highest HYD properties of the series. These great results over mixed HPAs based catalysts were achieved due to the formation of mixed $Mo_nW_{12-n}S_2$ active sulfide phase by virtue of close presence of both metals in the initial precursors. At this stage, we can propose that this beneficial effect of the mixed phase could take place through an electronic effect throughout the slabs, thus modifying the efficiency of the active sites. Currently, DFT calculations are in progress, to evaluate the effect of Mo atoms inside a WS_2 slab on the acidic properties of the S-H groups located at the edge.

References

1   C. La Fontaine, L. Barthe, A. Rochet and V. Briois. X-ray absorption spectroscopy and heterogeneous catalysis: Performances at the SOLEIL's SAMBA beamline // *Catal. Today.* –2013. –V.205. –P.148–158.

2   D. Nicosia, R. Prins. The effect of phosphate and glycol on the sulfidation mechanism of CoMo/Al2O3 hydrotreating catalysts: an in situ QEXAFS study // *Journal of Catalysis.* – 2005. –V.231. –P.259–268.

3   A.Rochet, B. Baubet, V. Moizan, C. Pichon, V. Briois, C. R. Co-K and Mo-K edges Quick-XAS study of the sulphidation properties of Mo/Al_2O_3 and $CoMo/Al_2O_3$ catalysts // *Comptes Rendus Chimie.* –2016. –V.19. –P.1337-1351.

4   R. Cattaneo, T. Weber, T. Shido, R. Prins. A Quick EXAFS Study of the Sulfidation of NiMo/SiO2 Hydrotreating Catalysts Prepared with Chelating Ligands // *Journal of Catalysis.* –2000. –V.191. –P.225–236.

5   S.D. Kelly. N. Yang. G.E. Mickelson, N. Greenlay. E. Karapetrova. W. Sinkler, Simon R.Bareb. Structural characterization of Ni–W hydrocracking catalysts using in situ EXAFS and HRTEM // *Journal of Catalysis.* –2009. –V.263 –P. 16–33.

6   V. Schwartz, M. Sun, R. Prins. An EXAFS Study of the Influence of Fluorine on the Structure of Sulfided W/Al_2O_3 and NiW/Al_2O_3 Catalysts // *The Journal of Physical Chemistry B.* – 2002. –V.106, –P. 2597-2605.

7   Marcus G. Martin and J. Ilja Siepmann. Transferable Potentials for Phase Equilibria. 1. United-Atom Description of n-Alkanes // *J. Phys. Chem. B.* –1998. –V.102. – P. 2569-2576.

8   H.W.P. Carvalho, S.H. Pulcinelli, C.V. Santilli, F. Leroux, F. Meneau, V. Briois. XAS/WAXS Time-Resolved Phase Speciation of Chlorine LDH Thermal Transformation: Emerging Roles of Isovalent Metal Substitution // *Chemistry of Materials.* –2013. –V.25 – P.2855.

9   P. Conti, S. Zamponi, M. Giorgetti, M. Berrettoni, W. H. Smyrl. Multivariate Curve Resolution Analysis for Interpretation of Dynamic Cu K-Edge X-ray Absorption Spectroscopy Spectra for a Cu Doped V_2O_5 Lithium Battery // *Analytical Chemistry.* – 2010. –V.82. –P.3629−3635.,

10   W. H Cassinelli, L. Martins, A. R. Passos, S. H. Pulcinelli, C. V. Santilli, A. Rochet, V. Briois. Multivariate curve resolution analysis applied to time-resolved synchrotron X-ray Absorption Spectroscopy monitoring of the activation of copper alumina catalyst // *Catalysis Today.* –2014. –V.229. –P.114−122.

11   A. Voronov, A. Urakawa, W. v. Beek, N. E. Tsakoumis, H. Emerich, M. Rønning. Multivariate curve resolution applied to in situ X-ray absorption spectroscopy data: An efficient tool for data processing and analysis // *Analytica Chimica Acta.* –2014. -V.840. – P.20−27.

12   Carlsson, M. Brorson, H. Topsoe. Supported metal sulphide nanoclusters studied by

HAADF-STEM // *Journal of microscopy.* –2006. –V.223. –P.179-181.

13   L.P. Hansen, Q. M. Ramasse, C. Kisielowski, M. Brorson, E. Johnson, H. Topsoe, S. Helvag, Angew. Atomic-Scale Edge Structures on Industrial-Style MoS_2 Nanocatalysts // *Chemie International Edition.* –2011. –V.50. –P.10153-10156.

14   M. Girleanu, T. Alphazan, Z. Boudene, A. Bonduelle-Skrzypczak, C. Legens, A.-S. Gay, C. Copéret, O. Ersen, P. Raybaud. Magnifying the Morphology Change Induced by a Nickel Promoter in Tungsten(IV) Sulfide Industrial Hydrocracking Catalyst: A HAADF-STEM and DFT Study // *ChemCatChem.* –2014. –V.6. –P.1594-1598.

15   T. Alphazan, A. Bonduelle-Skrzypczak, C. Legens, A.-S. Gay, Z. Boudene, M. Girleanu, O. Ersen, C. Copéret, P. Raybaud, ACS Catal., 2014, 4, 4320-4331.

16   B. Baubet, M. Girleanu, A.-S. Gay, A.-L. Taleb, M. Moreaud, F. Wahl, V. Delattre, E. Devers, A. Hugon, O. Ersen, P. Afanasiev, P. Raybaud. Highly Active Nonpromoted Hydrotreating Catalysts through the Controlled Growth of a Supported Hexagonal WS_2 Phase // *ACS Catalysis.* –2016. -V.6. –P.1081-1092.

17   M. Nikulshina, A.Mozhaev, C. Lancelot, M. Marinova, P. Blanchard, E. Payen, C. Lamonier, P. Nikulshin. MoW synergetic effect supported by HAADF for alumina based catalysts prepared from mixed $SiMo_nW_{12-n}$ heteropolyacids //*Applied Catalysis B: Environmental.* –2018. –V. 224. –P.951–959.

18   L. Van Haandel, M. Bremmer, P. Kooyman, J. A. Rob van Veen, T. Weber, E. J. M. Hensen. Structure–Activity Correlations in Hydrodesulfurization Reactions over Ni-Promoted $Mo_xW_{(1-x)}S_2/Al_2O_3$ Catalysts // *ACS Catalysis.* –2015. –V.5. –P.7276-7287.

19   Y. Gochi, C. Ornelas, F. Paraguay. S. Fuentes, L. Alvarez, J. L. Rico, G. Alonso-Núñez Effect of sulfidation on Mo-W-Ni trimetallic catalysts in the HDS of DBT // *Catalysis Today.* –2005. –V.107–108. –P.531–536.

20   P. A. Nikulshin, A. V. Mozhaev, K. I. Maslakov, A. A. Pimerzin, V. M. Kogan. Genesis of HDT catalysts prepared with the use of $Co_2Mo_{10}HPA$ and cobalt citrate: Study of their gas and liquid phase sulfidation // *Applied Catalysis B: Environmental.* –2014. –V.158–159. – P.161–174.

21   S. Texier, G. Berhault, G. Pérot, V. Harlé, F. Diehl. Activation of alumina-supported hydrotreating catalysts by organosulfides: comparison with H_2S and effect of different solvents // *Journal of Catalysis.* –2004. –V.223. –P.404–418.

Chapter 4

Ni-promoted alumina supported NiMoWS hydrotreating catalysts

A series of alumina supported Mo(W) catalysts promoted by Ni was prepared using Keggin-type heteropolyacids ($H_4SMo_nW_{12-n}O_{40}$) as precursors of active phase by analogy with unpromoted series. The synthesized samples were characterized by N_2 physisorption, XPS and HRTEM. Moreover, XAS and HAADF methods were used for better understanding of the active phase structure of trimetallic NiMoW catalysts. The prepared NiMo(W) catalysts were evaluated in HDS of DBT and in hydrogenation of naphthalene. In addition, the influence of on the catalytic properties of quinoline co-hydrotreated with DBT and naphthalene was investigated.

4.1. Preparation of the supported oxidic precursors

Catalysts with the same surface density of metals d(Mo+W) = 4.2 at/nm^2 were synthesized by the incipient wetness method via impregnation of γ-Al_2O_3 extrudates (S_{BET} = 275 m^2/g, V_p = 0.85 cm^3/g) with aqueous solutions containing the required amounts of HPAs, Ni carbonate and citric acid with molar ratios Ni/(W+Mo) = 0.5 and citric acid/Ni = 1/1. Two trimetallic $NiMo_nW_{12-n}$/Al_2O_3 were prepared by using corresponding mixed HPAs. Two $Ni(Mo_n+W_{12-n})$/Al_2O_3 reference catalysts were also prepared using mixture of monometallic $H_4SiMo_{12}O_{40}$ and $H_4SiMo_{12}O_{40}$ HPAs with a same Mo/W ratio as in mixed ones. Finally, bimetallic $NiMo_{12}$/Al_2O_3 and NiW_{12}/Al_2O_3 based on corresponding monometallic HPAs were synthesized for comparison. After impregnation and maturation, the catalysts were dried at 100 ºC for 10 h in air atmosphere without further calcination. The chemical compositions of the prepared catalysts are given in Table 1.

Table 1

Composition and textural properties of prepared Ni(Mo)W/Al_2O_3 catalysts

Catalyst	NiO (wt %)	MoO$_3$ (wt %)	WO$_3$ (wt %)	Specific surface area (m^2/g)	Pore volume (cm^3/g)	Average pore diameter (Å)
NiMo$_{12}$/Al$_2$O$_3$	4.7	18.0	-	245*	0.61*	8.4
NiW$_{12}$/Al$_2$O$_3$	4.2	-	26.2	275*	0.64*	8.4
NiMo$_1$W$_{11}$/Al$_2$O$_3$	4.3	1.4	24.2	262*	0.60*	8.4
NiMo$_3$W$_9$/Al$_2$O$_3$	4.3	4.2	20.1	256*	0.61*	8.4
Ni(Mo$_1$+W$_{11}$)/Al$_2$O$_3$	4.3	1.4	24.2	258*	0.67*	8.4
Ni(Mo$_3$+W$_9$)/Al$_2$O$_3$	4.3	4.2	20.1	259*	0.66*	8.4

*The values calculated per g of the support.

By comparison with the initial textural properties of alumina (S_{BET} = 275 m^2/g, V_p = 0.85 cm^3/g) only moderate variations were observed after impregnation of the support by metallic solutions and drying. The pore volume reduction is around 25% together with a SSA decrease around 11%, while keeping the same average pore diameter than that of alumina. These observations indicated the absence of large crystallites on the carrier surface that could be able to block the support pores and then largely decrease the SSA. Taking into account the important metallic surface density, 4.2 (Mo+W) atoms/ nm^2, the absence of noticeable evolution of the textural properties of the catalysts witness the formation of well-dispersed oxidic phase with the use of heteropolyacids precursors compared to that of classical precursors known to lead to larger deposits [1-3].

4.2. Characterization of sulfided catalysts

Four characterization techniques were used to characterize the sulfided solids. Firstly the samples were analyzed by EXAFS and HAADF with the aim to investigate after sulfidation of the promoted catalysts the formation of the mixed MoWS slabs as it was observed on unpromoted systems. As the sulfidation was studied by EXAFS under gas phase, the same procedure was used for HAADF. The investigation and quantification of active sites and thus the localization of Ni atoms were followed using TEM and XPS under sulfidation in liquid phase since this procedure was used to evaluate the catalytic properties of the promoted solids.

4.2.1. Study of formation of mixed slabs

4.2.1a. HAADF characterization of LP suldided Ni(Mo)W/Al$_2$O$_3$ catalysts

Sulfided catalysts were characterized by HAADF-STEM for these purposes. As seen for unpromoted solids, due to Z contrast images, the technique of HAADF is a powerful tool allowing recognizing the positions of the metal atoms and their nature, especially between Mo and W atoms offering very different Z numbers. Due to the dark field analysis, on HAADF images, heavy atoms (W) would appear bright while light atoms (Mo) would appear dark. Prior to the HAADF analysis, the catalysts were sulfided in gas phase (GP) at 400 ºC for 2 h in a stream of 10 % of H$_2$S in H$_2$ under atmospheric pressure. Typical HAADF images of sulfided NiMo$_3$W$_9$/Al$_2$O$_3$ and Ni(Mo$_3$+W$_9$)/Al$_2$O$_3$ catalysts are presented in Fig. 1.
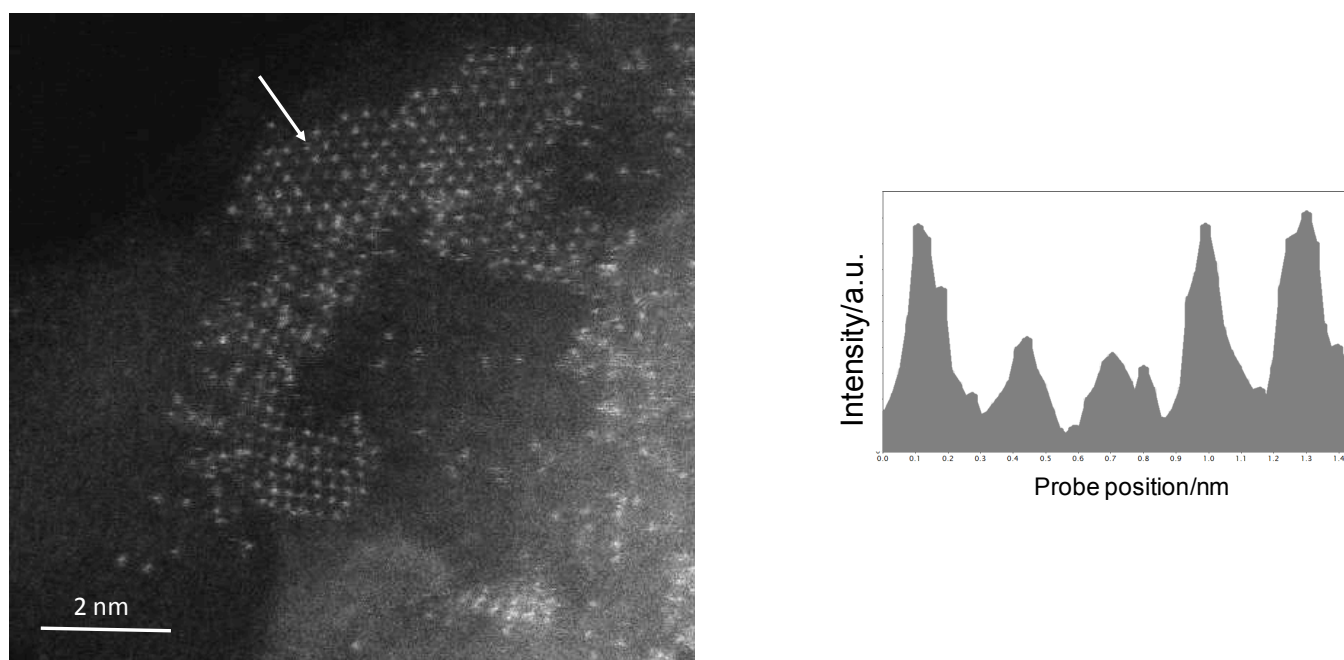
NiMo₃W₉/Al₂O₃
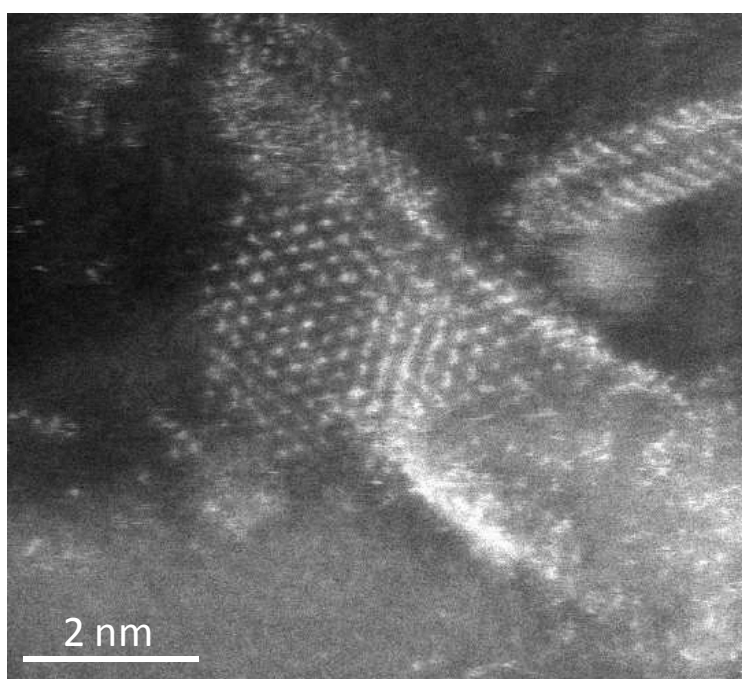
Ni(Mo₃+W₉)/Al₂O₃

Fig. 1. HAADF images of sulfided NiMo$_3$W$_9$/Al$_2$O$_3$ and Ni(Mo$_3$+W$_9$)/Al$_2$O$_3$ catalysts with intensity profiles corresponding to the row of atoms identified by the arrow on NiMo$_3$W$_9$/Al$_2$O$_3$.

The sulfide particles of Ni-promoted catalysts had irregular shapes, as observed in the case of unpromoted samples, due to interaction with alumina surface. HAADF images of NiMo$_3$W$_9$/Al$_2$O$_3$ show that the use of mixed SiMo$_3$W$_9$ HPA led to the formation of mixed MoWS slabs, in which small agglomerates of Mo atoms were surrounded by W ones. Even if mixed MoW slabs are clearly observed in

the case of this promoted catalyst, the atomic repartition in a disulphide slab differs from the core-shell structure of unpromoted Mo_3W_9/Al_2O_3 catalyst (sulfided with the same procedure) containing a whole Mo core. This situation is more similar to the one that have been observed with unpromoted Mo_3W_9/Al_2O_3 sulfided under liquid phase. The active phase of $Ni(Mo_3+W_9)/Al_2O_3$ sulfided under gas phase consisted mainly of homogeneous monometallic slabs. But the presence of mixed slabs was also evidenced, their number seeing to be a little bit higher than in corresponding unpromoted catalyst. This situation is thus in this case quite similar to what have been observed with unpromoted $(Mo_3+W_9)/Al_2O_3$ sulfided under gas phase or liquid phase.

HAADF shows then unambiguously the formation of the mixed slabs for Ni promoted mixed HPA based catalysts with more random distribution of both metals. In promoted catalysts prepared from mixture of monometallic slabs are mainly identified with few mixed slabs also present.

4.2.1b. EXAFS characterization of GP suldided Ni(Mo)W/Al$_2$O$_3$ catalysts

Quick EXAFS was employed to follow the sulfidation of Mo, W and Ni in alumina supported trimetallic hydrotreating catalysts. The Quick EXAFS measurements were carried out at the ROCK beamline at Synchrotron SOLEIL. Sulfidation was performed in a flow of 10 % H_2S in H_2 at atmospheric pressure from RT to 400 °C with a heating rate of 3 °C/min. Spectra were recorded in transmission mode at the Mo K-edge (20000 eV), W L_{III} edge (10207 eV) and at the Ni K-edge (8333 eV). The detailed structural characterization of $Ni(Mo)W/Al_2O_3$ catalysts after sulfidation was investigated. The Fourier transform moduli data recorded for the sulfided catalysts are presented in Fig. 2 and the corresponding fit EXAFS parameters are gathered in Table 2 and 3. The corresponding magnitude of the Fourier transform of the Mo K edge and W L_{III} edge spectra and of the best models obtained by fitting are shown in Fig. S1 (Supporting information for Chapter 4).

Mo K edge
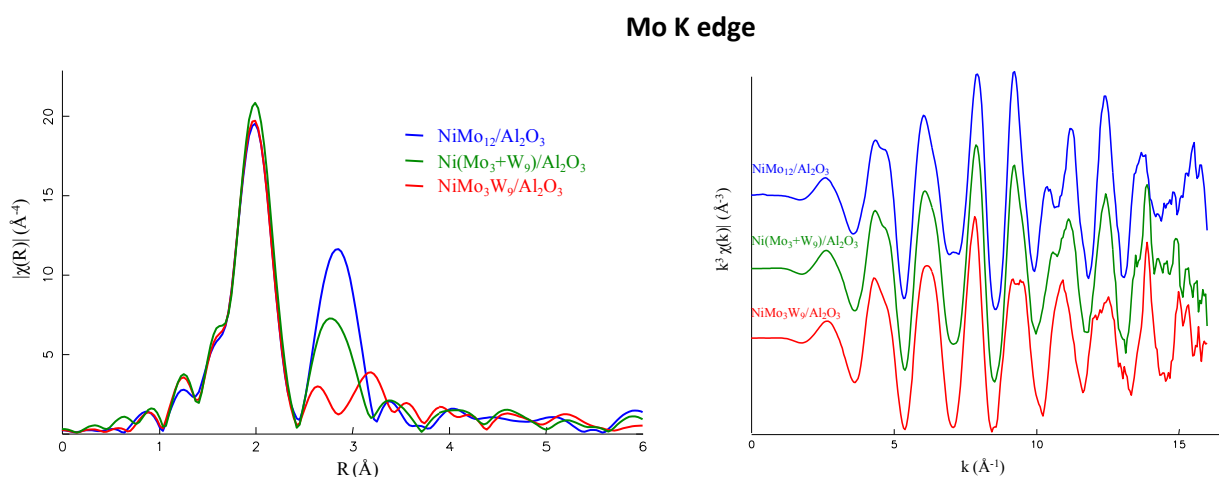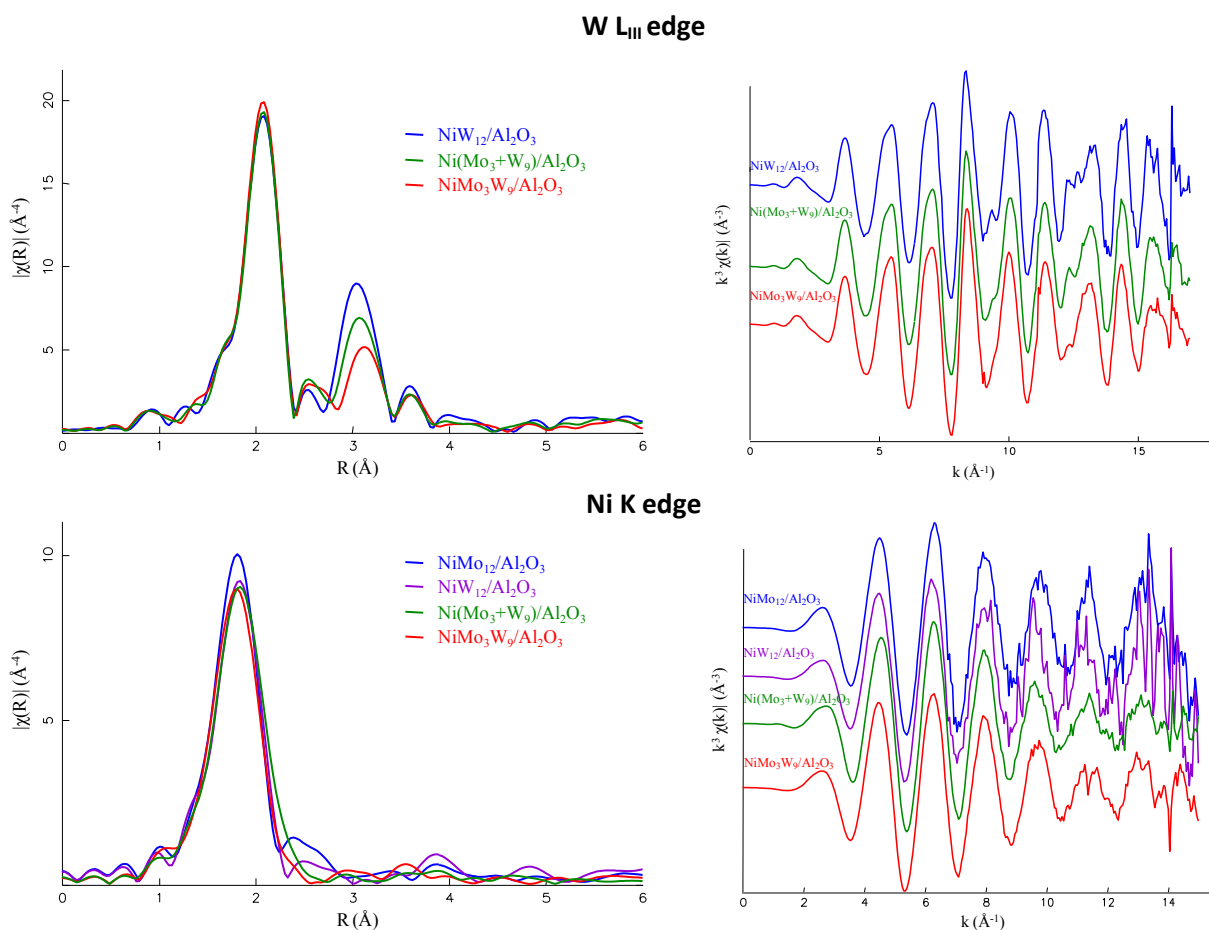
W L$_{III}$ edge

Ni K edge

Fig. 2. EXAFS at the Mo and Ni K edges and W L$_{III}$ edge and the corresponding Fourier transforms of sulfided Ni(Mo)W/Al$_2$O$_3$ catalysts.

Table 2

Mo K edge EXAFS results obtained by multi-edge fitting. k-range 3-14 Å^{-1}, R-range 1.4-3.4 Å, S$^2_0$ = 1.00.

Catalyst	Shell	N	R (Å)	$\sigma^2 \times 10^3$ (Å²)	E$_0$ (eV)	R-factor
NiMo$_{12}$/Al$_2$O$_3$	Mo − S	5.5±0.4	2.41 ± 0.01	3.4 ±0. 6	2.08 ±0.6	0.0029
	Mo-Mo	3.8±0.6	3.18 ±0.01	4.2 ±0.8		
NiW$_9$Mo$_3$/Al$_2$O$_3$	Mo-S	5.6 ±0.6	2.42 ±0.01	3.4 ±0.7	2.42 ±0.97	0.0123
	Mo-Mo	1.4 ±0.5	3.18 ±0.01	4.8 ±2.2		
	Mo-W	3.1 ±1.2	3.18 ±0.01	4.8 ±2.2		
Ni(Mo$_3$+W$_9$)/Al$_2$O$_3$	Mo-S	5.9±0.6	2.41 ±0.01	3.4±0.6	1.81 ±1.28	0.0092
	Mo-Mo	3.9±1.7	3.17 ±0.01	6.8±2.7		

Table 3

W L_{III} edge EXAFS results obtained by multi-edge fitting. k-range 4.1-14.5 $Å^{-1}$, R-range 1.4-3.43 Å, $S^2_0 = 0.84$.

Catalyst	Shell	N	R (Å)	$\sigma^2 \times 10^3$ ($Å^2$)	E_0 (eV)	R-factor
NiW$_{12}$/Al$_2$O$_3$	W-S	5.8±0.7	2.41 ±0.01	3.0±0.9	7.66±1.60	0.0105
	W-W	4.3 ±1.1	3.17 ±0.01	4.3±1.0		
NiW$_9$Mo$_3$/Al$_2$O$_3$	W-S	6.0 ±0.8	2.42 ±0.01	2.9±1.0	9.96±1.85	0.0123
	W-W	2.7 ±1.7	3.18±0.01	4.8 ±2.2		
	W-Mo	0.5 ±3.0	3.18 ±0.01	4.8 ±2.2		
Ni(Mo$_3$+W$_9$)/Al$_2$O$_3$	W-S	5.5±0.6	2.41±0.01	2.8±0.7	9.05±1.65	0.0092
	W-W	3.3±1.2	3.17±0.01	4.2± 1.6		

The first contributions in the Fourier transforms of the EXAFS at the Ni K-edge of the catalysts, at around 2 Å (phase-shift not corrected) is assigned to Ni-S [4] contributions. Works are still under progress to see if it is possible to rather link this contribution to a promoted NiMoS (or NiWS) than to a Ni sulfide contribution (Ni$_3$S$_2$). As in the case of unpromoted (Mo)W/Al$_2$O$_3$ catalysts the contributions of Mo-S and W-S were observed around 1.9 Å (phase-shift not corrected). The coordination number for Mo−S (W−S) and contributions were found ~ 5.6 for all studied samples. The second shell contributions around 3 Å (phase-shift not corrected) at both edges were assigned to metal backscatter within the Mo(W)S$_2$ structure. At both edges (Fig. 2), noticeable decrease can be noticed in the second coordination shell when comparing MoW catalysts to NiMo$_{12}$ and NiW$_{12}$ catalysts Fourier Transforms, in particular for mixed HPA based catalysts. As already observed in the case of unpromoted samples, the second coordination shell was more modified for Mo$_3$W$_9$HPA based catalyst compared to that of Ni(Mo$_3$+W$_9$)/Al$_2$O$_3$. This larger decrease indicates a greater presence of W surrounding Mo in agreement with the HAADF results which have shown that the use of mixed HPAs was leading to high amount of MoWS slabs, while the use of separate SiMo$_{12}$ and SiW$_{12}$ HPAs was mainly leading to separate MoS$_2$ and WS$_2$ slabs.

In fact refinements (Tables 2 and 3) indicate that for trimetallic catalyst prepared from mixture of two HPAs only one metal-metal contributions is obtained in second coordination shell, with a Mo-Mo coordination number equal to 3.9 at the Mo edge and a W-coordination number equal to 3.4 at the Wedge for (Mo$_3$+W$_9$)/Al$_2$O$_3$. At the Mo edge, this coordination number, similar to that obtained in NiMo$_{12}$/Al$_2$O$_3$ catalyst, could indicate the formation of MoS$_2$ slabs with morphology close to that in NiMo$_{12}$/Al$_2$O$_3$ catalyst. At the W edge a lower W-W coordination number is observed compared to that of NiW$_{12}$ catalyst (4.3 versus 3.4). The morphology of WS$_2$ slabs could thus be affected by the presence of Mo without identification of a W-Mo contribution. The same evolution of coordination number was also observed for the corresponding unpromoted catalysts showing that the behavior does not depend on the Ni promotion. In the two trimetallic mixed catalyst, at the Mo edge the addition of a Mo−W scattering path significantly

improved the fit confirming unambiguously the formation of mixed $(MoW)S_2$ slabs. However, contrary to the results of unpromoted catalysts presenting close Mo-Mo and Mo-W coordination number, these coordination numbers for NiW_9Mo_3/Al_2O_3 and $NiW_{11}Mo_1/Al_2O_3$ are different with largely higher value for Mo-W coordination number. It could be related to HAADF images revealing core-shell structure with a large Mo core for unpromoted catalyst while smaller islands of Mo surrounding by W atoms were observed in the mixed $(MoW)S_2$ slabs of Ni promoted catalyst. The scheme 1 shows that effectively Mo atoms have more W neighbors in the case of formation of Mo islands. We can noticed that from the W side, in mixed HPA based catalysts, a W-Mo contribution is also necessary to improve the fit of the W-Mo coordination values are obtained with high uncertainty.

(a) **(b)**
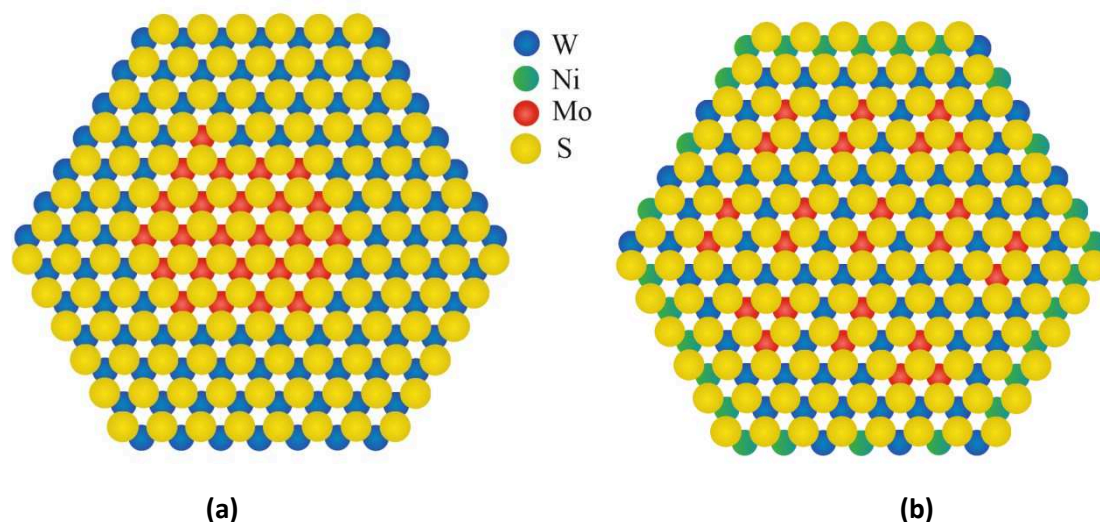
Scheme 1. Top view of structural models for the Mo_3W_9 (a) and $NiMo_3W_9$ (b) catalysts activated by GP sulfidation. These models based on HAADF results and the coordination numbers of metal-metal contributions according to EXAFS fit.

Conclusions

The characterizations under gas phase sulfidation have proven that the promotion of the MoW catalysts does not inhibit the formation of the mixed MoWS slabs when the oxidic precursors are prepared from mixed HPAs containing both Mo and W atoms. Promotion of the catalysts prepared from a mixture of HPA leads to small change because few mixed slabs are now observed besides separate MoS_2 and WS_2 slabs.

4.2.2. Evaluation of the number of active sites

4.2.2a. HRTEM characterization of LP suldided Ni(Mo)W/Al$_2$O$_3$ catalysts

HRTEM studies allow to obtain general morphological information with individual S–Mo(W)–S layers images when the disulfide slabs are oriented parallel to the electron beam. However, this technique does not allow distinguishing between NiMoS, NiWS or NiMoWS slabs due to the lack of a contrast between elements. Liquid phase sulfided Ni(Mo)W/Al$_2$O$_3$ catalysts were characterized by HRTEM in order to obtain information about the dispersion of the active phase particles, i.e. their length and their stacking. For this characterization, the oxidic samples were sulfided by liquid phase sulfidation (LP) in a stepwise protocol conducted over 10 h at 240 ºC and 8 h at 340 ºC using a mixture of DMDS (2 wt. % of sulfur) and decane at 3.5 MPa. Typical micrographs, which show the typical fringes due to Ni(Mo)WS crystallites with 0.65 nm interplanar distances, are presented Fig. 3.
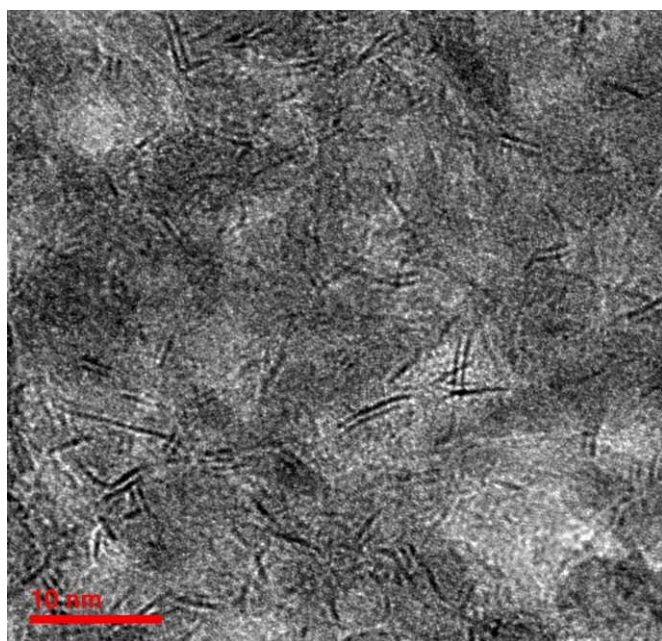
NiMo$_{12}$/Al$_2$O$_3$ NiW$_{12}$/Al$_2$O$_3$
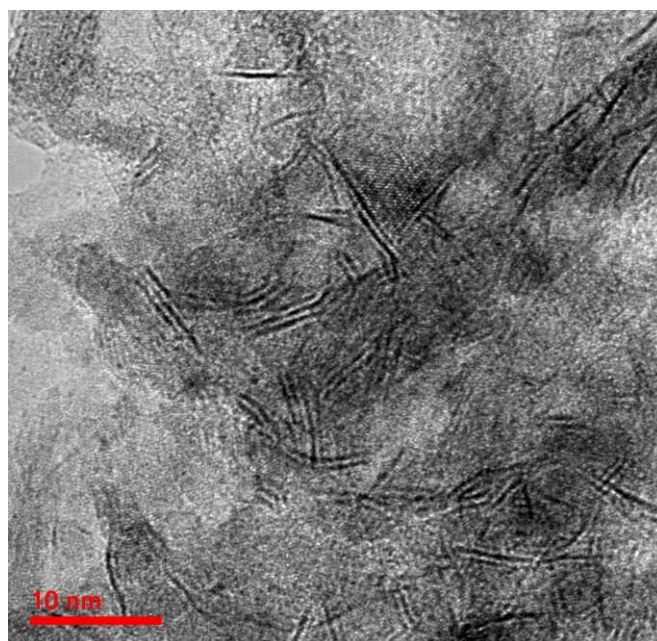
$$NiMo_3W_9/Al_2O_3 \qquad\qquad Ni(Mo_3+W_9)/Al_2O_3$$
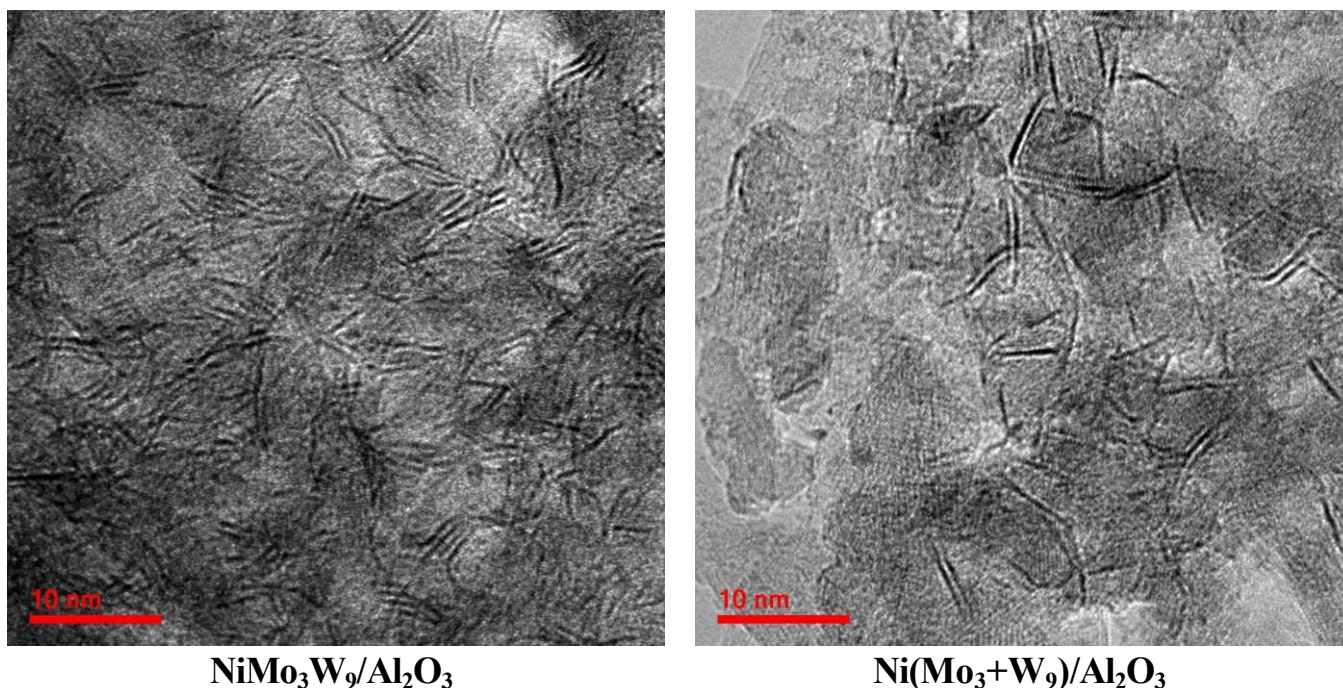
Fig. 3. HRTEM micrographs of sulfided $Ni(Mo)W/Al_2O_3$ catalysts.

Distributions in stacking degree and slab length of the samples as well as the corresponding average values are presented in Table 4. The HRTEM data allowed us to calculate the average dimension of the $NiMo(W)S$ phase particles. $NiMo_{12}/Al_2O_3$ had the slabs with the shortest length ~3.4 nm among all studied catalysts and the average stacking number 1.6. NiW_{12}/Al_2O_3 catalyst consisted predominantly the slabs with length ~ 3.9 nm and stacking number ~ 2.1. Obtained values are in agreement with the results reported in [5] showing that NiW particles are usually larger than NiMo ones. Adding one Mo atom to SiW_9 HPA had no effect on the average slab length and stacking number. Three molybdenum atoms addition resulted to little decrease in average length (from 3.9 to 3.6 nm) and average stacking number (from 2.1 to 1.8). For both trimetallic references catalysts (Ni(Mo+W), the morphologies of the slabs are almost the same to that of the corresponding catalysts prepared with mixed HPAs. Nevertheless, the stacking of $Ni(Mo_3+W_9)/Al_2O_3$ ($\overline{N}$ =1.4) seems to be lower than that of $NiMo_3W_9/Al_2O_3$ ($\overline{N}$ =1.8).

The theoretical average stacking (weighted average of the stacking of $NiMo_{12}$ and NiW_{12}) were calculated for both trimetallic samples: for the two synthesis (mixed HPA or mixture), the calculated values obtained are almost identical (~ 2) which means that the decrease in the average stacking observed for $Ni(Mo_3+W_9)/Al_2O_3$ cannot be used to conclude on the formation of separate NiMoS and NiWS particles (or mixed slabs) after liquid phase sulfidation. The stacking decrease for $Ni(Mo_3+W_9)/Al_2O_3$ should originate from another process.

Table 4

Morphological characteristics of the Ni(Mo)WS active phase species calculated from TEM micrographs.

Catalyst	Average length $\overline{l}$ (nm)	Average stacking number $\overline{N}$	Distribution of slab length (rel. %)					Distribution of stacking number (rel. %)			
			<2 (nm)	2-4 (nm)	4-6 (nm)	6-8 (nm)	>8 (nm)	1	2	3	>3
NiMo$_{12}$/Al$_2$O$_3$	3.4	1.6	13	62	21	4	0	40	57	3	-
NiW$_{12}$/Al$_2$O$_3$	3.9	2.1	3	52	40	4	1	30	38	27	5
NiMo$_1$W$_{11}$/Al$_2$O$_3$	3.9	2.1	6	50	37	6	1	32	44	19	4
NiMo$_3$W$_9$/Al$_2$O$_3$	3.6	1.8	12	55	29	2	2	36	48	13	3
Ni(Mo$_1$+W$_{11}$)/Al$_2$O$_3$	3.7	1.9	3	53	38	3	3	39	38	20	3
Ni(Mo$_3$+W$_9$)/Al$_2$O$_3$	3.6	1.4	9	54	33	2	2	65	28	5	2

By comparison with the active phase morphology of unpromoted catalysts, promotion of Mo(WS)$_2$ phase by Ni decreased the average slab length due to the decorating action of the Ni atoms, which fixed on the edges of Mo(W)S$_2$ during the formation of the disulfide slabs hindering their further growth. The same effect of promoter atoms on the length of the crystallites was reported in several studies [6-8]. In mixed catalysts, the average length decreased from 4.4 to 3.9 nm and from 4.8 to 3.6 nm for NiMo$_1$W$_{11}$/Al$_2$O$_3$ and NiMo$_3$W$_9$/Al$_2$O$_3$, respectively compared to their unpromoted counterparts. A most significant reduction of length ~ 1.5 nm was noticed in the catalysts prepared from mixture of two HPAs. In addition, Ni-promoted W containing catalysts showed slightly higher stacking degree of particles than their unpromoted counterparts.

4.2.2b. XPS characterization of LP suldided Ni(Mo)W/Al$_2$O$_3$ catalysts

The species formed after catalyst LP sulfidation have been analyzed by XPS. Fig. 4 shows the decomposition of Ni2p, Mo3d-S2s and W4f photoelectron spectra recorded for Ni(Mo)W/Al$_2$O$_3$ catalysts. The spectral region of Ni2p$_{3/2}$ (Fig. 4a) contains three peaks with their respective satellites. The peak at a BE of 853.7 eV is related to Ni(Mo)WS phase. The signals at 852.9 eV and 856.5 eV correspond to the NiS species and Ni^{2+} in an oxidic environment, respectively [9-13]. The results of decomposition of Mo3d (Fig. 4b) and W4f (Fig. 4c) spectra correspond to those described for unpromoted catalysts (Chapter 3). The decomposition of the XPS spectra revealed the relative amount of nickel, molybdenum and tungsten species present on the surface of the sulfided catalysts (Table 5).

Fig. 4 (a). Decomposition of XPS of the Ni2p spectra recorded for the Ni(Mo)W/Al$_2$O$_3$ catalysts; in blue: Ni^{2+} oxide contributions; in green: NiS contributions; in black: Ni(Mo)WS phase contributions.

Fig. 4 (b). Decomposition of XPS of the Mo3d spectra recorded for the Ni(Mo)W/Al$_2$O$_3$ catalysts; in blue: Mo^{6+} oxide contributions; in green: MoS$_x$O$_y$ contributions; in black: MoS$_2$ contributions.

NiW$_{12}$/Al$_2$O$_3$

NiMo$_1$W$_{11}$/Al$_2$O$_3$

NiMo$_3$W$_9$/Al$_2$O$_3$

Ni(Mo$_1$+W$_{11}$)/Al$_2$O$_3$
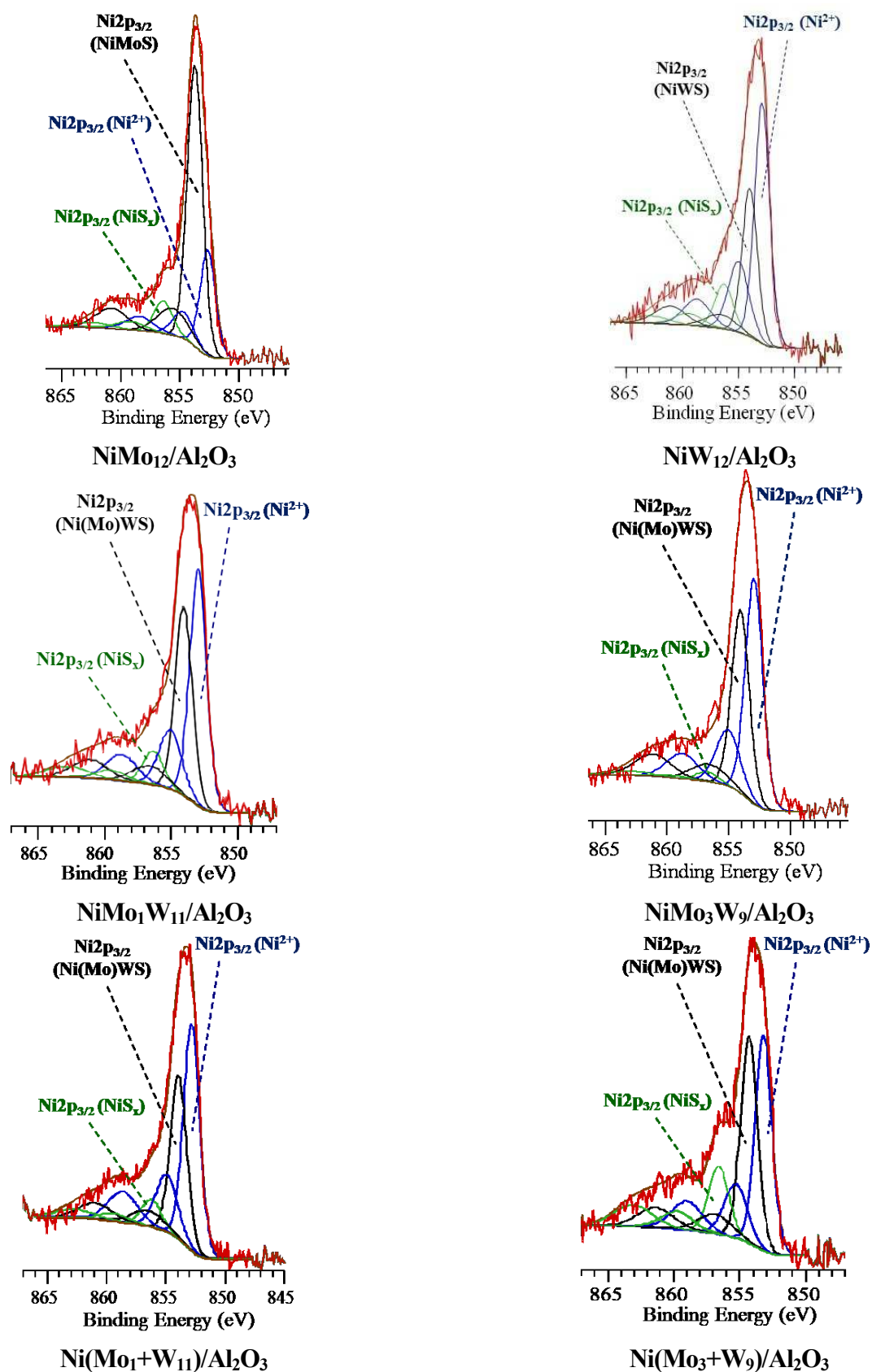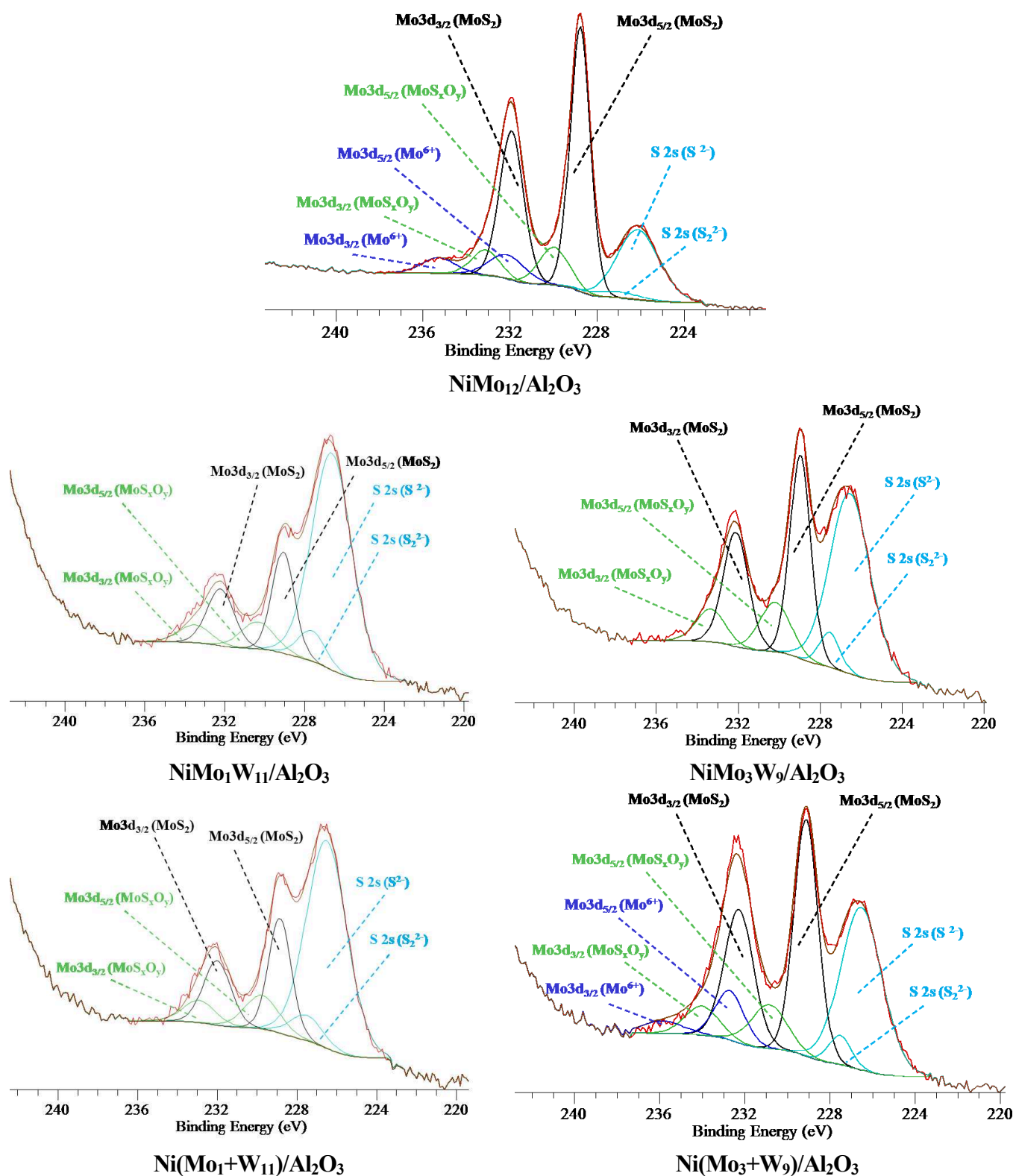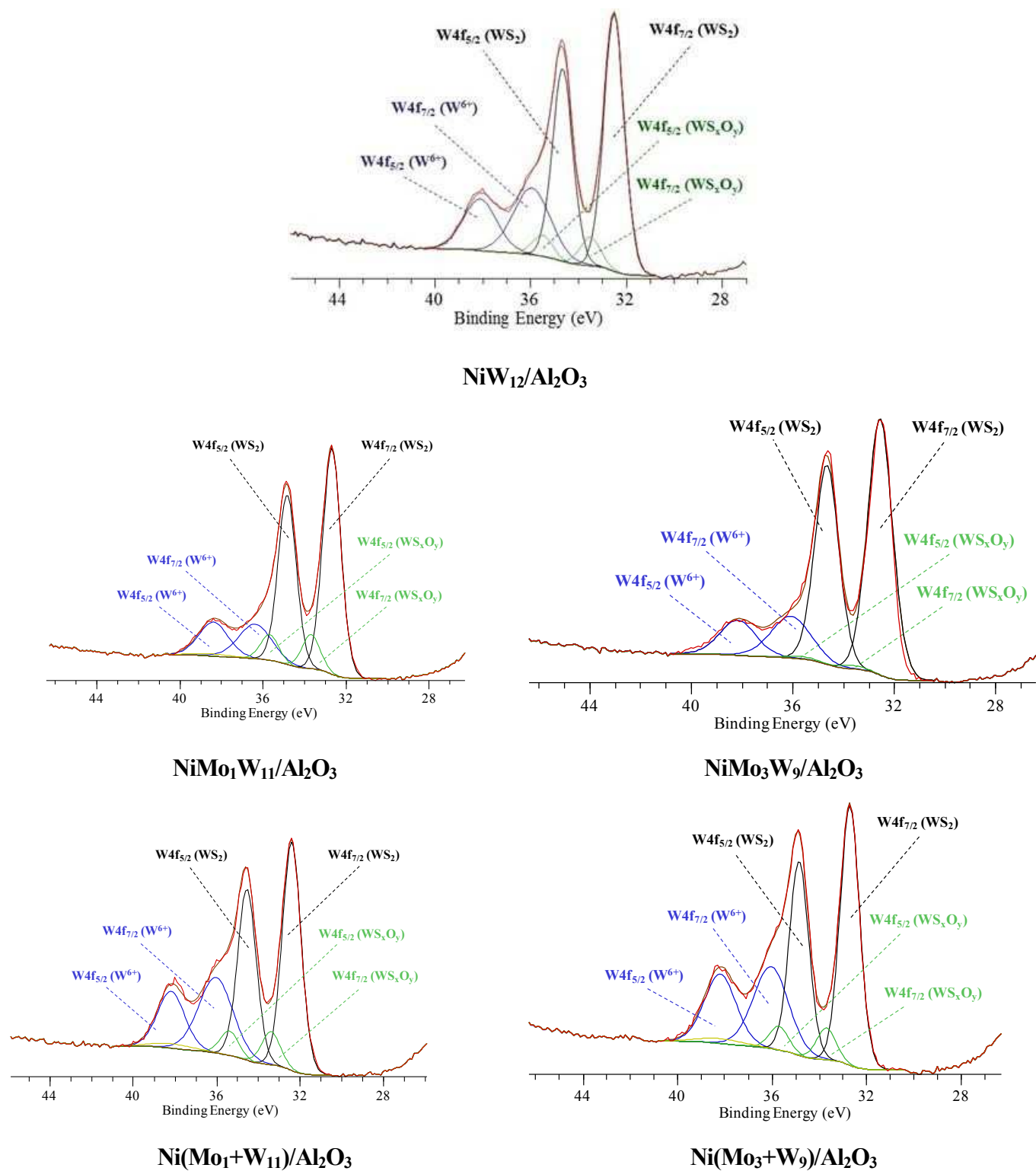
Ni(Mo$_3$+W$_9$)/Al$_2$O$_3$

Fig. 4 (c). Decomposition of XPS of the W4f spectra recorded for the Ni(Mo)W/Al$_2$O$_3$ catalysts; in blue: W^{6+} oxide contributions; in green: WS$_x$O$_y$ contributions; in black: WS$_2$ contributions.

Table 5

Metal fractions measured by XPS for molybdenum and tungsten species present at the surface of LP sulfided Ni(Mo)W/Al$_2$O$_3$ catalysts.

Catalyst	Mo fraction (rel. %)			W fraction (rel. %)			Ni fraction (rel. %)		
	MoS$_2$	MoS$_x$O$_y$	Mo^{6+}	WS$_2$	WS$_x$O$_y$	W^{6+}	Ni(Mo)WS	NiS	Ni^{2+}
NiMo$_{12}$/Al$_2$O$_3$	73	15	12	-	-	-	62	27	11
NiW$_{12}$/Al$_2$O$_3$	-	-	-	64	7	29	30	56	14
NiMo$_1$W$_{11}$/Al$_2$O$_3$	72	28	0	69	10	21	37	51	12
NiMo$_3$W$_9$/Al$_2$O$_3$	74	26	0	74	8	18	42	54	5
Ni(Mo$_1$+W$_{11}$)/Al$_2$O$_3$	70	30	0	59	9	33	35	55	10
Ni(Mo$_3$+W$_9$)/Al$_2$O$_3$	67	19	14	59	7	34	36	43	21

The sulfidation degree of molybdenum was close in all Mo containing samples (~71 rel. %) and varied less than 10 %. Addition of promoter atoms to bimetallic catalysts led to decreasing of molybdenum sulfidation degree at ~ 30 rel. %. In contrast, the W sulfidation degree was lower than those obtained for Mo. The catalysts prepared by using mixed MoW HPAs had the highest W sulfidation degree. Incorporation of one and three molybdenum atoms into the structure of HPA led to an increase in W content in WS$_2$ phase compared to NiW catalyst from 64 to 69 and 74 rel. %, respectively. On the contrary, both corresponding NiMoW references sample demonstrated the lowest W sulfidation degree (59 rel. %) and quantity of molybdenum had no effect. Obtained results could be explained from the genesis of mixed NiMoWS phase which is favored in the case of mixed molecular precursors. The sulfidation of Mo at low temperature could facilitate the sulfidation of W atoms which are enclosed in the same molecular entities. Presence of Ni had weaker effect on decreasing of W sulfidation degree, than on Mo one. Thus, the content of WS$_2$ decreased at ~ 5 rel. % for mixed HPAs based catalysts and at ~ 12 rel. % for trimetallic references. Only for bimetallic NiW catalyst the WS$_2$ amount was increased with promoter addition, that agrees with the results reported in [7,14,15].

XPS decompositions allow quantifying the 3 well admitted Ni phases after sulfidation, i.e. Ni^{2+} in the NiMo(W)S active phase, Ni^{2+} in nickel sulfide (Ni$_2$S$_3$ or NiS) and non sulfided Ni^{2+} ions localized in the alumina lattice but do not allow to distinguish separate NiMoS and NiWS or NiMoWS phases. The highest and lowest concentrations of Ni(Mo)WS phase were obtained for bimetallic catalysts NiMo$_{12}$/Al$_2$O$_3$ (62 rel. %) and NiW$_{12}$/Al$_2$O$_3$ (30 rel. %), respectively. Replacing of one and three tungsten atoms to molybdenum in SiW$_{12}$ HPA structure

led to raise Ni(Mo)WS content compared to NiW_{12}/Al_2O_3 catalyst from 30 rel. % to 37 rel. % for $NiMo_1W_{11}/Al_2O_3$ and 42 rel. % for $NiMo_3W_9/Al_2O_3$. Both samples synthesized from two separate HPAs had also higher content of Ni(Mo)WS phase ($\sim$ 35%) than that in NiW_{12}/Al_2O_3. The amount of substituted Mo had no effect on Ni(Mo)WS %.

Concerning the two other Ni species, excepted for NiMo solid, the main species is always the NiS one (about or more than 50% of the Ni) and only about 10-20% of non sulfided Ni in oxidic environment is observed. That means that more than 80-90 % of Ni is sulfided which may be due to the addition of citric acid introduced in the impregnating solution for the preparation of the oxidic precursors. This compound is known to chelate the Ni ions, to improve their dispersion of Ni species on the support, to decrease the interaction of the Ni ions with the support and thus to improve the sulfidation of Ni. However, as about 60 rel. % of the sulfided Ni is implied in pure nickel sulfide species, that could mean that all the edge and corner sites are fully occupied by Ni, the excess of sulfided Ni remaining at the surface under NiS species. The study of the global Ni/(Mo+W) atomic ratio and of the effect of citric acid in such systems is needed to understand these points. It has been reported in literature that the optimal experimental Ni/W ratio was about 0.3 which could explain the large amount of Ni sulfide species [11].

4.2.2c.Quantification and Ni substitution rate

Quantification of the number of active promoted sites was done using the values obtained by TEM and XPS. First the chemical composition (in molar percentage) of the sulfided solids was determined by XPS (Table 6). Indeed only the metals that can be detected by XPS can be involved in the formation of the active phase [16].

Table 6

Surface chemical composition of LP sulfided Ni(Mo)W/Al$_2$O$_3$ catalysts as estimated by XPS (after removal of C loading).

Catalyst	Concentration (% mol)				
	Ni	Mo	W	S	Al
$NiMo_{12}/Al_2O_3$	0.61	1.69	0	3.59	30.4
NiW_{12}/Al_2O_3	0.51	0	0.83	2.69	31.3
$NiMo_1W_{11}/Al_2O_3$	0.63	0.22	1.15	4.10	33.4
$NiMo_3W_9/Al_2O_3$	0.67	0.56	0.87	4.23	31.3
$Ni(Mo_1+W_{11})/Al_2O_3$	0.60	0.25	1.12	3.56	33.1
$Ni(Mo_3+W_9)/Al_2O_3$	0.68	0.53	0.88	3.79	31.5

Table 7 presents the XPS and theoretical (calculated from the theoretical amount of metals) atomic ratios nMo/nAl, nW/nAl and nNi/nAl. These ratios permit to estimate the dispersion of the metals at the alumina surface. At the surface whatever the catalyst, almost the whole quantity of Mo is detected by XPS while only less than half of W and Ni atoms are detected. Works are under progress on the dispersion of the oxidic catalysts to explain this behavior.

Table 7

XPS and theoretical atomic ratios nMo/nAl, nW/nAl and nNi/nAl.

Catalyst	nMo/nAl XPS	nMo/nAl theo	nW/nAl XPS	nW/nAl theo	nNi/nAl XPS	nNi/nAl theo
NiMo$_{12}$/Al$_2$O$_3$	0.056	0.083	/	/	0.020	0.042
NiW$_{12}$/Al$_2$O$_3$	/	/	0.027	0.084	0.016	0.041
NiMo$_1$W$_{11}$/Al$_2$O$_3$	0.0066	0.0071	0.034	0.077	0.018	0.042
NiMo$_3$W$_9$/Al$_2$O$_3$	0.018	0.021	0.028	0.063	0.021	0.041
Ni(Mo$_1$+W$_{11}$)/Al$_2$O$_3$	0.0076	0.0071	0.034	0.077	0.018	0.042
Ni(Mo$_3$+W$_9$)/Al$_2$O$_3$	0.017	0.021	0.028	0.063	0.022	0.041

Table 7 presents the results of calculations that were done taking into account the amount of metals that are present when considering 10^{22} atoms of catalysts. These calculations permitted to obtain the numbers of Mo and W atoms involved in the formation of the active particles and to determine the number of Ni atoms that are localized in the promotion position. Taking into account the well admitted geometrical model of Kasztelan et al. [17], which has shown that the hexagonal shape of the slabs is the most representative model for modelling the numbers of active sites per slab. It was thus possible thanks to the TEM measurements (average length of the slabs) to calculate for each solid the Ni substitution rate, which represents the fraction of Mo or W replaced by Ni on the edges and corners of an average slab.

Table 8

Quantification of the numbers of promoted active sites and of the Ni substitution rate (fraction of Mo or W replaced by Ni on the edges and corners in average slab). Calculation based on 10^{22} atoms of catalysts taking into account the XPS chemical analysis.

	$NiMo_{12}$	NiW_{12}	$NiMo_1W_{11}$	$NiMo_3W_9$	$Ni(Mo_1+W_{11})$	$Ni(Mo_3+W_9)$
Number of Mo	$1.69.10^{20}$	0	$0.22.10^{20}$	$0.56.10^{20}$	$0.25.10^{20}$	$0.53.10^{20}$
Number of W	0	$0.83.10^{20}$	$1.15.10^{20}$	$0.87.10^{20}$	$1.12.10^{20}$	$0.88.10^{20}$
Number of Ni	$0.61.10^{20}$	$0.51.10^{20}$	$0.63.10^{20}$	$0.67.10^{20}$	$0.60.10^{20}$	$0.68.10^{20}$
% MoS_2	73	-	72	74	70	67
% WS_2	-	64	69	74	59	59
% Ni(W)MoS	62	30	37	42	35	36
Number of Mo in MoS_2 (X)	$1.23.10^{20}$	0	$0.16.10^{20}$	$0.41.10^{20}$	$0.18.10^{20}$	$0.36.10^{20}$
Number of W in WS_2 (Y)	0	$0.53.10^{20}$	$0.79.10^{20}$	$0.64.10^{20}$	$0.66.10^{20}$	$0.52.10^{20}$
Number of Ni in Ni(W)MoS (T)	$0.38.10^{20}$	$0.15.10^{20}$	$0.23.10^{20}$	$0.28.10^{20}$	$0.21.10^{20}$	$0.24.10^{20}$
Number of Mo+W+ Ni in the slabs (X+Y+T)	$1.61.10^{20}$	$0.68.10^{20}$	$1.18.10^{20}$	$1.33.10^{20}$	$1.05.10^{20}$	$1.12.10^{20}$
Slab size (Å)	34 Å	39 Å	39 Å	36 Å	37 Å	36 Å
Number of atoms per slab (N)	114	147	147	127	134	127
Number of edge + corner atoms (N_{b+c})	34	39	39	36	37	36
Number of slabs (Z) = (X+Y+T)/(N)	$1.41.10^{18}$	$0.46.10^{18}$	$0.80.10^{18}$	$1.05.10^{18}$	$0.78.10^{18}$	$0.88.10^{18}$
Number of Ni per slabs (C) = (T)/(Z)	27	32-33	29	27	27	27
Substitution Rate (C)/(N_{b+c})	0.8±0.3	0,8±0,3	0,7±0,3	0,8±0,3	0,7±0,3	0,8±0,3

Table 8 shows that the number of promoted active sites obtained for the solids prepared from mixed HPAs or from mixtures of two HPAs (T in Table 8) is higher compared to NiW_{12}/Al_2O_3. This result is due either to the relative Ni % into the NiMo(W)S phase as determine by decomposition of the Ni2p XPS spectra, either to the amount of Ni detected by XPS. Indeed for NiW_{12}/Al_2O_3 the amount of W and Ni detected by XPS is lower than expected.

When looking at the Ni substitution rate, similar values are obtained for all solids. This value, about 0.8, corresponds to the substitution by Ni of all the W (or Mo) located on the S-edge of a slab and to the substitution of half of the W (or Mo) located on the metallic edge [18].

Conclusions

In the present work, NiMoW catalysts supported on alumina were prepared by co-impregnation of Ni carbonate, citric acid and mixed $SiMo_1W_{11}$ or $SiMo_3W_9$ HPAs and characterized by different techniques. Trimetallic reference $Ni(Mo_n+W_{12-n})/Al_2O_3$ catalysts were prepared by using mixture of two $H_4SiMo_{12}O_{40}$ and $H_4SiMo_{12}O_{40}$ HPAs with the same Mo/W ratio as the references.

HAADF and EXAFS characterizations performed after gas sulfidation have allowed to evidence the formation of mixed $MoWS_2$ slabs for Ni promoted mixed MoW HPAs based catalysts as already observed for the corresponding unpromoted catalysts. The difference states in the more random location of the Mo atoms forming Mo islands surrounding by W atoms, while slabs with large Mo core and shell of W were clearly observed for unpromoted catalysts. Such differences in location seem to be reflected by different Mo-Mo and Mo-W coordination numbers determine for Ni promoted catalysts.

Taking into account results previously obtained in chapter 3 showing that for the unpromoted mixed HPA based catalysts mixed slabs were observed after gas sulfidation as well as after liquid sulfidation, we assume here that mixed slabs could also be formed after liquid sulfidation of Ni promoted corresponding catalysts.

XPS analysis allows to estimate the amount of promoted phase without distinction of NiMoS, NiWS and NiMoWS in the case of trimetallic samples.

For all catalysts the sulfide phase is fully promoted with a Ni substitution rate around 0.8 showing that the mixed phase is as much promoted as the classical NiMoS and NiWS phases.

4.3. Examination of the catalytic properties

4.3.1. Catalytic activity in HDS and HYD reactions

Prior to the catalytic activity evaluation, the catalysts were activated by LP sulfidation. The catalytic activity of sulfided $NiMo_nW_{12-n}/Al_2O_3$ catalysts was examined in HDT of the model feed (1500 ppm S from DBT, 3 wt. % of naphthalene and 1 wt. % of hexadecane in toluene). The HDT activity tests were performed in a fixed-bed microreactor at 280 ºC, 3.0 MPa of hydrogen, with a LHSV of 40 h^{-1} and a 500 NL/L volume ratio of hydrogen to feed. All catalysts exhibited stable performance, achieving a steady state after 7 – 10 h on stream.

The results of the evaluation of the catalytic properties of prepared $NiMo_nW_{12-n}/Al_2O_3$ catalysts in DBT HDS and naphthalene HYD are presented in Table 9. For comparison reason,

the catalytic activities of unpromoted sulfided Mo_nW_{12-n}/Al_2O_3 catalysts tested in the same conditions in HDS of DBT and hydrogenation of naphthalene are presented in Table 9.

Table 9

Catalytic properties of prepared promoted and unpromoted (Ni)(Mo)W/Al_2O_3 catalysts in HDT of a mixture of DBT and naphthalene.[**]

Catalyst	Conversion (%)		Selectivity DBT HDS $S_{HYD/DDS}$	Rate constants $(\times 10^4 \, mol \, h^{-1} \, g^{-1})$	
	DBT HDS	Naphthalene HYD		k_{HDS}	k_{HYD}
$NiMo_{12}/Al_2O_3$	73.0	44.2	0.21	31.8	70.6
NiW_{12}/Al_2O_3	53.6	37.5	0.34	18.7	57.0
$NiMo_1W_{11}/Al_2O_3$	62.1	35.5	0.24	23.4 (19.8)[*]	52.7 (58.1)[*]
$NiMo_3W_9/Al_2O_3$	73.8	39.5	0.23	32.5 (22.0)[*]	60.9 (60.4)[*]
$Ni(Mo_1+W_{11})/Al_2O_3$	54.3	33.9	0.39	19.0 (19.8)[*]	50.0 (58.1)[*]
$Ni(Mo_3+W_9)/Al_2O_3$	45.2	34.0	0.35	14.6 (22.0)[*]	50.2 (60.4)[*]
Mo_{12}/Al_2O_3	16.6	13.5	0.91	0.6	2.2
W_{12}/Al_2O_3	3.0	3.5	0.74	0.1	0.5
Mo_1W_{11}/Al_2O_3	7.2	7.5	1.22	0.2 (0.1)[*]	1.2 (0.7)[*]
Mo_3W_9/Al_2O_3	18.2	18.6	2.76	0.6 (0.2)[*]	3.1 (1.0)[*]
$(Mo_1+W_{11})/Al_2O_3$	5.1	5.3	0.62	0.2 (0.1)[*]	0.8 (0.7)[*]
$(Mo_3+W_9)/Al_2O_3$	6.6	6.1	0.51	0.2 (0.2)[*]	1.0 (1.0)[*]

[*]The additive quantities, which were calculated using the values for $(Ni)Mo_{12}/Al_2O_3$ and $(Ni)W_{12}/Al_2O_3$.
[**]LVSH = 40 h^{-1} for Ni-promoted catalysts and 5h^{-1} for unpromoted ones.

Conversions of the reactants varied from 45.2 to 73.8 % for DBT HDS and from 33.9 to 44.2 % for naphthalene HYD over all prepared catalysts (Table 6). Incorporation of one molybdenum atom into SiW_{12} HPA led to an increase in HDS activity compared to NiW_{12}/Al_2O_3 from 18.7 $\times 10^4$ mol $h^{-1}g^{-1}$ to 23.4 $\times 10^4$ mol $h^{-1}g^{-1}$. Increasing substitution from one to three tungsten atoms resulted in further increase in DBT HDS over $NiMo_3W_9/Al_2O_3$ to 32.5 $\times 10^4$ mol $h^{-1}g^{-1}$ and allowed reaching level of $NiMo_{12}/Al_2O_3$ (31.8 $\times 10^4$ mol $h^{-1}g^{-1}$) catalyst.

In contrast, the Mo content in references prepared from mixture of two HPA had no effect on HDS activity. Thus, $Ni(Mo_1+W_{11})/Al_2O_3$ catalyst had the activity equal to NiW catalysts. $Ni(Mo_3+W_9)/Al_2O_3$ catalyst demonstrated the lowest HDS (rate constant of 14.6×10^4 $mol\,h^{-1}g^{-1}$).

In addition, the rate constant values for trimetallic catalysts were calculated by additive way (Table 9). Trimetallic catalysts prepared by using mixed MoW HPAs had higher values of rate constant than predicted ones. These results support the proposal about formation of mixed NiMoWS sites. Trimetallic references samples, on the contrary, had lower activity, than that was predicted.

$NiMo_{12}/Al_2O_3$ catalysts demonstrated the highest HYD activity (31.8×10^4 $mol\,h^{-1}g^{-1}$) among all studied catalysts. Incorporation of Mo into HPA structure led to slightly decreasing of rate constant from 57.0×10^4 $mol\,h^{-1}g^{-1}$ to 52.7×10^4 $mol\,h^{-1}g^{-1}$ in case of Mo_1W_{11}/Al_2O_3 and increasing until 60.9×10^4 $mol\,h^{-1}g^{-1}$ in case of Mo_3W_9/Al_2O_3.

Both catalysts synthesized from mixture of monometallic HPAs had equal values (50×10^4 $mol\,h^{-1}g^{-1}$) of rate constant which were lower than that obtained for NiW sample.
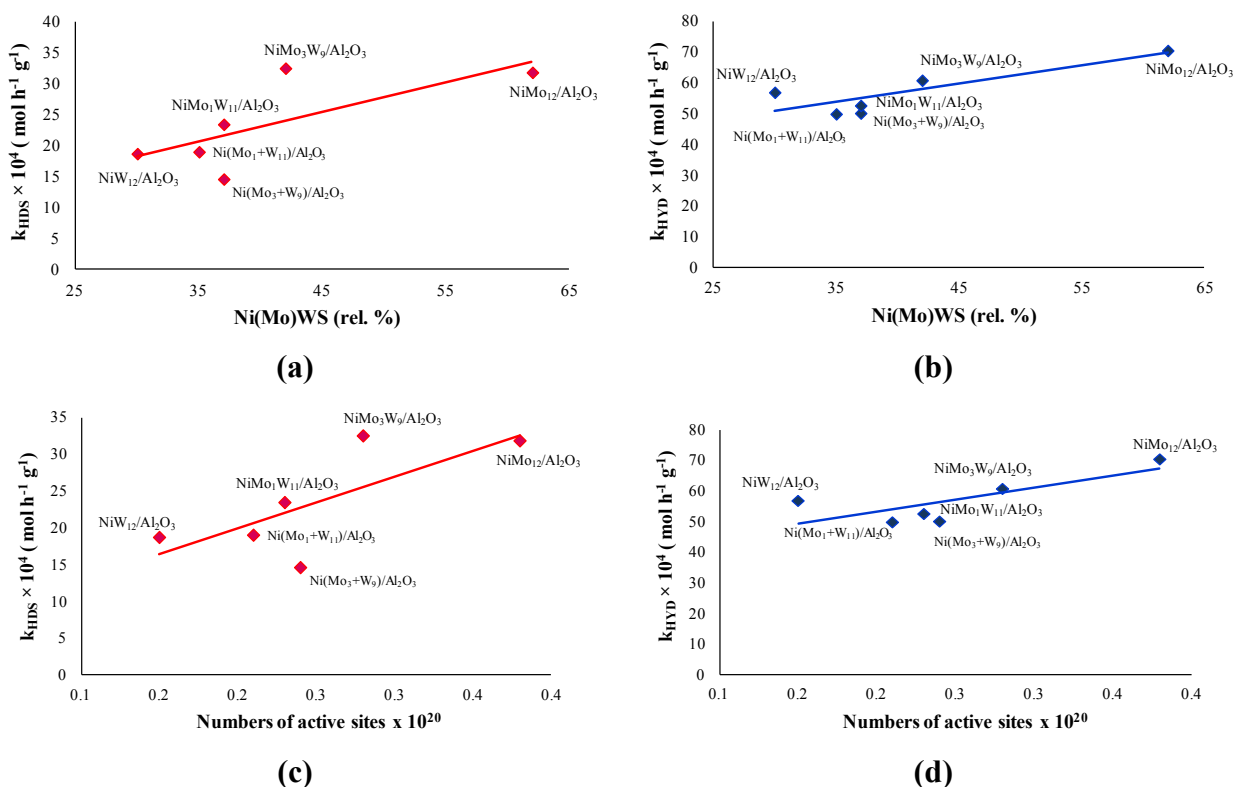

Fig. 5. Dependences of the rate constants of the HDS DBT (a) and HYD naphthalene (b) over Ni(Mo)W/Al$_2$O$_3$ catalysts on the relative % of Ni(Mo)WS phase as determine by XPS decomposition and of the HDS DBT (c) and HYD naphthalene (d) on the number of active promoted sites (T in Table 8).

Fig. 5 demonstrates the dependences of the rate constants of the HDS DBT and HYD naphthalene over Ni(Mo)W/Al$_2$O$_3$ catalysts with the amount of Ni(Mo)WS phase determined by XPS methods (Ni(Mo)WS % and with the number of active promoted sites).

The shape of the curves (a) and (c) and of the curves (b) and (d) are similar showing that parameters as metallic dispersion, slabs average length that have been taken into account to estimate the number of promoted sites follow the same trend in the catalysts series. Linear correlation between HDS rate constants and the amount of Ni promoter atoms into Ni(Mo)WS phase is obtained except for NiMo$_3$W$_9$/Al$_2$O$_3$ and Ni(Mo$_3$+W$_9$)/Al$_2$O$_3$ catalysts. This latter is clearly below the linear trend. The number of relative promoted phase Ni(Mo)WS % together with the number of actives sites is not in agreement with measured catalytic performances for DBT HDS. The low performances are not explained up to now. The NiMo$_3$W$_9$/Al$_2$O$_3$ catalyst offers better catalytic performances than that expected from the estimate number of promoted sites in agreement with the formation of mixed promoted phase developing more active sites for HDS.

A good correlation for naphthalene HYD activity is observed with less variation around the average trend. It means that in this case hydrogenation sites could be different than the HDS sites (relative to DDS pathway) and that hydrogenation activity is directly linked with Ni atoms in promoting sites independently of NiMoS, NiWS and also mixed NiMoWS sites, the activity level of each hydrogenation site being levelled by the presence of Ni.

In order to evaluate and to better understand the Ni-promotion effect, the series of unpromoted catalysts was also tested at the same reaction conditions with liquid sulfidation used for promoted catalysts. The HDT of DBT and naphthalene for (Mo)W/Al$_2$O$_3$ samples was carried out under the following conditions: 280 ℃, 3.0 MPa hydrogen, LHSV − 5 h^{-1} and a 500 NL/L volume ratio of hydrogen to feed. The results of catalytic tests are given in Table 9.

Catalytic results obtained after liquid phase sulfidation and lower temperature reaction (280 instead 320°C) show the same catalytic behavior than already observed after gas phase sulfidation. Bimetallic reference catalysts are largely less efficient than MoW HPAs based catalysts and Mo$_3$W$_9$/Al$_2$O$_3$ presents the best catalytic results for DBT HDS and naphtalene hydrogenation.

When using promoted catalysts an important increase of catalytic performances is noticed for all catalysts. Even if in DBT HDS and in naphthalene hydrogenation, a higher Ni-promotion for catalysts prepared using separate HPAs is observed compared to the solids prepared using mixed HPAs, these latter catalysts still offer better catalytic performances than their corresponding reference. These results witness about some differences in synergy effect between

Ni and mixed sulfide phase mainly present in mixed HPA catalysts confirming the levelling effect of Ni on different active sites (NiMoS, NiWS and NiMoWS) as discussed above. Moreover, cyclic sulfur compounds as DBT react through two pathways: DDS and HYD during HDS reactions. In the unpromoted series, Mo_3W_9/Al_2O_3 is the best catalyst with in particular enhanced hydrogenation properties compared to Mo_{12}/Al_2O_3 catalyst, leading to the highest $S_{HYD/DDS}$ selectivity ratio (2.8 against 0.9 Table 9). Ternary catalysts prepared from two HPAs and SiW_{12}HPA based sample had similar selectivity ratio $S_{HYD/DDS}$ (~ 0.36) compared to mixed and $SiMo_{12}$ HPAs based ones (~ 0.22) in agreement with previously reported results in literature [19,20]. This observation meets the previous one showing that the promoted Ni mixed phase does not possess more active hydrogenation sites than the NiMoS or the NiWS ones for naphthalene hydrogenation.

The activities of the $Ni(Mo)W/Al_2O_3$ catalysts depending on the composition and characteristics of the species of the active phase were estimated by the turnover frequencies (TOF, s^{-1}). Calculated TOF_{HDS} values (Table 10) varied from 3.2×10^3 to 4.3×10^3 s^{-1}, and from 10.8×10^3 to 13.9×10^3 s^{-1} for TOF_{HYD}. The use of mixed MoW HPAs led to increase of the TOF values for DBT HDS compared to other references samples.

Table 10

Calculated *TOF* values of prepared $Ni(Mo)W/Al_2O_3$ catalysts in HDT of model feeds.

Catalyst	*TOF* values($\times 10^3$ s^{-1})				
	DBT+ Naphthalene		DBT+ Naphthalene+ Quinoline		
	TOF_{HDS}	TOF_{HYD}	TOF_{HDS}	TOF_{HYD}	TOF_{HDN}
$NiMo_{12}/Al_2O_3$	3.6	10.8	3.3	0.3	0.2
NiW_{12}/Al_2O_3	4.0	13.9	5.0	3.5	0.6
$NiMo_1W_{11}/Al_2O_3$	4.1 (4.0)[*]	11.8 (13.7)[*]	5.2 (4.8)[*]	4.9 (3.2)[*]	0.8 (0.6)[*]
$NiMo_3W_9/Al_2O_3$	4.3 (3.9)[*]	11.5 (13.1)[*]	4.2 (4.6)[*]	2.0 (2.7)[*]	0.5 (0.5)[*]
$Ni(Mo_1+W_{11})/Al_2O_3$	3.9 (4.0)[*]	12.0 (13.7)[*]	4.9 (4.8)[*]	3.0 (3.2)[*]	1.0 (0.6)[*]
$Ni(Mo_3+W_9)/Al_2O_3$	3.2 (3.9)[*]	12.1 (13.1)[*]	4.2 (4.6)[*]	1.4 (2.7)[*]	0.3 (0.5)[*]

[*]The additive quantities, which were calculated using the values for bimetallic $NiMo_{12}/Al_2O_3$ and NiW_{12}/Al_2O_3.

The 3D dependence of the *TOF* number in DBT HDS and naphthalene HYD over NiMo$_n$W$_{12-n}$/Al$_2$O$_3$ catalysts on the average length of the Ni(Mo)WS phase species and (Ni/Mo+W)$_{edge}$ ratio is shown in Fig. 6. The use of mixed HPAs as starting precursors allowed to achieve the highest *TOF*$_{HDS}$ values at lower promotion degree and a long particle length compared to NiMo$_{12}$/Al$_2$O$_3$ (Fig. 6). In addition, the *TOF* values for trimetallic catalysts were calculated by additive way (Table 10). Both samples prepared by using MoW HPAs had active sites with higher *TOF* values than predicted values. Thus, the high *TOF*$_{HDS}$ number of active sites in these catalysts can be attributed to the formation of mixed NiMoWS active sites. The lowest *TOF* number of Ni(Mo)WS sites in DBT HDS was achieved in Ni(Mo$_3$+W$_9$)/Al$_2$O$_3$ catalyst.
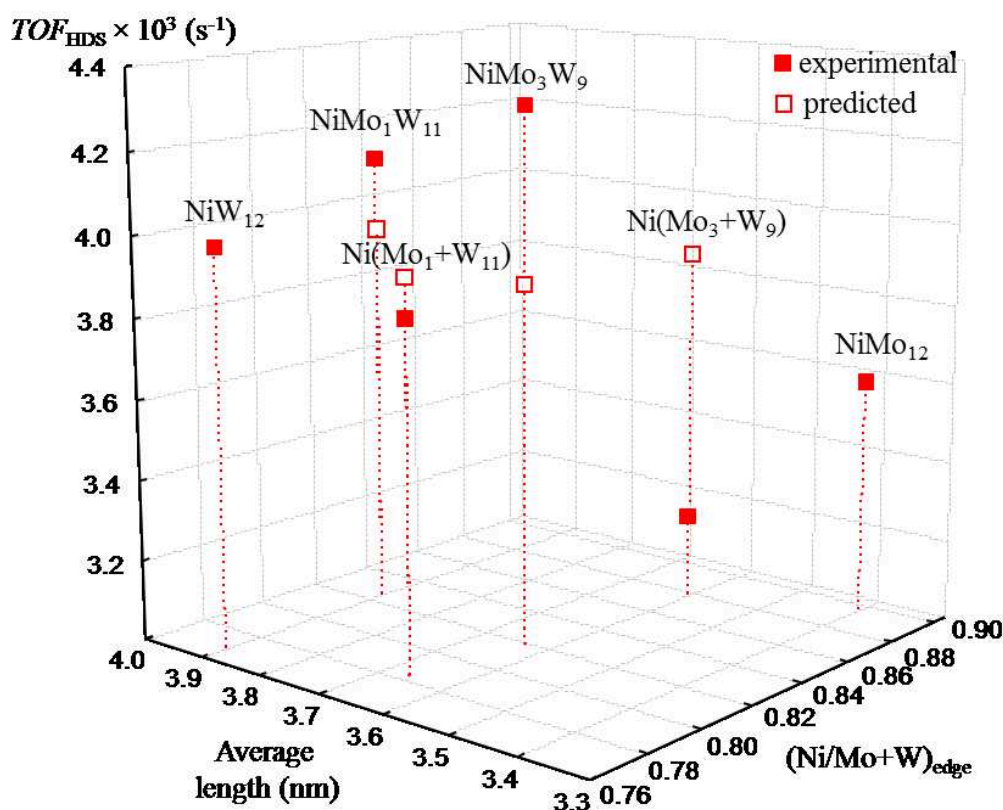
Fig. 6. 3D dependence of the *TOF* number in DBT HDS over Ni(Mo)W/Al$_2$O$_3$ catalysts on the average length of the Ni(Mo)WS phase species and (Ni/Mo+W)$_{edge}$ ratio.

4.3.2. Catalytic activity in HDS, HYD and HDN reactions

Catalytic properties of synthesized catalysts were also investigated in co-hydrotreating of DBT, naphthalene, and quinoline. The HDT activity tests were performed in a fixed-bed microreactor at 280 ºC, 3.0 MPa of hydrogen, with a LHSV of 40 h^{-1} and a 500 NL/L volume ratio of hydrogen to feed. A mixture of DBT (1500 ppm S), naphthalene (3 wt.%), quinoline

(500 ppm N), hexadecane (as an internal standard, 1 wt.%) and toluene (as a solvent) was used as a model feedstock for evaluation of HDS, HYD and HDN performances.Prior to the catalytic activity evaluation, the catalysts were activated by LP sulfidation.

The inhibitory effect of quinoline on the hydrogenating function of the catalysts is attributed to a negative influence of N-containing products of quinoline HYD and ammonia evolving during quinoline HDN. Strong adsorption of quinoline and its HYD products hinders the adsorption of naphthalene molecules on the active sites of the catalyst and thus slows down the rate of hydrogenation of organic compounds [21-23]. It was found that the selectivity of DBT HDS change in the presence of quinoline in the feedstock.

Table 11 shows the results of hydrotreating of a mixture containing DBT, naphthalene and quinoline over $NiMo_nW_{12-n}/Al_2O_3$ catalysts. The conversion of all substrates in the course of the tests varied from 1.2 to 78%.

Table 11

Catalytic properties of prepared $Ni(Mo)W/Al_2O_3$ catalysts in HDT of a mixture of DBT, naphthalene and quinoline.

Catalyst	Conversion (%)			Selectivity ratio $S_{HYD/DDS}$ DBT HDS	Rate constants $(\times 10^4 \, mol \, h^{-1} \, g^{-1})$		
	DBT HDS	Naphthalene HYD	Quinoline HDN		k_{HDS}	k_{HYD}	k_{HDN}
$NiMo_{12}/Al_2O_3$	67.9	1.2	5.6	0.01	27.6	1.5	1.1
NiW_{12}/Al_2O_3	66.8	9.3	10.3	0	26.8	11.9	2.0
$NiMo_1W_{11}/Al_2O_3$	78.0	14.7	16.7	0.01	36.6 (26.9)[*]	19.2 (11.0)[*]	3.4 (1.9)[*]
$NiMo_3W_9/Al_2O_3$	72.5	7.0	10.5	0	31.3 (27.0)[*]	8.8 (9.3)[*]	2.1 (1.8)[*]
$Ni(Mo_1+W_{11})/Al_2O_3$	69.3	8.4	18.9	0.01	28.6 (26.9)[*]	10.6 (11.0)[*]	3.9 (1.9)[*]
$Ni(Mo_3+W_9/Al_2O_3)$	59.5	4.0	6.1	0.01	21.9 (27.0)[*]	4.9 (9.3)[*]	1.2 (1.8)[*]

[*]The additive quantities, which were calculated using the values for bimetallic $NiMo_{12}/Al_2O_3$ and NiW_{12}/Al_2O_3.

The detailed analysis of the reaction products shows that for all the studied catalysts the preferential pathway is DDS, in case of quinoline containing model feed. The HDS product from

DBT included only biphenyl (BP) via the DDS pathway (Chapter 1 Scheme 1). Absence of hydrogenated tetrahydro- and perhydrodibenzothiophenes, as well as cyclohexylbenzene (CHB) and bicyclohexyl (BCH) via the HYD pathway of DBT HDS was caused by strong inhibition effect of quinoline present in the feed. Tetralin was the main product of naphthalene HYD reaction (Chapter 1 Scheme 3).The presence of decaline in reaction products has not been detected over all catalysts under chosen conditions. Since 92–98% quinoline rapidly turns into tetrahydroquinoline (Chapter 1 Scheme 4), conversion of nitrogen-containing compounds (x_N) was calculated as follows:

$$x_N = \frac{C_H}{C_H + C_N + C_{Qui}} \times 100\%, \qquad (3)$$

where C_H is concentration (wt.%) of HDN products not containing nitrogen (propylbenzene (PB), propylcyclohexane (PCH)); C_N is concentration (wt.%) of HDN products containing nitrogen (tetrahydroquinoline (THQui), o-aminopropylbenzene (o-APB), o-aminopropylcyclohexane (o-APCH)); C_{Qui} concentration (wt.%) of quinoline after reaction.

Rate constants values depending on the reaction type increased in the order HDN < HYD < HDS that correlated with the reactivity of the chosen compounds (Table 11). NiW based hydrotreating catalysts are usually more efficient than NiMo ones for HYD and HDN reactions especially at severe conditions. [21,24-26]. As expected, the lowest value of rate constant in HYD reaction was obtained over NiMo$_{12}$/Al$_2$O$_3$ catalysts. Addition of one Mo to SiW$_{12}$ HPA led to increase of k_{HDS} from 26.8×10^4 mol h^{-1} g^{-1} to 36.6×10^4 mol h^{-1} g^{-1}, k_{HYD} from 11.9×10^4 mol h^{-1} g^{-1} to 19.2×10^4 mol h^{-1} g^{-1} and k_{HDN} from 2.0×10^4 mol h^{-1} g^{-1} to 3.4×10^4 mol h^{-1} g^{-1}. Increasing of molybdenum content in mixed HPA resulted in the increase of HDS to 31.3×10^4 mol h^{-1} g^{-1}. At the same time NiMo$_3$W$_9$/Al$_2$O$_3$ had the demonstrated the same HDN performance and slightly lower HYD activity compared to NiW$_{12}$/Al$_2$O$_3$.

Both ternary mixed HPAs based catalysts had higher HDS catalytic activity than their analogues with the same Mo/W ratio. Moreover, these catalysts were at 1.8 times more active in the hydrogenation of naphthalene than ternary references. However, Ni(Mo$_1$+W$_{11}$)/Al$_2$O$_3$ had higher HDS activity, than that obtained on NiW catalyst and close value of $k_{HYD}=10.6 \times 10^4$ mol h^{-1} g^{-1}. In addition, both catalysts with molar ratio Mo/W=1/11 had the equal rate constants of quinoline HDN. The value of DBT conversion was the lowest on (Mo$_3$+W$_9$)/Al$_2$O$_3$ catalyst and its HYD and HDN activities were significantly lower than those obtained for other W-containing catalysts.

It should be mentioned that in the case of quinoline containing model feed $NiMo_1W_{11}/Al_2O_3$ sample demonstrated higher rate constants in all studied reactions than $NiMo_3W_9/Al_2O_3$ in contrast with unpromoted and Ni promoted catalysts in HDT of free quinoline feedstock. In addition, experiment values of rate constants and TOF values for the HDS of DBT, HYD of naphthalene and HDN of quinoline on $NiMo_1W_{11}/Al_2O_3$ catalyst were higher than those calculated by the additive way (Table 11).

The main product of DBT HDS in presence of quinoline was biphenyl via the DDS pathway, as noted previously, while HYD pathway had been preferable for model feed without quinoline (Table 9). Presence of quinoline, in addition to change of pathway of HDS reaction led to a higher HDS conversion over tungsten-containing catalysts (Table 11, Fig.7.).
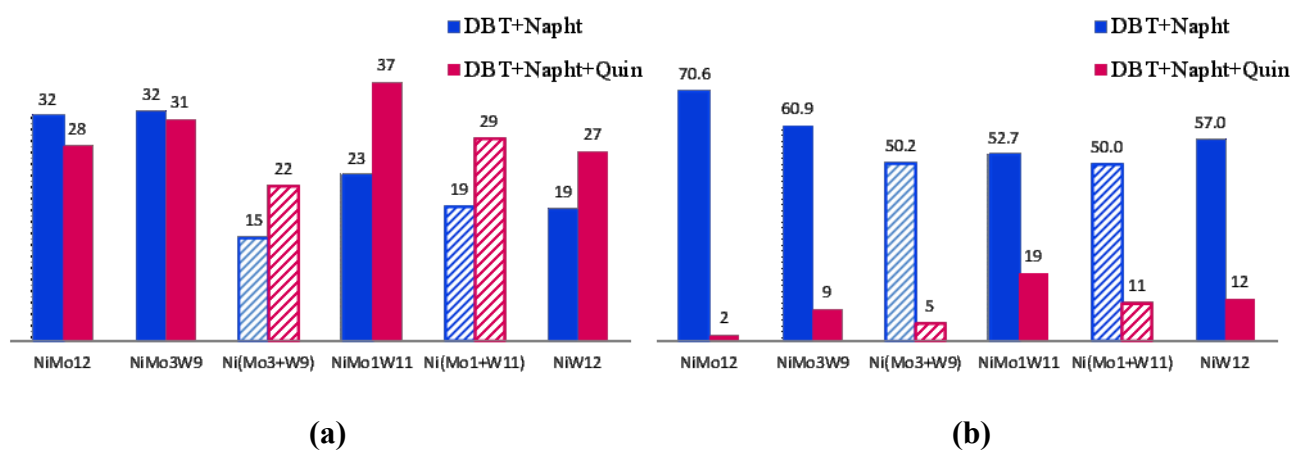

(a) **(b)**

Fig. 7. Rate constants of DBT HDS (a) and naphthalene HYD (b) without quinoline and in the presence of quinoline on the $NiMo_nW_{12-n}/Al_2O_3$ catalysts.

Promotion effect of nitrogen compounds on hydrogenolysis of DBT was previously described in the literature [27-29]. It is known that quinoline rapidly turns into tetrahydroquinoline which is adsorbed on one catalytic site perpendicular to the catalyst surface due to lack of π-electrons in the ring with the nitrogen atom. Moreover, the adsorption of THQui is 3 times higher than that of quinoline [30]. Therefore, after THQui adsorption only one neighboring active site remains vacant and available for σ-adsorption of DBT molecule for HDS via DDS pathway. Thus, the number of DDS sites increases owing to the conversion of HYD sites into active DDS sites induced by the adsorption of saturated products of quinoline HYD on the active phase. A similar slow-down of the rates of the HYD pathway of DBT HDS and naphthalene HYD in the presence of quinoline suggests that DBT HYD and naphthalene HYD occur on the same active sites. On the opposite, rate constants of the DDS of DBT do not depend

on the rate constants of naphthalene HYD. It confirms that DDS and HYD occur on different active sites.

The inhibitory effect of quinoline on the DBT HDS reaction rate was estimated by the inhibitory factor value, which was calculated as follows:

$$\theta_{HDS}^{DBT} = \frac{k_{HDS}^{DBT} - k_{HDS}^{DBT'}}{k_{HDS}^{DBT}},\qquad(4)$$

where θ_{HDS}^{DBT} is the inhibitory factor of quinoline on DBT HDS (%); k_{HDS}^{DBT} is the rate constant

of the DBT HDS reaction without quinoline ($\times 10^4$ mol h^{-1}g^{-1}); and $k_{HDS}^{DBT'}$ is the rate constant of the DBT HDS reaction in the presence of quinoline ($\times 10^4$ mol h^{-1}g^{-1}).

The quinoline inhibitory factor on naphthalene HYD was calculated by the following equation:

$$\theta_{HYD}^{Napht} = \frac{k_{HYD}^{Napht} - k_{HYD}^{Napht'}}{k_{HYD}^{Napht}},\qquad(5)$$

where θ_{HYD}^{Napht} is the quinoline inhibitory factor on naphthalene HYD (%); k_{HYD}^{Napht} is the rate

constant of naphthalene HYD without quinoline ($\times 10^4$ mol h^{-1}g^{-1}); and $k_{HYD}^{Napht'}$ is the rate constant of naphthalene HYD inthe presence of quinoline ($\times 10^4$ mol h^{-1}g^{-1}).

The most significant promoting effect on the rate of biphenyl formation in DBT HDS was observed for both ternary samples prepared from the mixture of two HPAs (θ_{HDS}^{DBT} is -50.7%) and SiMo$_1$W$_{11}$ HPA based one (θ_{HDS}^{DBT} is -56.2%), the rate constant increased by 1.5 times on the average for these catalysts (Fig. 9).Whereas the NiMo$_3$W$_9$/Al$_2$O$_3$ catalysts with the highest HDS activity in HDT of DBT+Napth model feed kept its activity when quinoline was added. NiW$_{12}$/Al$_2$O$_3$, as expected, was stronger promoted by of quinoline than NiMo$_{12}$/Al$_2$O$_3$ catalysts. However, HYD pathway of HDS DBT was almost completely poisoned when the addition of quinoline for all studied catalysts.
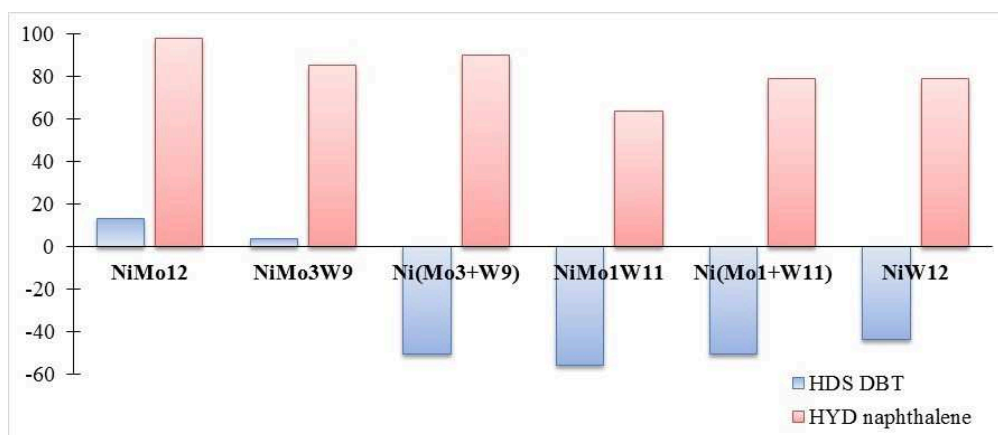
Fig. 9. Dependence the inhibitory factor value of quinoline on the DBT HDS (in blue) and naphthalene HYD (in red) on catalyst's composition.

Naphthalene HYD was inhibited as well HYD pathway of HDS DBT due to competitive adsorption of the reagents. The catalytic activity of trimetallic samples in naphthalene HYD decreased with loading of Mo. $NiMo_1W_{11}/Al_2O_3$ catalyst is more resistant to inhibition of quinoline than its counterparts $Ni(Mo_1+W_{11})/Al_2O_3$. Moreover, $NiMo_1W_{11}/Al_2O_3$ had the highest conversion of naphthalene and DBT among all studied catalysts.

Dependences of the rate constants of the HDS DBT (a); HYD naphthalene (b) and HDN quinoline over $Ni(Mo)W/Al_2O_3$ catalysts on the number of active promoted sites have been plotted in Fig. 10
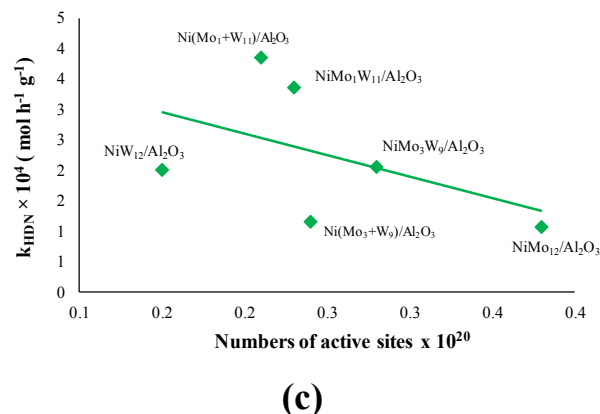

(a)

(b)

(c)
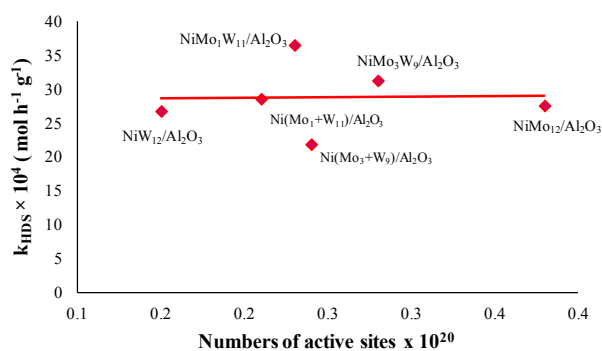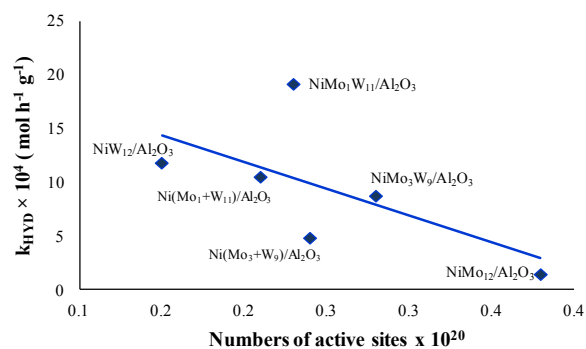
Fig. 10. Dependences of the rate constants of the HDS DBT (a); HYD naphthalene (b) and HDN quinoline (c) over Ni(Mo)W/Al$_2$O$_3$ catalysts on the number of active promoted sites (T in Table 8).

The trends for HDS DBT and naphthalene hydrogenation differ from that previously observed without quinoline. Indeed, no evolution of the HDS rate constant can be noticed with the number of promoted sites while a decrease is observed for k_{HYD}. Moreover the trends observed for naphthalene hydrogenation and quinoline HDN are similar which can be assigned to required pre-hydrogenation before C-N hydrogenolysis. Inhibition effects could be at the origin of this different behavior. Nevertheless in the series, the NiMo$_1$W$_{11}$/Al$_2$O$_3$ catalyst shows better rate constants in HDS hydrogenation and HDN confirming the advantage to use mixed HPA as precursors for HDT reactions. We propose that this global improvement could be related to the formation of the mixed promoted phase with different catalytic properties.

Conclusions

MoW catalysts promoted by Ni were characterized after sulfidation by EXAFS and HAADF (gas sulfidation) and TEM and XPS (liquid phase sulfidation) The promotion by Ni do not prevent the formation of mixed MoWS sulfide phase in mixed HPA based catalysts. HAADF images show that these mixed slabs are formed with Mo islands surrounded by W atoms in agreement with EXAFS fittings. XPS analysis allows to estimate the amount of promoted phase without distinction of NiMoS, NiWS and NiMoWS in the case of trimetallic samples. It was found that NiMoW catalysts prepared by using different precursors demonstrated a difference in sulfidation degree of metals. Combination of TEM results and atomic composition determined by XPS enabled, using the hexagonal model of disulphide slabs, to calculate the nickel substitution rate. For all catalysts the sulfide phase is fully promoted with a Ni substitution rate around 0.8 showing that the mixed phase is as much promoted as the classical NiMoS and NiWS phases.

The sulfided NiMoW catalysts were tested in the hydrotreating of a mixture of DBT and naphthalene in presence of quinoline and without quinoline. For Mo_3W_9 catalysts evaluated in DBT HDS without quinoline, improved catalytic performance has been attributed to the presence of more active mixed NiMoWS sites. For hydrogenation of naphthalene without quinoline, activity depends only on the number of active sites without distinction between mixed and monometallic promoted sites. With quinoline, inhibition effects on hydrogenation reactions are observed favoring largely the DDS pathway in the case of DBT HDS. Different trends are observed when plotting DBT HDS and naphthalene hydrogenation rate constants versus the number of active sites. Indeed, no evolution of the HDS rate constant can be noticed with the number of promoted sites while a decrease is observed for k_{HYD}. Moreover, the trends observed for naphthalene hydrogenation and quinoline HDN are similar, which can be assigned to pre-hydrogenation reaction before C-N hydrogenolysis. In the hydrotreatment of a mixture of DBT and naphthalene, the most efficient HDS active sites are observed in Mo_3W_9 catalyst prepared from mixed HPA. In the presence of quinoline the Mo_1W_{11} catalyst shows better performances in HDS, hydrogenation and HDN confirming the advantage to use mixed HPA as precursors for HDT reactions. This global improvement should be related to the formation of the mixed promoted phase evidenced by HAADF and EXAFS refinements.

References

1   A. Griboval, P. Blanchard, E. Payen, M. Fournier, J.L. Dubois. Alumina supported HDS catalysts prepared by impregnation with new heteropolycompounds. Comparison with catalysts prepared by conventional Co–Mo–P coimpregnation // *Catalysis Today.* –1998. – V.45 –P.277.

2   M. Breysse, C. Geantet, P. Afanasiev, J. Blanchard, M. Vrinat. Recent studies on the preparation, activation and design of active phases and supports of hydrotreating catalysts // *Catalysis Today*. –2008. –V.130 –P.3-13

3   P. Nikulshin, A. Mozhaev, C. Lancelot, P. Blanchard, E. Payen, C. Lamonier. Hydroprocessing catalysts based on transition metal sulfides prepared from Anderson and dimeric Co_2Mo_{10}-heteropolyanions. A reviewCatalyseurs d'hydrotraitement à base de sulfures de métaux de transition préparés à partir des hétéropolyanions d'Anderson et du dimère Co_2Mo_{10}. Une revue // *Comptes Rendus Chimie*. –2016. –V.19. –P.1276.

4   S.D. Kelly. N. Yang. G.E. Mickelson, N. Greenlay. E. Karapetrova. W. Sinkler, Simon R.Bareb. Structural characterization of Ni–W hydrocracking catalysts using in situ EXAFS and HRTEM // *Journal of Catalysis*. –2009. –V.263 –P. 16–33

5   L. Lizama, T. Klimova. Highly active deep HDS catalysts prepared using Mo and W heteropolyacids supported on SBA-15 // *Applied Catalysis B: Environmental*. –2008. –V.82 –P.139–150

6   N. Frizi, P. Blanchard, E. Payen, P. Baranek, M. Rebeilleau, C. Dupuy, J. P. Dath. Genesis of new HDS catalysts through a careful control of the sulfidation of both Co and Mo atoms: Study of their activation under gas phase // *Catalysis Today.* –2008. –V.130. –P.272–282

7   P. P. Minaev, P. A. Nikulshin, M. S. Kulikova, A. A. Pimerzin, V. M. Kogan. $NiWS/Al_2O_3$ hydrotreating catalysts prepared with 12-tungstophosphoric heteropolyacid and nickel citrate: Effect of Ni/W ratio// *Applied Catalysis A: General*. –2015. –V.505. –P.456–466

8   D. Ishutenko, P. Minaev, Yu. Anashkin, M. Nikulshina, A. Mozhaev, K. Maslakov, P. Nikulshin. Potassium effect in $K-Ni(Co)PW/Al_2O_3$ catalysts for selective hydrotreating of model FCC gasoline // *Applied Catalysis B: Environmental*. –2017. –V.203 –P.237–246.

9   J.C. Mogica-Betancourt, A. Lopez-Benitez, J.R. Montiel-Lopez, L. Massin, M. Aouine, M. Vrinat, G. Berhault, A. Guevara-Lara. Interaction effects of nickel polyoxotungstate with the Al_2O_3–MgO support for application in dibenzothiophene hydrodesulfurization // *Journal of Catalysis*. –2014. –V.313 –P.9–23

10   K.B. Tayeb, C. Lamonier, C. Lancelot, M. Fournier, E. Payen, A. Bonduelle, F.Bertoncini. Study of the active phase of NiW hydrocracking sulfided catalysts obtained from an innovative heteropolyanion based preparation // *Catalysis Today*. –2010. –V.150. –P.207–212.

11   K.B. Tayeb, C. Lamonier, C. Lancelot, M. Fournier, A. Bonduelle-Skrzypczak, F. Bertoncini. Increase of the Ni/W Ratio in Heteropolyanions Based NiW Hydrocracking Catalysts with Improved Catalytic Performances // *Catalysis Letters*. –2014. –V.144. –P.460–468.

12   D. Zuo, M. Vrinat, H. Nie, F. Mauge, Y. Shi, M. Lacroix, D. Li. The formation of the active phases in sulfided NiW/Al$_2$O$_3$ catalysts and their evolution during post-reduction treatment // *Catalysis Today*. –2004. –V.93. –P.751–760.

13   L. Coulier, G. Kishan, J.A.R. van Veen, J. Niemantsverdriet. Influence of Support-Interaction on the Sulfidation Behavior and Hydrodesulfurization Activity of Al2O3-Supported W, CoW, and NiW Model Catalysts // *Journal of Physical Chemistry B*. –2002. –V.106. –P.5897–5906.

14   B. Scheffer, P. J. Mangnus, J. A. Moulijn. A temperature-programmed sulfiding study of NiO 3/Al2O3 catalysts // *Journal of Catalysis*. –1990. –V.121 –P.18.

15   C.-H. Kim, W. Yoon. I. Lee, S. Woo. The effect of Ni loading and the sulfidation temperature on the structure and catalytic activity of Ni-W hydrodesulfurization catalysts // *Applied Catalysis A: General*. –1996. –V.144 –P.159-175.

16   A. Cordova, P. Blanchard, C. Lancelot, G. Frémy, C. Lamonier. Probing the Nature of the Active Phase of Molybdenum-Supported Catalysts for the Direct Synthesis of Methylmercaptan from Syngas and H$_2$S // ACS Catalysis. –2015. –V.5 (5), –P.2966.

17   S. Kasztelan, H. Toulhoat, J. Grimblot, J. P. Bonnelle. A geometrical model of the active phase of hydrotreating catalysts. // *Applied Catalysis*. –1984. –V.13. –P.127–159

18   E. Krebs, B. Silvi, P. Raybaud. Mixed sites and promoter segregation: A DFT study of the manifestation of Le Chatelier's principle for the Co(Ni)MoS active phase in reaction conditions // *Catalysis Today*. –2007. –V.130 –P.160

19   P. Raybaud, H. Toulhoat // Catalysis by Transition Metal Sulphides From Molecular Theory to Industrial Application. –2013.

20   F. Bataille, J.-L. Lemberton, P. Michaud, G. Pérot, M. Vrinat, M. Lemaire, E. Schulz, M. Breysse, S. Kasztelank. Alkyldibenzothiophenes Hydrodesulfurization-Promoter Effect,

Reactivity, and Reaction Mechanism // *Journal of Catalysis.* –2000. –V.191. –P.409–422

21   A. Stanislaus, A. Marafi, and M. S. Rana. Recent advances in the science and technology of ultra low sulfur diesel (ULSD) production // *Catalysis Today*. –2010. –V.153. –P.1-68

22   T. C. Ho and L. Qiao. Competitive adsorption of nitrogen species in HDS: Kinetic characterization of hydrogenation and hydrogenolysis sites // *Journal of Catalysis*. –2010. –V.269. –P.291

23   M. Egorova and R. Prins. Mutual influence of the HDS of dibenzothiophene and HDN of 2-methylpyridine // *Journal of Catalysis*. –2004. –V.221. –P.11.

24   W.R.A.M. Robinson, J.A.R. van Veen, V.H.J. de Beer, R.A. Santen. Development of deep hydrodesulfurization catalysts: II. NiW, Pt and Pd catalysts tested with (substituted) dibenzothiophene // *Fuel Processing Technology*. –1999. –V.61. –P.103–116.

25   S.A. Ali, M.A.B. Siddiqi. Dearomatization, cetane improvement and deep desulfurization of diesel feedstock in a single-stage reactor // *Reaction Kinetics and Catalysis Letters*. –1997. –V.61. –P.363–368.

26   H. Topsøe, B.S. Clausen, F.E. Massoth. Hydrotreating catalysis // *Catalysis–Science and Technology*. –1996. –V.11. –P..310.

27   V. LaVopa, and C. N. Satterfield. Response of dibenzothiophene hydrodesulfurization to presence of nitrogen compounds // *Chemical Engineering Communications*. –1998. –V.70 –P.171 (1988).

28   R. Prins. Catalytic hydrodenitrogenation // *Advances In Catalysis*. –2001. –V.46 –P.399-464.

29   V.A. Sal'nikov, P.A. Nikul'shin, A.A. Pimerzin. The catalytic properties of transition metal sulfides synthesized from Anderson-type heteropoly compounds in hydrogenation, hydrodesulfurization, and hydrodenitrogenation reactions // *Petroleum Chemistry.* –2013. –V.53. –P.233–244.

30   Beltramore A.R., Crossley S., Resasco D.E., AlvarezW.E., Choudhary T.V. Inhibition of the Hydrogenation and Hydrodesulfurization Reactions by Nitrogen Compounds over NiMo/Al$_2$O$_3$ // *Catalysis Letters*. –2008. –V.123. –P.181.

General Conclusion

General Conclusion

It is a world-wide tendency that more stringent environmental regulations require the production of higher quality fuels with lower sulfur concentration. It is a challenge to develop more active hydrodesulfurization (HDS) catalysts for the «deep refining» of feedstocks to meet the new strict standards. Especially, sulfides catalysts described as γ-alumina supported CoMoS, NiMoS or NiWS active phase are widely used in hydrotreatment processes depending on the requested catalytic properties (hydrodesulfurization, hydrogenation or hydrodenitrogenation). The active phase of the traditional catalysts consists in MoS_2 or WS_2 nanocrystallites promoted by Co or Ni atoms located at the edges of the sulfide slabs. These catalysts exhibit high activity in removing sulfur from thiophene and benzothiophene compounds and some non-refractory dibenzothiophenes (DBT). However, their activity is very low in removing sulfur from specific alkyl substituted derivatives as the 4,6 DMDBT. Moreover the presence of aromatics or nitrogen compounds in the feed as expected in low quality petroleum feedstock's can decrease catalysts efficiency.

The development of catalysts based on mixed transition metal sulfides can become a possible solution to the problem of creating more efficient production processes. A leap to a new level of activity of hydrotreating (HDT) catalysts was carried out in the early 2000 with the advent of the «Nebula» catalyst. This new bulk NiMoW catalyst with improved catalytic performances has at least three times greater activity than classical HDT catalysts. Beneficial effect could be attributed to the trimetallic character and the formation of NiMoWS active phase rather than the conventional bimetallic NiWS, NiMoS and CoMoS counterparts and high content of metals as well because this catalyst does not contain a support. However, this advantage is at the same time its main drawback of the catalyst due to its high cost. One possible solution is to develop supported trimetallic sulfide catalyst.

The aim of the study was the preparation of alumina supported bi- and trimetallic (Ni)MoW catalysts starting from mixed $SiMo_nW_{12-n}$ Keggin type heteropolyacids (HPAs). This approach has never been reported in the literature and could benefit from the initial proximity of Mo and W at the nanoscale to induce mixed $(MoW)S_2$ phase formation. For comparison purposes, catalysts based on separate $SiMo_{12}$ HPA and SiW_{12} HPA and their mixture were also prepared and studied.

Two heteropolyacids of α-$H_4[SiMo_1W_{11}O_{40}]$ and β-$H_4[SiMo_3W_9O_{40}]$ were prepared and characterized by IR-, Raman and polarography techniques. The combination of XRD and EXAFS results allowed to confirm the elemental composition and the structure of prepared mixed HPAs.

A series of unpromoted $Mo(W)S_2/Al_2O_3$ catalysts with the same surface density of metals ((Mo+W) = 4 at/nm^2) were synthesized by the incipient wetness method via impregnation of alumina with aqueous solutions containing the required amounts of HPAs. After drying EXAFS analysis have allowed to conclude to the preservation of mixed HPA on alumina surface while $AlMo_6O_{24}H_6^{3-}$ Aderson HPA was identified by Raman analysis for the catalyst prepared from $SiMo_{12}$ HPA.

Dried samples were directly activated by gas phase (H_2S/H_2) (GP) and liquid phase (DMDS) (LP) sulfidation.

The physical-chemical properties and catalytic activity are demonstrated to be correlated to the nature of the initial precursors. The use of mixed HPAs resulted in small reduction of average length of active phase species compared to mixture of separate HPAs. In Mo_3W_9/Al_2O_3 catalyst XPS analysis shows similar Mo sulfidation degree (around 82 rel.%) compared to Mo_{12}/Al_2O_3 catalyst while tungsten sulfidation degree were largely higher and similar in both bimetallic samples (~ 64 rel.%) compared to that of monometallic W_{12}/Al_2O_3 reference (49 rel.%), regardless of sulfidation type. LP activation of bimetallic samples was leading to complete Mo sulfidation.

Sulfided Mo_3W_9/Al_2O_3 and $(Mo_3+W_9)/Al_2O_3$ catalysts were characterized by HAADF. It was found that GP sulfidation of mixed molecular precursor led to formation of a core−shell structure, where Mo was mostly located in the core and W in the shell. In contrast, $(Mo_3+W_9)/Al_2O_3$ catalyst prepared from two HPAs show a large majority of monometallic MoS_2 and WS_2 slabs with only few bimetallic particles. Results of HAADF characterization are in good agreement with those were obtained by EXAFS. The best fitting results of EXAFS spectra for the catalysts prepared from separate HPAs showed that second coordination shell consists only one metal-metal contributions, while mixed HPAs based catalysts showed the presence of heteroatom neighbors (Mo versus W) in second coordination shell, indicating the formation of mixed $Mo_nW_{12-n}S_2$ active phase. The active phase of LP sulfided Mo_3W_9/Al_2O_3 consists in isolated Mo islands randomly distributed inside the WS_2 slabs. LP sulfidation of $(Mo_3+W_9)/Al_2O_3$ led to the main formation of monometallic particles and few mixed ones where Mo atoms appear to be gathered in larger islands surrounding by W atoms.

Genesis of the active phase was studied during in-situ sulfidation by H_2S/H_2 of the catalysts by Quick-XAS. The chemometric methods, such as PCA and MCR-ALS methods, allowed to determine number of intermediate species and their concentration profiles. It was found that tungsten sulfidation using mixed HPA precursor started at lower temperature,

compared to W sulfidation in monometallic and bimetallic references catalysts. This Mo and W simultaneously sulfidation t can govern the formation of mixed $MoWS_2$ phase.

The catalytic activity of the synthesized catalysts was evaluated in HDT of model feed containing DBT and naphthalene. Substitution of one or three tungsten atoms by molybdenum ones in case of mixed HPAs resulted to in a significant increase of DBT HDS as well as naphthalene HYD activity, compared to those obtained for catalysts prepared from mixture of HPAs. Furthermore, HDS activity over Mo_3W_9/Al_2O_3 was equal to that obtained on Mo_{12}/Al_2O_3, while HYD activity was higher. The trend in distribution of the catalytic properties was kept whatever the activation type. In addition, the mixed HPAs based catalyst also presented high DBT HDS selectivity ratio $S_{HYD/DDS}$, being usually typical of bulk sulfides having significant HYD activity. This observation supports the formation of different active sites at the edges of the $MoWS_2$ phase developing strong hydrogenation properties required for the treatment of heavy fuels. In order to understand the better efficiency of the edge site of $MoWS_2$ mixed phase DFT calculations are in progress for evidencing a prospective electronic effect.

The same Ni-promoted series with a surface density of metals $((Mo+W) = 4.2$ at/nm$^2)$ was also prepared. GP sulfidation of $NiMo_3W_9/Al_2O_3$ resulted again, in the presence of Ni, in the formation of mixed slabs where small molybdenum islands are surrounded by WS_2 as .imaged by HAADF. In contract, the active phase of $Ni(Mo_3+W_9)/Al_2O_3$ sulfided under gas phase consisted mainly of monometallic slabs. This different locations of Mo and W atoms in sulfide slabs was also reflected by EXAFS refinements. As in case of unpromoted catalysts, mixed HPAs based catalysts had two metal-metal contributions in the second coordination shell thus indicating of the mixed active phase formation. The samples prepared from separate HPAs had only homogeneous metal-metal contributions in the second shell.

Based on previous HAADF characterizations performed on unpromoted seris, the formation of mixed MoW sulfide phase after LP sulfidation was assumed in the Ni promoted mixed HPA based catalysts. LP sulfided catalysts were tested in hydrotreating of a mixture DBT and naphthalene. It was established that incorporation of Mo atoms into the SiW_{11} and SiW_9 heteropolyanions led to an increase of the HDS rate constant in comparison with NiW_{12}/Al_2O_3, while addition of Mo in bimetallic references catalysts had no effect. The catalytic synergy of mixed HPAs based catalysts was attributed to the presence of mixed $(Ni)Mo_nW_{12-n}S_2$ giving rise to the most efficient NiMoWS sites. HDS activity level of $NiMo_3W_9/Al_2O_3$ sample was corresponded to the $NiMo_{12}/Al_2O_3$ despite a greater amont of actives sites in this latter catalyst.

In addition, the catalytic properties Ni-promoted catalysts were evaluated in co-hydrotreating of DBT, naphthalene and quinoline. Introduction of Mo into the structure of HPA

led to significant increase on HDS activity. Mixed HPAs based catalysts were more resistant to inhibition by quinoline. Both catalysts synthesized from MoW HPAs had the highest values of rate constant compared to bimetallic as well corresponding trimetallic counterparts in all studied reactions. In the presence of quinoline the Mo_1W_{11}/Al_2O_3 catalyst containing a mixed promoted phase shows better performances in HDS, hydrogenation and HDN confirming the advantage to use mixed HPA as precursors for HDT reactions.

In summary, in the framework of this PhD thesis an innovative way to prepare (Ni)MoW catalysts was presented in which mixed MoW HPAs were used as Mo and W precursor. It had been established that the proximity of atoms in starting material results to synergetic effect between them after sulfidation through the formation of mixed $MoWS_2$ slabs. For the first time, the combination of advanced characterization techniques, EXAFS and HAADF, allowed to investigate the nanoscale location of Mo and W in a mixed slabs surrounding of Mo and W in sulfide active phase. Moreover, the investigation of the evolution of oxide catalysts during in situ sulfidation followed by Quick-XAS allows the understanding of this active phase genesis. The mixed active phase leads to the formation of more efficient active sites for hydrotreating reactions.

DFT calculations are now in progress for explaining the mixed sites efficiency taking into account Mo and W locations into the slabs. As perspective of this work, different sulfidation treatments could be studied in order to try to increase the quantity of mixed active phase.

The synthesis of mixed HPA with high molybdenum content is $SiMo_9W_3$ could be also considered observing the good HDS performances of $SiMo_{12}$ catalyst, as well as the use of ASA support for the treatment of heavy fuels.

Annex

1.1. Infrared (IR) spectroscopy

It is the absorption measurement of different IR frequencies by a sample positioned in the path of an IR beam. The main goal of IR spectroscopic analysis is to determine the chemical functional groups in the sample. Different functional groups absorb characteristic frequencies of IR radiation [1].

IR spectra were recorded using a Nicolet 510 Fourier Transform IR spectrometer. The samples were analyzed in the 200-1200 cm^{-1} spectral range using KBr pellets prepared with 1 wt % of sample dilution.

1.2. Rama n spectroscopy

Raman spectroscopy is a vibrational spectroscopy, like IR spectroscopy. It is based on Raman Effect [2]. When a sample is submitted to a monochromatic light, the main part of the light is elastically scattered with the same frequency (Rayleigh diffusion). Weakly intense scattered light quanta with frequencies different from those of the incident light quantum, are observed too: their frequencies are equal to $v_0 + v_i$ (anti-Stokes Raman diffusion) and to $v_0 - v_i$ (Stokes Raman diffusion), where v_i corresponds to the characteristic vibrational frequency of sample components [3]. Raman spectroscopy is a versatile method for analysis of a wide range of samples. It can be used for both qualitative by measuring the frequency of scattered radiations and quantitative analysis, which can be performed by measuring the intensity of scattered radiations. This characterization technique provides important information on chemical structures of HDT catalysts from the impregnation solution to the sulfided catalyst.

The Raman spectra of HPA based impregnating solutions and the catalysts were recorded at RT using an Infinity XY Horiba Jobin-Yvon Raman microprobe equipped with a photodiode array detector. The exciting laser source was the 532.16 nm line of a Nd-YAG laser. The wavenumber accuracy was 4 cm^{-1}.

1.3. Polarography

Polarography is a method of qualitative and quantitative physicochemical analysis, based on the registration of current-voltage curves (polarograms), which is a graphical representation of the current (I) as a function of the voltage (V) in the circuit consisting of the solution to be immersed in working (polarizing) and auxiliary (non-polarizable) electrodes [4]. This method is used to study the stages of the reduction of heteropolyacids of the different compositions.

The polarographic measurements were performed on a Tacussel (Pol 150) electrochemical analyzer monitored by a Tracemaster 5 programmer. A conventional single-compartment cell with standard three-electrodes configuration was used. Pt was used as an auxiliary electrode, while Ag/AgCl was used as a reference electrode. The working electrode was a glassy carbon disk (using a rate of stirring was equal to 840 rpm) allowing to study the heteropolymolybdates. Tungsten compounds being less reducible than molybdenum compounds, the study of $H_4SiW_{12}O_{40}$ that requires a mercury dropping electrode for reaching lower potential could not be performed. Deoxygenating of the solutions was carried out using argon as inert gas. The concentration in molybdenum atoms was equal 10^{-3} M in aqueous electrolytic solutions HCl (1 M)/ethanol (equivolume).

1.4. Single crystal X-Ray Diffraction (XRD)

Single-crystal X-ray Diffraction is a non-destructive analytical technique, which provides detailed information about the internal lattice of crystalline substances, including the unit cell dimensions, bond-lengths, bond-angles, and details of site-ordering. XRD is based on constructive interference of monochromatic X-rays and a crystalline sample. These X-rays are generated by a cathode ray tube, filtered to produce monochromatic radiation, concentrated, and directed toward the sample.

The interaction of the incident rays with the sample produces constructive interference (and a diffracted ray) when conditions satisfy Bragg's Law, see equation (1):

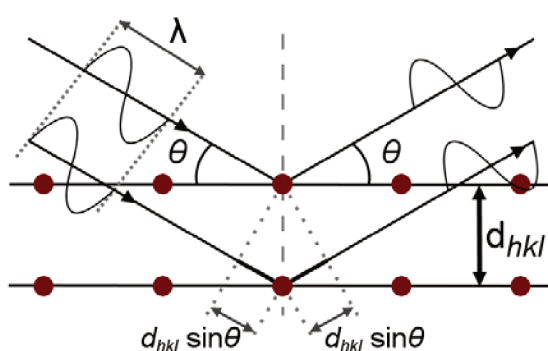$$2d_{hkl} \sin \theta = n\lambda \tag{1}$$

Fig. 1. Bragg diffraction. Bragg diffraction occurs when the difference in path lengths, $2d_{hkl}\sin\theta$, between two parallel in-phase waves is equal to an integer multiple of the incoming wavelength of the radiation, λ.

This law relates the wavelength of electromagnetic radiation to the diffraction angle and the lattice spacing in a crystalline sample. These diffracted X-rays are then detected, processed and counted [https://serc.carleton.edu/research_education/geochemsheets/techniques/SXD.html].

Single crystals suitable for XRD experiments have been isolated from the crystallization products and sticked on a glass fiber using vacuum grease. Crystals of β-$H_4[SiMo_3W_9O_{40}]\cdot 9H_2O$ are air stable and can be handled without precaution. On the opposite, crystals of the α-$H_4[SiMo_1W_{11}O_{40}]\cdot 30H_2O$ are very unstable under exposure in air and rapidly decompose. In this case, crystals were placed in grease, rapidly mounted and the data were collected under nitrogen flow at 100 K without any decomposition.

Both crystal structures have been refined using single crystal XRD data collected on a DUO-Bruker SMART apex diffractometer using the Mo Kα radiation by least square minimization on F_{hkl}. Intensities were extracted and corrected from the Lorentz-Polarization factor through the SAINT program. Multiscan absorption correction was applied using SADABS [5]. The structure was solved using Superflip [6] and refined using Jana 2006 [7].Specificities for each collection and refinement are given below in the crystal structure dedicated sections.

1.5. X-Ray Absorption Spectroscopy (XAS)

XAS is an essential tool to gather spectroscopic information about the electronic structure of materials. It is extremely useful for systems where single-crystal diffraction techniques are not readily applicable e.g., gas, liquid, solution, amorphous and polycrystalline solids, surfaces, polymer, etc.) [8] that allows applying XAS in many diverse fields.

Hitting of sample by x-rays results to that the electrons in an atom can jump from core energy level to an unoccupied outer level (excitation) by absorbing or losing (emitting) one quantum ($h\nu$) of electromagnetic radiation.

$$h\nu = E_f - E_i, \tag{2}$$

where E_i and E_f are the energies of the initial and final states, respectively.

When a beam of monochromatic X-rays passes through a sample, it inevitably loses its intensity via interaction with the material. The loss in intensity I is proportional to the original intensity I_0 and the thickness x of a sample:

$$\frac{I}{I_0} = e^{-\mu x}, \tag{3}$$

where μ is the linear absorption coefficient, which depends on the types of atoms and the density ρ of the material.

An absorption edge is the energy at which the absorption coefficient increases abruptly by several-fold. This discontinuity in then absorption coefficient corresponds to the ejection of a core electron from an atom, i.e. to produce a photoelectron. Thus, the energies of the absorbed radiation at these edges correspond to the binding energies of electrons in the K, L_I, L_{II}, L_{III}, etc.

shells of the absorbing elements, corresponding to the creation of electron holes in the 1s, 2s, $2p_{1/2}$, $2p_{3/2}$ etc. atomic subshells. The absorption threshold is associated with this transition and is characterized by the corresponding energy (E_0). XAS spectroscopy refers to the measurement of the X-ray absorption coefficient μ as a function of photon energy E above the threshold of an absorption edge [8].

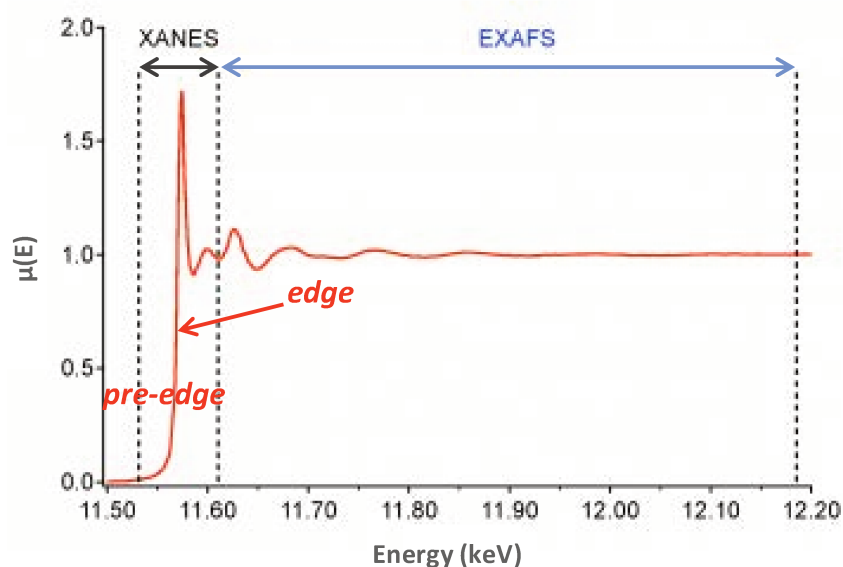In general, the absorption spectra are usually divided in three main regions (Fig. 2):

Fig. 2. Example of XAS spectrum showing three major regions.

pre-edge region ($E < E_0$) and edge limited to a few eV around the edge, contain bonding information, the electronic configuration, and the site symmetry. The edge position also contains information about the charge on the absorber;

the X-ray absorption near edge structure (XANES): > 50 eV above E0 where many-body interactions and multiple scatterings, allow to obtain an information about chemical states and symmetries;

the extended X-ray absorption fine structure (EXAFS): 50−1000 eV above the edge where the photoelectrons have high kinetic energy and single scattering by the nearest neighbouring atoms dominates shells provide information about the local geometric structure surrounding such as coordination numbers and inter-atomic distances.

The EXAFS oscillations result from the interference between the outgoing photoelectron wave and components of backscattered wave from neighboring atoms in the molecule, which start immediately past an absorption edge and extending to about 1000 eV above the edge [9]. In the absence of neighboring atoms (for a monatomic gas) a photoelectron ejected by absorption of an X-ray photon will travel as a spherical wave k with λ:

$$k = \frac{2\pi}{\lambda} = \sqrt{\frac{2m}{\hbar^2}} (E - E_0), \qquad (4)$$

where $\hbar = h/2\pi$, h is Planck's constant, E is the incident photon energy and E_0 is the threshold energy, and m is the mass of an electron.

In the presence of neighboring atoms, the outgoing photoelectron can be backscattered from the neighboring atoms, thereby producing an incoming wave, which can interfere either constructively or destructively. The amplitude and frequency of the sinusoidal oscillations of μ *vs* E depends on the type of the neighboring atoms and their distances away from the absorber, respectively [8]. The EXAFS function, $\chi(k)$, is described by the following formula:

$$\chi(k) = S_0^2 \sum_j N_j F_j (k) e^{-2\sigma_j^2 k^2} e^{-2r_j/\lambda_j(k)} \frac{\sin(2kr_j + \phi_{ij}(k))}{kr_j^2}, \qquad (5)$$

where S_0^2 is the amplitude reduction factor due to many-body effects, $F_j(k)$ is the backscattering amplitude from each of the N_j neighboring atoms of the jth type with a Debye-Waller factor of σ_j (to account for thermal vibration and static disorder), r_j is a distance between the absorbing atom and a neighbor, $\phi_{ij}(k)$ is the total phase shift experienced by the photoelectron, and $e^{-2r_j/\lambda_j(k)}$ is due to inelastic losses in the scattering process (due to neighboring atoms and the medium in between) with $\lambda_j(k)$ – the photoelectron mean free path.

EXAFS focusses on the immediate environment around each absorbing species (at distance out of 6 Å that is corresponded to 1-3 coordination shells). The structural parameters (the coordination number (N), the interatomic distance (r) and the Debye-Weller factor (σ)) can be determined separately for each coordination shell by using Fourier transformation and back-transform of the EXAFS signal. However, for determinations of these parameters the amplitude and phase functions must be known. It can be obtained from the EXAFS spectra of the reference compounds.

Ni K-edge (8333 eV), Mo K-edge (20 000 eV) and W L_{III} edge (10 207 eV) EXAFS measurements were carried out at the ROCK beamline of the SOLEIL synchrotron source [10]. The measurements were done at RT on powdery sample pressed into pellets, using Si(111) (for W) and Si(220) (for Mo and Ni) monochromators when characterizing bulk mixed SiMo$_1$W$_{11}$HPA, SiMo$_3$W$_9$ HPAs and dried catalysts at the oxide state. Sulfide catalysts were characterized after *in situ* sulfidation using the catalytic cell available at SOLEIL [11]. Powdered dried oxide catalysts were loaded in the cell and the *in situ* sulfidation was performed with a flow of 10% H$_2$S in H$_2$ at atmospheric pressure from room temperature to 400°C with a plateau of two hours.

For the whole measurements, XAS spectra were obtained in transmission mode with ionization chambers as X-Ray detectors. The ionization chambers were filled with a mixture of

argon and nitrogen (50:50) for measurements at the Mo K edge and (73:27) at the W L_{III} edge. Mo and W-edges EXAFS regions of the spectra were extracted and analyzed using Athena and Artemis software packages[34]. For Mo K edge, $k^3\chi(k)$ EXAFS signals were Fourier transformed in R-space pseudo-radial distribution functions using a Kaiser−Bessel window between $k_{min} = 4.8$ Å^{-1} and $k_{max} = 10.5$ Å^{-1} and dk window sill parameter equal to 2. For W L_{III} edge, FT of the $k^3\chi(k)$ EXAFS data were carried out from 3.5 to 16.8 Å^{-1} with a dk parameter equal to 2. The inverse Fourier Transformation of the EXAFS at the Mo K edge and W L_{III} edge were fitted using appropriate single and multiple scattering EXAFS paths generated from the cif files derived from crystallographic structures. During fitting of mixed bulk samples using Artemis, the distances between each concerned atoms and the coordination numbers were constrained by XRD single crystal data to check the transferability of amplitude and phase functions which will be further applied for catalysts EXAFS analysis. In this frame, the amplitude reduction factor S_0^2, which takes into account multielectronic effects, together with the enot factor which allows to match theoretical phase functions with the experimental EXAFS signals were first determined on the bulk HPA for the Mo and W edges. S_0^2 and enot values were after kept fixed for catalysts fitting. The number of fitted points was below the number of independent points according to the Nyquist criterion [12]. Typical accuracies for the determination of the coordination numbers and distances are 10 to 20 % and 1 to 2 %, respectively.

1.6. Nitrogen adsorption measurements

Two types of adsorption are existed: physical and chemical adsorption. Physical adsorption is conditional on weak Van der Waals forces of attraction. It is reversible process which results to formation of mono- and multimolecular layers of adsorbate on adsorbent. Chemical adsorption (chemisorption) is a result of a chemical interaction between adsorbate and adsorbent that it allowed to apply this phenomenon to determine the number of active sites on a surface. Chemisorption takes place with formation of monomolecular layers. In chemisorption the force of attraction is very strong, therefore it is irreversible process.

The physical adsorption of nitrogen is the most commonly used method for obtaining information on the surface areas and porous characteristics of solids from the adsorption isotherm (a function of the amounts of adsorbate on the surface of adsorbent against the adsorption pressure at constant temperature). Six different types of adsorption isotherm are identified depending on their shape. Several theories to analyse nitrogen adsorption/desorption isotherms obtained at liquid nitrogen temperature (77 K) were proposed.

According to the Langmuir theory [13] be supposed that for the first layer the rate of evaporation is equal to rate of condensation; the adsorption energy (ΔH_{ads}) is independent of the surface coverage.

The method based on Brunauer–Emmett–Teller (BET) theory [14] is the most widely used technique for determining surface area. This approach based on the Langmuir theory and the following postulates:

1. gas molecules physically adsorb on a solid in layers infinitely;

2. there is no interaction between each adsorption layer;

3. the Langmuir theory can be applied to each layer.

The BET equation is

$$\frac{p}{v(p_0-p)} = \frac{1}{v_m c} + \frac{c-1}{v_m c} \cdot \frac{p}{p_0},$$ (6)

where p and p_0 are the equilibrium and the saturation pressure of adsorbates, respectively, v_m is the volume adsorbed in one complete monomolecular layer, and c is the BET constant.

$$c = e^{\frac{E_1-E_L}{RT}},$$ (7)

where E_1 and E_L are the heat of adsorption for the first layer, and the heat of liquefaction, respectively.

The linear relationship of this equation has been found to hold in the range of $0.05 < p/p_0 < 0.35$.

The specific surface area (SSA) can be calculated by the equation:

$$S = \frac{V_m \cdot a \cdot N_a}{m \cdot 22400},$$ (8)

where S is specific surface area (m^2/g), a is effective cross-sectional area of one adsorbate molecule (m^2) for nitrogen is 0.162 nm^2, N is Avogadro constant (6.022×10^{23} mol^{-1}), m is mass of test powder (g).

One of the major characteristic of porous solids is size of a pore. According to the IUPAC classification [15] all pores depending on their size can be divided into three groups of materials with micropores (diameter <2 nm), mesopores (diameter 2-50 nm) and macropores (diameter >50 nm).

The method had been developed by Barrett-Joyner-Halenda (BJH) [16] is the most commonly used for deriving the pore size distribution from an appropriate nitrogen isotherm.

The method based on a change of adsorbed volume depending on pressure p/p$_0$ is caused by capillary condensation. Capillary condensation is a secondary process that requires the preformation of an adsorbed layer on the pore walls formed by multilayer adsorption. Both

processes generally occur simultaneously. The Kelvin equation relates the curvature of the meniscus present in a pore to the p/p_0 value associated with condensation.

$$lp\frac{p}{p_0} = \frac{-2\sigma V_m cos\theta}{RTr_k}, \tag{9}$$

where: p and p_0 are the equilibrium and the saturation pressure of adsorbates, respectively, σ is the surface tension of the liquid condensate, V_m is molar volume of the liquid condensate, r_k is the Kelvin radius, θ is wetting angle, R is universal gas constant and T is temperature.

The textural characteristics of the prepared oxide catalysts were determined by nitrogen adsorption performed at 77 K on a Quantachrome Autosorb-1 adsorption porosimeter. The specific surface area was calculated using the BET method at relative partial pressures (p/p_0) ranging from 0.05 to 0.3. The total pore volume (at p/p_0 of 0.99) and pore size distribution were calculated based on the desorption curve using the BJH model. Before the measurement, the samples were outgassed under vacuum ($<10^{-1}$Pa) at 350 ºC for 4 h.

1.7. X-ray Photoelectron Spectroscopy (XPS)

X-ray photoelectron spectroscopy (XPS) is a surface-sensitive quantitative spectroscopic technique that measures the elemental composition at the parts per thousand range, empirical formula, chemical state and electronic state of the elements that exist within a material. XPS spectra are obtained by irradiating a material with a beam of X-rays, while simultaneously measuring the kinetic energy and number of electrons that escape from the top 0 to 10 nm of the material being analyzed.

The main process of photoelectron spectroscopy is the absorption of a quantum with energy and the emission of an electron called a photoelectron, whose kinetic energy, measured from the corresponding zero energy, depends on the binding energy of the electron in the target atom. In this process, the incident photon transfers all its energy to the bound electron and the element is identified by measuring the energy of the electrons leaving the sample without losing energy.

XPS is a very good quantitative method for determining the ratio of different chemical forms of one element in a homogeneous sample. In this work, this method was used to determine the composition of synthesized heteropolyacids, as well as to determine the composition of particles of the active phase on the surface of the support in different states (oxidic and after sulfidation). The XPS spectrum of typical MoS_2/Al_2O_3-type catalyst is illustrated on Fig. 3.
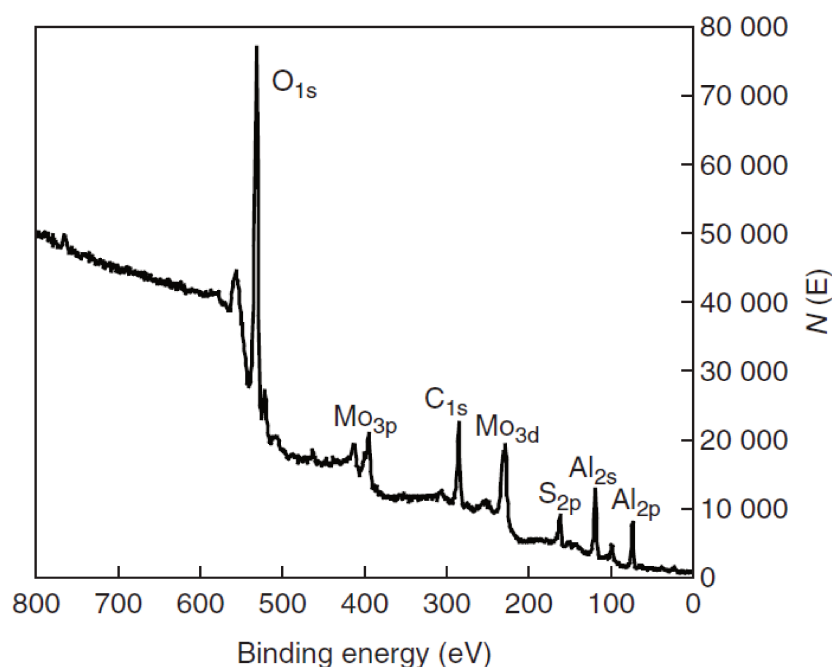
Fig. 3. Typical XPS spectrum of an MoS$_2$/Al$_2$O$_3$ catalyst [17]

The spectra were obtained on a Kratos Axis Ultra DLD spectrometer using a monochromatic AlK_α source (hν = 1486.6 eV, 150 W). The binding energy (BE) scale of the spectrometer was preliminarily calibrated using the position of the peaks for the Au 4f$_{7/2}$ (83.96 eV) and Cu 2p$_{3/2}$ (932.62 eV) core levels of pure metallic gold and copper. The samples were mounted on a holder using double-sided adhesive tape. For the non-conductive samples, the Kratos charge neutraliser system was used and the spectra were charge-corrected to provide the C 1s spectral component of adventitious carbon (C–C, C–H) at 284.8 eV. In addition to the survey photoelectron spectra, narrow spectral regions (Al 2p, S 2p, Mo 3d, W 4f, Ni 2p, C 1s and O 1s) were recorded. The pass energy of the analyzer was 160 eV for the survey spectra and 40 eV for the narrow scans. The individual spectral regions were analyzed to determine the BE of the peaks, identify the chemical state of the elements and calculate the relative ratios of the elements on the catalyst surface.

The collected spectra were analysed using the CasaXPS software program (Version 2.3.16) after applying a Shirley background subtraction. Gaussian (30 %) – Lorentzian (70 %) peaks were used for spectra decomposition. The decompositions of the S 2p, Ni 2p, Mo 3d and W 4f XPS spectra were performed using the appropriate oxide and sulfided references as supported monometallic catalysts.

XPS decomposition enabled the absolute quantification of each species:

$$C(j)_{\mathrm{T}} \text{ (at. \%)} = \frac{A_j / S_j}{\sum\limits_{i=1..n} A_i / S_i} \times 100,$$ (10)

where A_i is the measured area of species i, S_i is the sensitivity factor of the atom related to species i (provided by the manufacturer) and $C(j)_T$ is the absolute content of species j.

The relative concentrations of each species Mo^{6+}, MoS_xO_y, MoS_2, W^{6+}, WS_xO_y and WS_2 were determined for all sulfided catalysts. For example, the relative amount of WS_2 was determined using the following equation:

$$[WS_2] (\%) = \frac{A_{WS_2}}{A_{WS_2} + A_{WS_xO_y} + A_{W^{6+}}} \times 100 , \qquad (11)$$

where A_X represents the peak area of species x.

We determined the relative concentrations of each Ni species, nickel oxide Ni^{2+}, NiS_x, NiMo(W)S, for every Ni-promoted sulphided catalyst. For example, the relative amount of NiMoS was determined using the following equation:

$$[NiMoS] (\%) = \times \frac{A_{NiMoS}}{A_{NiMoS} + A_{NiS_x} + A_{Ni^{2+}}} \; 100 , \qquad (12)$$

where A_X represents the peak area of species x.

The absence of any signal at 169.0 eV (characteristic of sulfates) indicates that sulfided catalysts were not reoxidized during the transfer of the solid from the sulfiding reactor to the XPS instrument.

1.8. High-resolution transmission electron microscopy (HRTEM)

Transmission electron microscopy (TEM) is a microscopy technique, where a beam of electrons is transmitted through an ultra thin sample. HRTEM provides detailed information of particle structure. The principal setup of TEM is illustrated on the Fig. 4. An electron source (gun) produces a stream of electrons. The condenser lenses are used in order to form the electron beam which illuminates the sample. The beam strikes the specimen and a part of it gets transmitted through it. This transmitted beam is focused by the objective lenses into an image. This image is then fed down the column through the projector lenses, which enlarges the image, depending upon the set magnification. The darker areas of the image represent the thicker or denser region of the sample (fewer electrons were transmitted) and the lighter areas of the image represent those areas which are thinner or less dense (more electrons were transmitted).
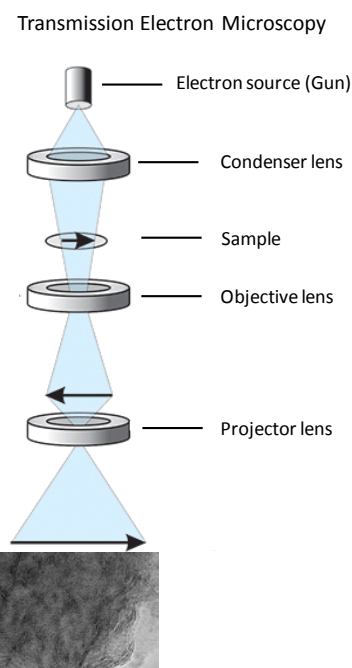

Fig. 4. The principal setup of TEM.

HRTEM was used to determine the morphology of particles of the active phase on the surface of the catalyst, as well as to determine the geometric characteristics of particles of the active phase of catalysts, based on the hexagonal model.

HRTEM was carried out using a Tecnai G2 20 electron microscope with a 0.14 nm lattice-fringe resolution and an accelerating voltage of 200 kV. Freshly sulfided samples were ground under an inert atmosphere and dispersed in ethanol. The suspension was collected on carbon films supported on copper grids and 10 – 15 representative micrographs were obtained for each catalyst in high–resolution mode. Typically, the length and stacking of at least 500 slabs were measured for each catalyst. Distribution in length and stacking of the slabs was determined. To measure the extent of Mo(W)S_2 dispersion, the average fraction of Mo(W) atoms at the Mo(W)S_2 edge surface (D) was calculated, assuming that the Mo(W)S_2 slabs were perfect hexagons [18]. Mo(W)S_2 dispersion (D) was statistically evaluated by dividing the total number of Mo(W) atoms at the edge surface (W_e), including corner sites (W_c), by the total number of Mo(W) atoms (W_T) using the slab sizes measured in the TEM micrographs:

$$D = \frac{W_e + W_c}{W_T} = \frac{\sum\limits_{i=1..t} 6n_i - 6}{\sum\limits_{i=1..t} 3n_i^2 - 3n_i + 1}, \tag{13}$$

where n_i is the number of Mo(W) atoms along one side of the Mo(W)S$_2$ slab, as determined by its length, and t is the total number of slabs in the TEM micrograph.

The average slab length of (Ni)Mo(W)S slabs was calculated as follows:

$$\overline{L} = \frac{\sum\limits_{i=1..t} l_i}{n}, \tag{14}$$

where l_i is the length of slab i, n is the total number of slabs.

The number of slabs per stack was determined to obtain the average stacking degree ($\overline{N}$):

$$\overline{N} = \frac{\sum\limits_{i=1..t} n_i N_i}{\sum\limits_{i=1..t} n}, \tag{15}$$

where n_i is the number of stacks in N_i layers.

High resolution high-angle annular dark-field scanning transmission electron microscopy (HR HAADF-STEM) analyses were performed using a FEG TEM/STEM system (Titan Themis FEI) operated at 200 kV, equipped with a monochromator and a probe Cs corrector. For HAADF acquisition, the spot size was 9 with a screen current of ~50 pA and a camera length of 115 mm, corresponding to inner and outer diameters of annular detector of ~50 and ~200 mrad, respectively. Samples were prepared in the same way as for HRTEM analysis.

1.9 High angle annular dark field scanning transmission electron microscopy (HAADF-STEM)

Another TEM technique that can be used for imaging is scanning transmission electron microscopy (STEM). It scans the region of interest with a fine focused electron beam (i.e. 0.05 – 0.5 nm probe size) collecting the scattered electrons using a detector (Fig. 5).
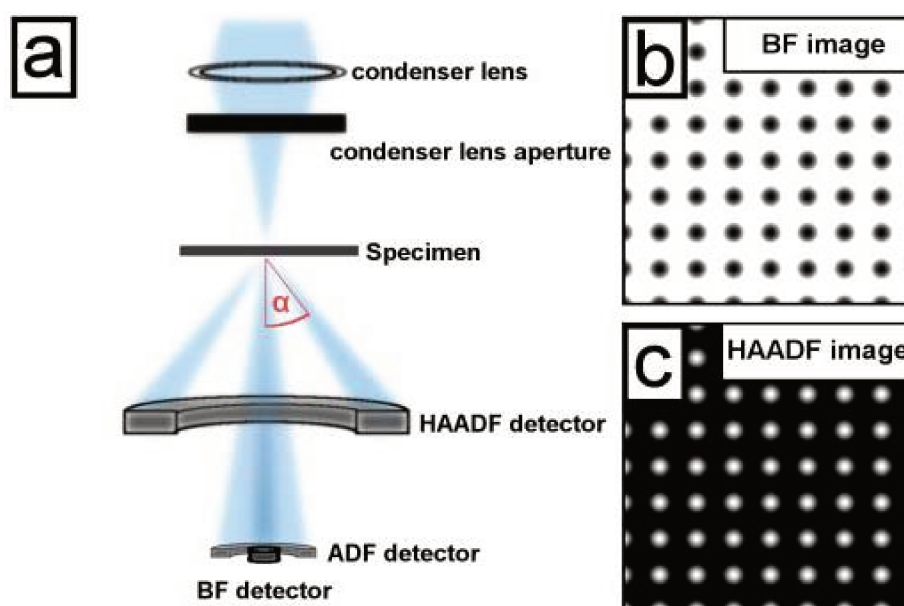
Fig. 5. Scanning transmission electron microscopy imaging. (a) Schematic of the electron ray path for STEM imaging showing the position of BF, ADF and HAADF detectors, as well as their relationship with the scattering angle α. (b) Simulated STEM-BF and (c) STEM-HAADF images of FeO along a <001> zone axis where the atomic columns are revealed in black (BF image) and white (HAADF image), respectively.

The advantage of STEM over HRTEM imaging is the absence of contrast reversal, which enables a direct interpretation of the contrast in a STEM image. In STEM bright-field (STEM-BF), the BF signal is a coherent signal that relies on phase contrast, it is therefore more sensitive to samples with lower atomic numbers, such as the carbon substrate of TEM grids or biological samples. The BF-STEM signal gained is similar to a conventional TEM image and is harder to interpret as the phase contrast means the signal is not directly proportional to atomic number or thickness. An annular dark-field (ADF) detector collects the electrons scattered at higher angles excluding the low-angle scattered electrons (e.g. the direct beam). A STEM-BF image results from the interference of the direct beam with low-angle scattered electrons (i.e. elastic and inelastic electrons). STEM-BF using an annular detector has shown promising results in imaging light elements [19,20]. On the other hand, high-angle annular dark-field (HAADF) in STEM has attracted much interests because it produces image contrast that is sensitive to the atomic number ($I \propto Z^2$), sometimes called Z-contrast imaging [21].

For qualitative determination of atom species and calculations of atomic column distances, HAADF STEM imaging is widely used due to the simple interpretation and the absence of contrast reversal. In this thesis, prepared sulfided NiMo(W)/Al_2O_3 catalysts were characterized by HAADF STEM to determine a structure of sulfided active phase species especially the atom position determination.

High resolution high-angle annular dark-field (HRHAADF) imaging has been performed at 200 kV on a TITAN Themis FEI scanning transmission electron microscope (S/TEM). The microscope is equipped with a monochromator and a Cs probe corrector. For HAADF acquisition, the spot size was 9 with a screen current of ~50 pA and a camera length of 115 mm, corresponding to inner and outer diameters of the annular detector of ~50 and ~200 mrad, respectively. The samples were prepared in the same way as for HRTEM analysis. More than 50 slabs were observed on each studied catalyst.

1.10. Examination of the catalytic properties

All catalysts were tested in a hydrotreating of model feed in a bench-scale flow reactor under pressure of hydrogen (Fig. 6). Examination of DBT HDS activity and naphthalene HYD of unpromoted catalysts was performed in a fixed-bed microreactor under 320 ºC, 3.0 MPa of hydrogen, with a LHSV (liquid hourly space velocity) of 10 h^{-1} and a 500 NL/L volume ratio of hydrogen to feed. A mixture of DBT (1500 ppm S), naphthalene (3 wt. %), hexadecane (as an internal standard, 1 wt. %) and toluene (as a solvent) was used as a model feedstock for evaluation of HDS and HYD performances.
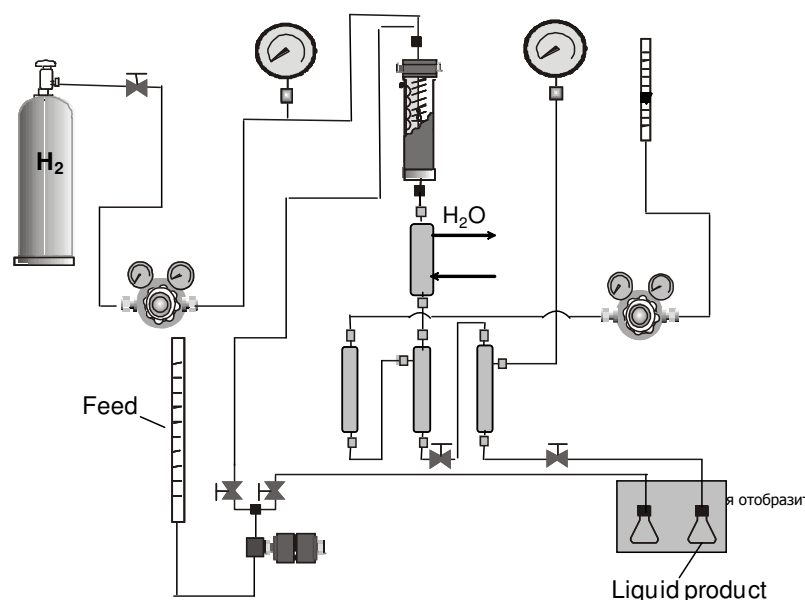

Fig. 6. Scheme of laboratory hydrotreating bench-scale flow unit.

Examination of DBT HDS activity and naphthalene HYD of unpromoted catalysts was performed in a fixed-bed microreactor under 320 ºC, 3.0 MPa of hydrogen, with a LHSV (liquid hourly space velocity) of 10 h^{-1} and a 500 NL/L volume ratio of hydrogen to feed. A mixture of

DBT (1500 ppm S), naphthalene (3 wt. %), hexadecane (as an internal standard, 1 wt. %) and toluene (as a solvent) was used as a model feedstock for evaluation of HDS and HYD performances.

Ni-promoted catalysts were tested in HDT of the mixtures: 1) DBT (1500 ppm S), naphthalene (3 wt. %), hexadecane (as an internal standard, 1 wt. %) and toluene (as a solvent); 2) DBT (1500 ppm S), naphthalene (3 wt. %), quinoline (500 ppm N), hexadecane (as an internal standard, 1 wt.%) and toluene (as a solvent). The tests were performed in a fixed-bed microreactor at 280 ºC, 3.0 MPa of hydrogen, with a LHSV of 40 h^{-1} and a 500 NL/L volume ratio of hydrogen to feed.

In a typical HDT experiment, 0.6 g (for unpromoted catalysts) or 0.2 g (for Ni-promoted catalysts) sample of the catalyst (0.25 – 0.50 mm) was diluted with 0.6 cm^3 of low-surface-area carborundum (0.2 – 0.4 mm) and placed in the centre of the reactor (the reactor had an internal diameter of 0.8 cm). Prior to the catalytic activity tests, the catalysts were sulfided with a mixture of DMDS (2 wt. % of sulfur) and decane at 3.5 MPa in a stepwise procedure over 10 h at 240 ºC and 8 h at 340 ºC. The liquid product compositions of the samples collected every hour were determined using a Crystall-5000 Gas Chromatograph equipped with a 30 m OV-101 column. The reaction products were identified by matching retention times with those of commercially available standards and by GC/MS analysis using a Finnigan Trace DSQ. All catalysts exhibited stable performance, achieving a steady state after 7 – 10 h.

The rate constants of the pseudo-first-order reactions of the DBT HDS and naphthalene HYD were determined using the following equations:

$$k_{HDS} = -\frac{F_{DBT}}{W}\ln(1-x_{DBT}), \; k_{HYD} = -\frac{F_{Naph}}{W}\ln(1-x_{Naph}) \text{ and } k_{HDN} = -\frac{F_{Qui}}{W}\ln(1-x_{N}) \tag{16}$$

where k_{HDS}, k_{HYD} and k_{HDN} are the pseudo-first-order reaction constants for the DBT HDS, naphthalene HYD and quinoline HDN (mol g^{-1} h^{-1}), respectively, x_{DBT}, x_{Naph} and x_{N} are the conversions (%) of DBT, naphthalene, quinoline and its nitrogen-containing products, respectively, F_{DBT}, F_{Naph} and F_{Qui} are the reactant flow in moles (mol h^{-1}) and W is the weight of the catalyst (g).

The HDS products from DBT included biphenyl (BP) via the direct desulfurisation (DDS) pathway, as well as cyclohexylbenzene (CHB) and dicyclohexyl (DCH) from the HYD pathway. Only traces of hydrogenated tetrahydro- and perhydrodibenzothiophenes were observed. The HYD/DDS selectivity was calculated according to the reaction network for DBT HDS (Chapter 1 Scheme 1):

$$S_{HYD/DDS} = \frac{k_{HYD}}{k_{DDS}} = \frac{C_{CHB} + C_{DCH}}{C_{BP}}, \tag{17}$$

where C_{CHB}, C_{BCH} and C_{BP} are the concentrations (wt. %) of CHB, DCH and BP in the reaction products, respectively.

The turnover frequencies (TOF, s^{-1}) normalised on edge sites of $Mo(W)S_2$ slabs for the HDS of DBT, HYD of naphthalene allowed to get more complete understanding of the catalytic properties of the active phase species. TOF values were calculated using the following equations:

$$TOF_{HDS} = \frac{F_{DBT} \cdot x_{DBT}}{W \cdot \left(\dfrac{C_{WS_2}}{Ar_W} + \dfrac{C_{MoS_2}}{Ar_{Mo}} \right) \cdot D \cdot 3600}, \; TOF_{HYD} = \frac{F_{Naph} \cdot x_{Naph}}{W \cdot \left(\dfrac{C_{WS_2}}{Ar_W} + \dfrac{C_{MoS_2}}{Ar_{Mo}} \right) \cdot D \cdot 3600},$$

$$TOF_{HDN} = \frac{F_{Qui} \cdot x_N}{W \cdot \left(\dfrac{C_{WS_2}}{Ar_W} + \dfrac{C_{MoS_2}}{Ar_{Mo}} \right) \cdot D \cdot 3600} \tag{18}$$

where, F_{DBT}, F_{Naph} and F_{Qui} are the reactant flow (mol h^{-1}); x_{DBT}, x_{Naph} and x_N are the conversions (%) of DBT, naphthalene, quinoline and its nitrogen-containing products, respectively; W is the weight of the catalyst (g); C_{WS_2} and C_{MoS_2} are the effective content of W and Mo, respectively, in $Mo(W)S_2$ species (wt. %); D is the dispersion of $Mo(W)S_2$ species; Ar_W and Ar_{Mo} are the atomic mass of tungsten (183.9 g/mol) and molybdenum (95.9 g/mol).

References

1 C.-P. Sherman Hsu. Handbook of Instrumental Techniques for Analytical Chemistry, (1997), P.247-283

2 C.V. Raman, K.S. Krishnan. A New Type of Secondary Radiation // *Nature*, V.121, (1928), P.501-502.

3 M Digne, K. Marchand, P. Bourges. Monitoring Hydrotreating Catalysts Synthesis and Deactivation using Raman Spectrometry// *Oil & Gas Science and Technology,* V. 62 (2007), P. 91-99.

4 A.J. Bard, L.R. Faulkner. Electrochemical Methods: Fundamentals and Applications (2 ed.), (2000), Wiley. ISBN 0-471-04372-9.

5 G. Sheldrix, SADABS. Area Detector Absorption Correction, Madison: WI, 1996.

6 L. Palatinus and G. Chapuis. SUPERFLIP- a computer program for the solution of crystal structures by charge flipping in arbitrary dimensions // *J. Appl. Cryst.,* (2007), V.40, P.786-790.

7 V. Petricek, M. Dusek and L.Palatinus, Kristallogr. Crystallographic computing system JANA2006: General features. (2014), V. 229, P.345-352.

8 B. K. Teo, EXAFS: Basic principles and data analysis. Springer Verlag (1986).

9 J. Yano,V. K. Yachandra // *Photosynth Res* (2009) 102:241–254.

10 V. Briois, C. La Fontaine, S. Belin, L. Barthe, T. Moreno, V. Pinty, A. Carcy, R. Girardot, E. Fonda, ROCK: the new Quick-EXAFS beamline at SOLEIL // *JPCS* (2016), V.712, P.1-6.

11 C. La Fontaine, L. Barthe, A. Rochet and V. Briois. X-ray absorption spectroscopy and heterogeneous catalysis: performances at the SOLEIL's SAMBA beamline // *Catal. Today*, (2013), V.205, P.148–158.

12 E.A. Stern. Number of relevant independent points in x-ray-absorption fine-structure spectra // *Phys. Rev. B.,* (1993), V.48, P.9825-9827.

13 I. Langmuir // *J. Am. Chem. Soc*. (1916) V.38, P.2221.

14 S. Brunauer, P.H. Emmett, E. Teller. Adsorption of Gases in Multimolecular Layers // *J. Am. Chem. Soc.* (1938), V.60, P. 309.

15 J. Rouquerol, D. Avnir, C. W. Fairbridge, D. H. Everett, J. M. Haynes, N. Pernicone, J. D. F. Ramsay, K. S. W. Sing and K. K. Unger. Physical and biophysical chemistry division commission on colloid and surface chemistry including catalysis // *Pure & Appl. Chem*., V. 66, (1994), P. 1739-1758,.

16 E. D. Barrett, L. G. Joyner, and P. P. Halenda. The Determination of Pore Volume

and Area Distributions in Porous Substances. I. Computations from Nitrogen Isotherms // *J. Am. Chem. Soc.*, V. 73, (1951), P. 373–380,

17 P. Beccat, P. Da Silva, Y. Huiban, S. Kasztelan. Quantitative Surface Analysis by Xps (X-Ray Photoelectron Spectroscopy): Application to Hydrotreating Catalysts // *Oil & Gas Science and Technology – Rev. IFP*, V.54, (1999), P.487-496.

18 S. Kasztelan, H. Toulhoat, J. Grimblot, J. P. Bonnelle. A geometrical model of the active phase of hydrotreating catalysts. // *Applied Catalysis*. (1984), V.13. P.127–159.

19 J.M. Cowley, M.S. Hansen, S.-Y. Wang. Imaging modes with an annular detector in STEM // *Ultramicroscopy* V. 58, (1995), P.18–24.

20 R. Ishikawa, E.Okunishi, H.Sawada, Y. Kondo, F.Hosokawa, E. Ab // *Nat. Mater.* V.10, (2011), P.278–281.

21 S. J. Pennycook, D.E. Jesson. High-resolution Z-contrast imaging of crystals // *Ultramicroscopy* V.37, (1991), P.14–38.

Supporting Information for Chapter 2

Characterization of bulk $H_4[SiMo_nW_{12-n}O_{40}]$ HPAs
EXAFS

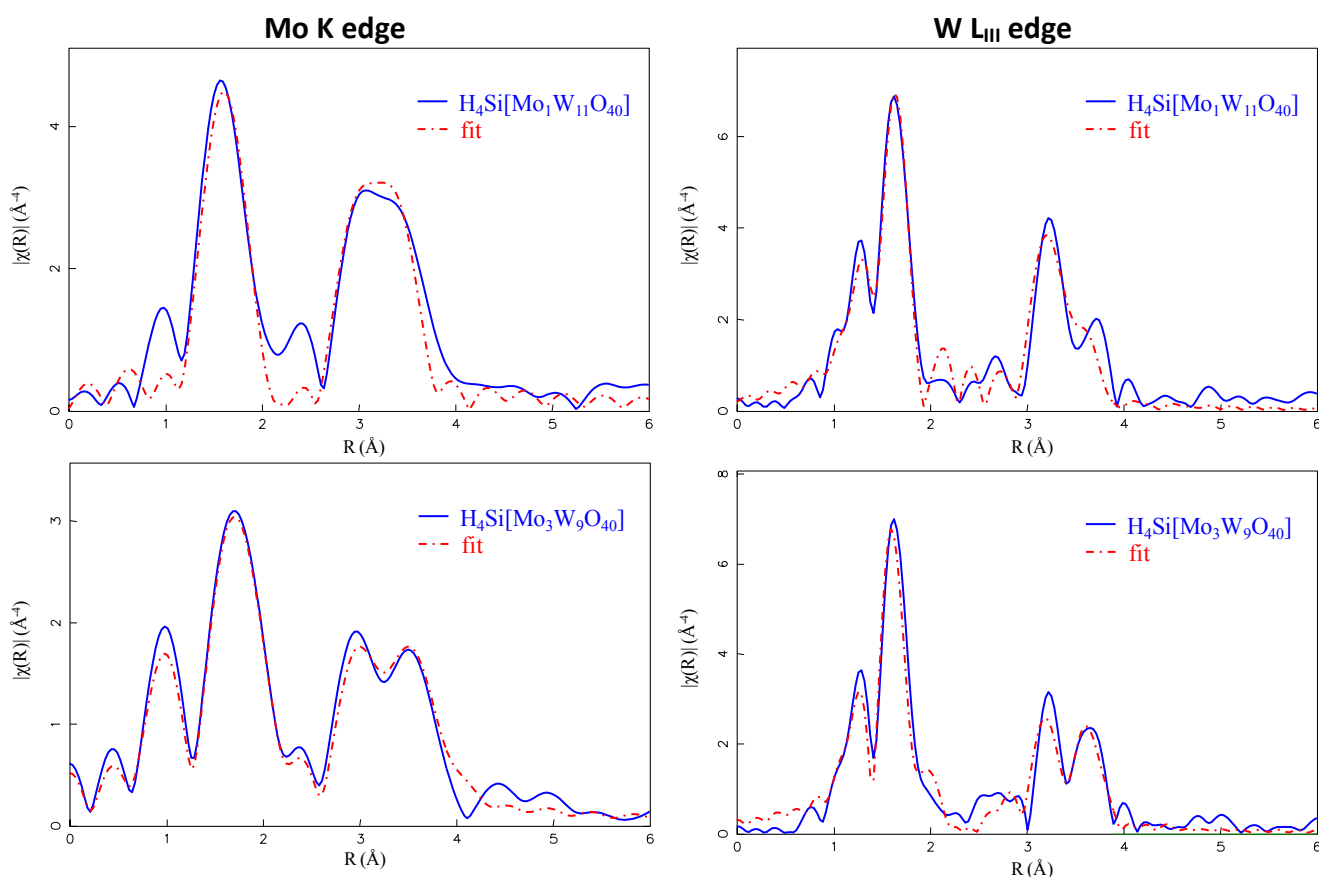**Mo K edge**   **W L_{III} edge**

Fig. S1. Magnitude of the Fourier transform of the Mo K edge and W L_{III} edge spectra (solid line) and model (dotted line) for bulk $H_4Si[Mo_1W_{11}O_{40}]$ and $H_4Si[Mo_3W_9O_{40}]$ HPAs.
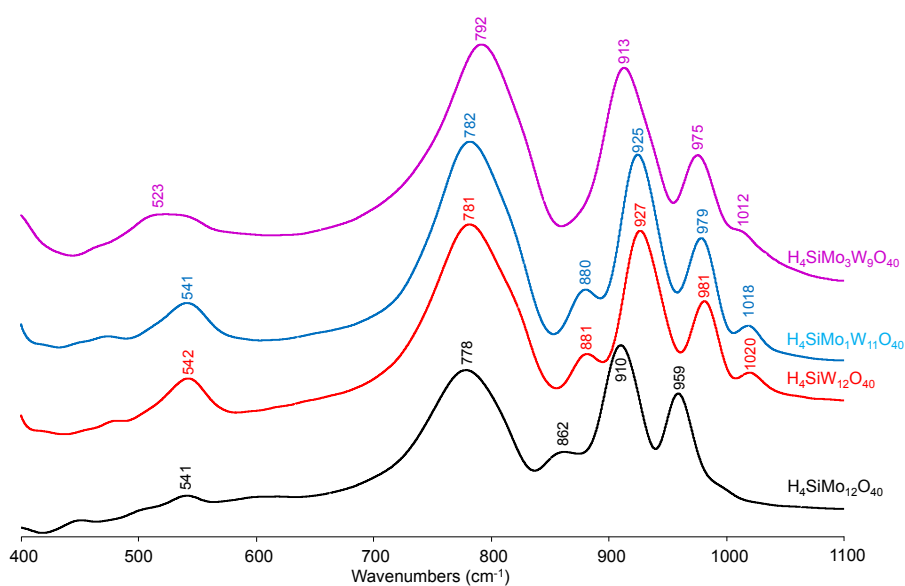
IR Spectroscopy

Fig. S2. IR spectra of bulk HPA: comparison of mixed HPA with the monometallic ones

Fig. S2 presents IR spectra of $H_4[SiMo_1W_{11}O_{40}]$, $H_4[SiMo_3W_9O_{40}]$, $H_4[SiMo_{12}O_{40}]$ and $H_4[SiW_{12}O_{40}]$. According to literature data on $SiW_{12}O_{40}$ IR characterization,[1,2] characteristic bands are assigned to the Keggin structure: Si-O and $W=O_t$ vibrations stretching mode (t stands for terminal) are observed at 927 and 981 cm^{-1} respectively while lines at 880 and 781 cm^{-1} are assigned to $W-O_b-W$ and $W-O_c-W$ vibrations (O_b oxygen atoms between two octahedra of different W_3O_{13} groups and O_c, oxygen atoms between two octahedra from a same W_3O_{13} group) . In the low wavenumbers (520-540 cm^{-1}), vibrations are due to squeletal deformations of the Keggin unit. All these vibrations were observed in mixed heteropolyanions with small variations in wavenumber. The IR spectra of mixed HPA are very close and look like that of $H_4SiW_{12}O_{40}$ indicating that in the mixed HPA Mo- and W-oxygen vibrational modes cannot be observed separately. $H_4[SiMo_1W_{11}O_{40}]$ IR spectrum is also in agreement with that of $SiMoW_{11}O_{40}$ prepared as microtubes reported by Shen et al.[10]
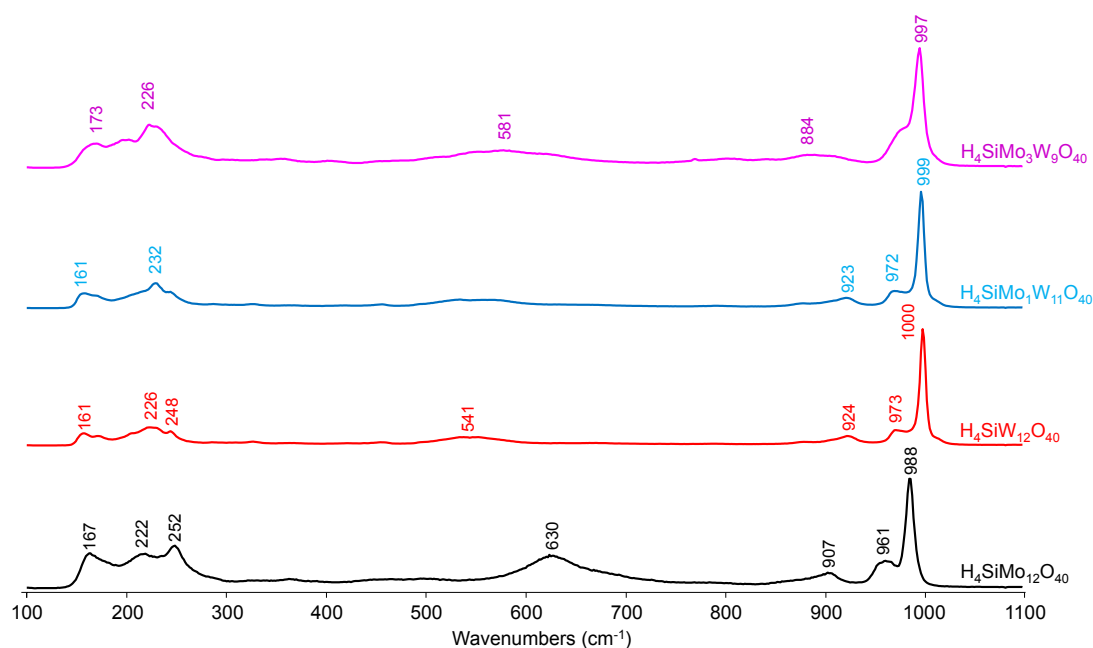
Raman Spectroscopy

Fig. S3. Raman spectra of bulk HPA: comparison of mixed HPA with the monometallic ones

Fig. S3 presents Raman spectra of $H_4[SiMo_1W_{11}O_{40}]$ and $H_4[SiMo_3W_9O_{40}]$. For comparison purposes, $H_4[SiMo_{12}O_{40}]$ and $H_4[SiW_{12}O_{40}]$ spectra have also been added on this figure. The mixed heteropolyacids present very close Raman spectra (as already observed for IR analysis) that are dominated by a main peak corresponding to a $M=O_t$ terminal vibration at the same wavenumber (about 997 cm^{-1}). This value is very similar to that of the $W=O_t$ vibration observed in the $H_4[SiW_{12}O_{40}]$ spectrum. The relative simplicity of the mixed MoW HPA Raman

spectra shows that these spectra do not correspond to a mixture of both $H_4[SiMo_{12}O_{40}]$ and $H_4[SiW_{12}O_{40}]$ monometallic spectra. For mixed $SiMo_1W_{11}O_{40}{}^{4-}$ and $SiMo_3W_9O_{40}{}^{4-}$, due to similarity between Mo and W, $Mo=O_t$ and $W=O_t$ cannot be distinguished and the redistribution of potential energy in the mixed anion leads to the complete mixing of $W=O_t$ and $Mo=O_t$ vibrators.
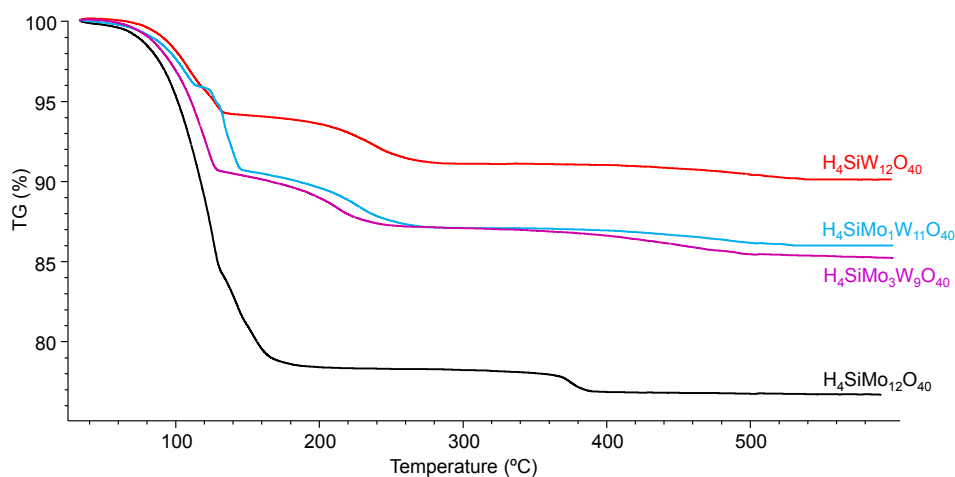
DTA-TGA analysis

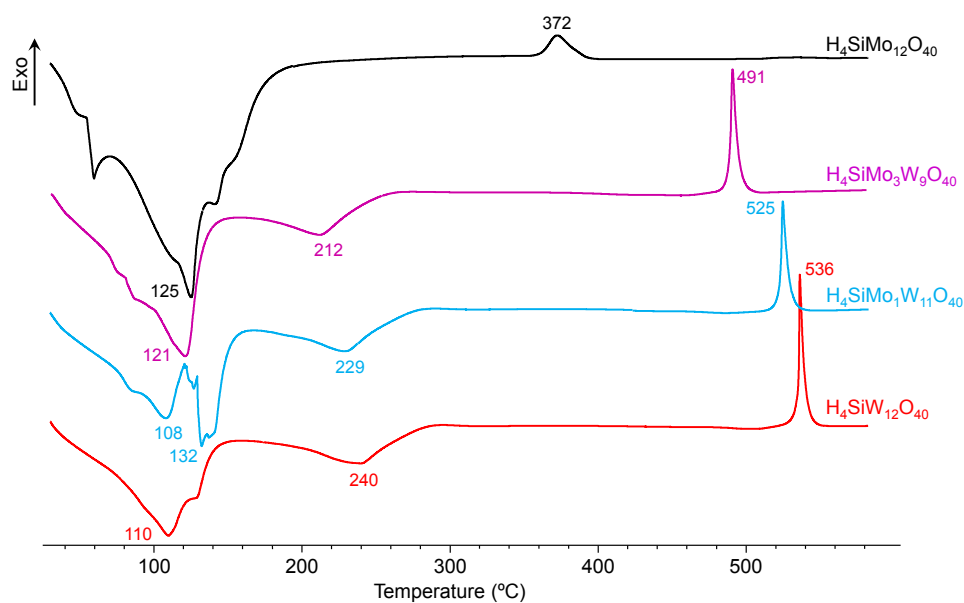

Fig. S4. TGA curves of mixed and monometallic HPA

Fig. S5. DSC curves of mixed and monometallic HPA

Thermal stability of mixed and monometallic HPA was evaluated by thermogravimetric analysis (TGA) and respective DSC analyses were also carried out. TG curves are reported Fig. S4 showing that the thermal behavior of the mixed HPA and silicotungstic acid is very similar

and differs slightly from that of silicomolybdic acid. For this later well-known acid, an important first loss (23%) until 180°C, also characterized by an important endothermic peak in DSC (Fig. S5), corresponds to the release of 29 crystalline water molecules. After 180°C, a plateau is reached indicating the formation of the stable dehydrated $H_4SiMo_{12}O_{40}$ until 360°C. The second weight loss of 1.6 % is attributed to the loss of constituting water molecules giving rise to separate MoO_3 oxide and non-crystalline SiO_2. The exothermic peak in the DSC curve indicates a crystallization temperature around 370°C for MoO_3.

For silicotungstic acid and mixed HPA, the first weight loss observed between 25 and 180°C in $H_4SiMo_{12}O_{40}$ spreads out especially as the amount of tungsten increases reaching 260°C for silicotungstic acid. Moreover the important departure of crystalline water, also indicated by the endothermic peaks, occurs in two steps indicating the formation of a stable intermediate hydrate as $H_4SiW_{12}O_{40}$, $6\ H_2O$ around 120°C in agreement with the weight loss of 6.7% before the formation of the dehydrated compounds corresponding to the plateau in the TG curves. The loss of constitutive water leading to the oxides formation is observed until the WO_3 crystallization represented by the exothermic peaks in DSC curves at 536, 525 and 491°C for $H_4SiW_{12}O_{40}$, $H_4SiMoW_{11}O_{40}$ and $H_4SiMo_3W_9O_{40}$ respectively, the substitution of W by Mo slightly decreasing the thermal stability of the mixed HPA compared to that of silicotungstic acid.

[1] C. Rocchiccioli-Deltcheff, M. Fournier, R. Franck and R. Thouvenot, *Inorg. Chem.*,1983, **22**, 207-216.

[2] C. Rocchiccioli-Deltcheff, R. Thouvenot, R.Franck, *Spectrochim. Acta,* 1976, **A32**, 587-597.
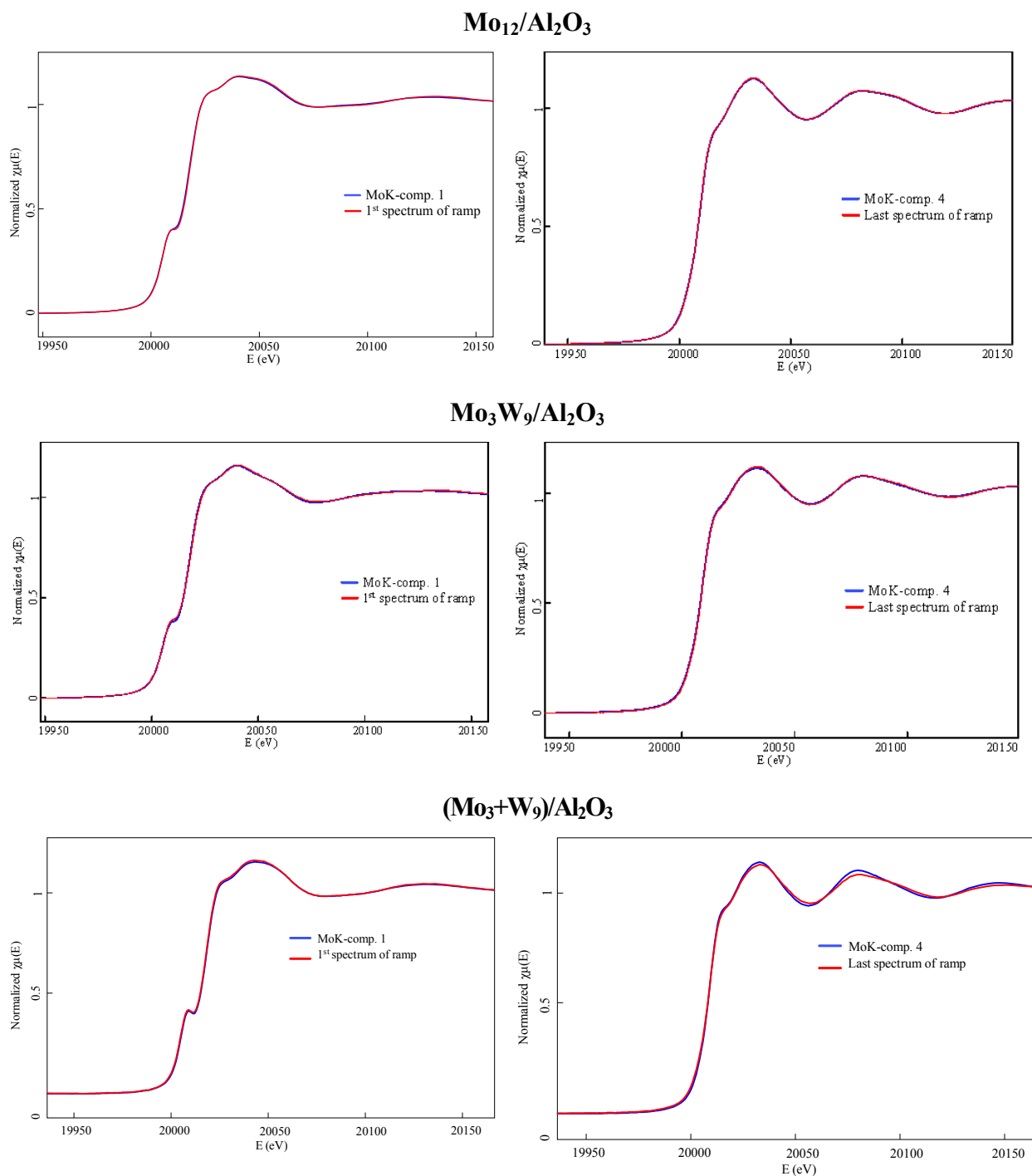
Supporting Information for Chapter 3

Characterization of (Mo)W/Al$_2$O$_3$ catalysts during in situ sulfidation by Quick-XAS

Mo$_{12}$/Al$_2$O$_3$

Mo$_3$W$_9$/Al$_2$O$_3$

(Mo$_3$+W$_9$)/Al$_2$O$_3$

Fig. S1. Mo K edge XANES spectra for the (Mo)W/Al$_2$O$_3$ catalysts: the first component determined by MCR-ALS compared to the first spectrum of the heating ramp(first line); the third component determined by MCR-ALS compared to the last spectrum of the ramp (second line).

W₁₂/Al₂O₃

Mo₃W₉/Al₂O₃

(Mo₃+W₉)/Al₂O₃

Fig. S2. W L$_I$ edge XANES spectra for the (Mo)W/Al$_2$O$_3$ catalysts: the first component determined by MCR-ALS compared to the first spectrum of the heating ramp (first line); the third component determined by MCR-ALS compared to the last spectrum of the plateau (second line).
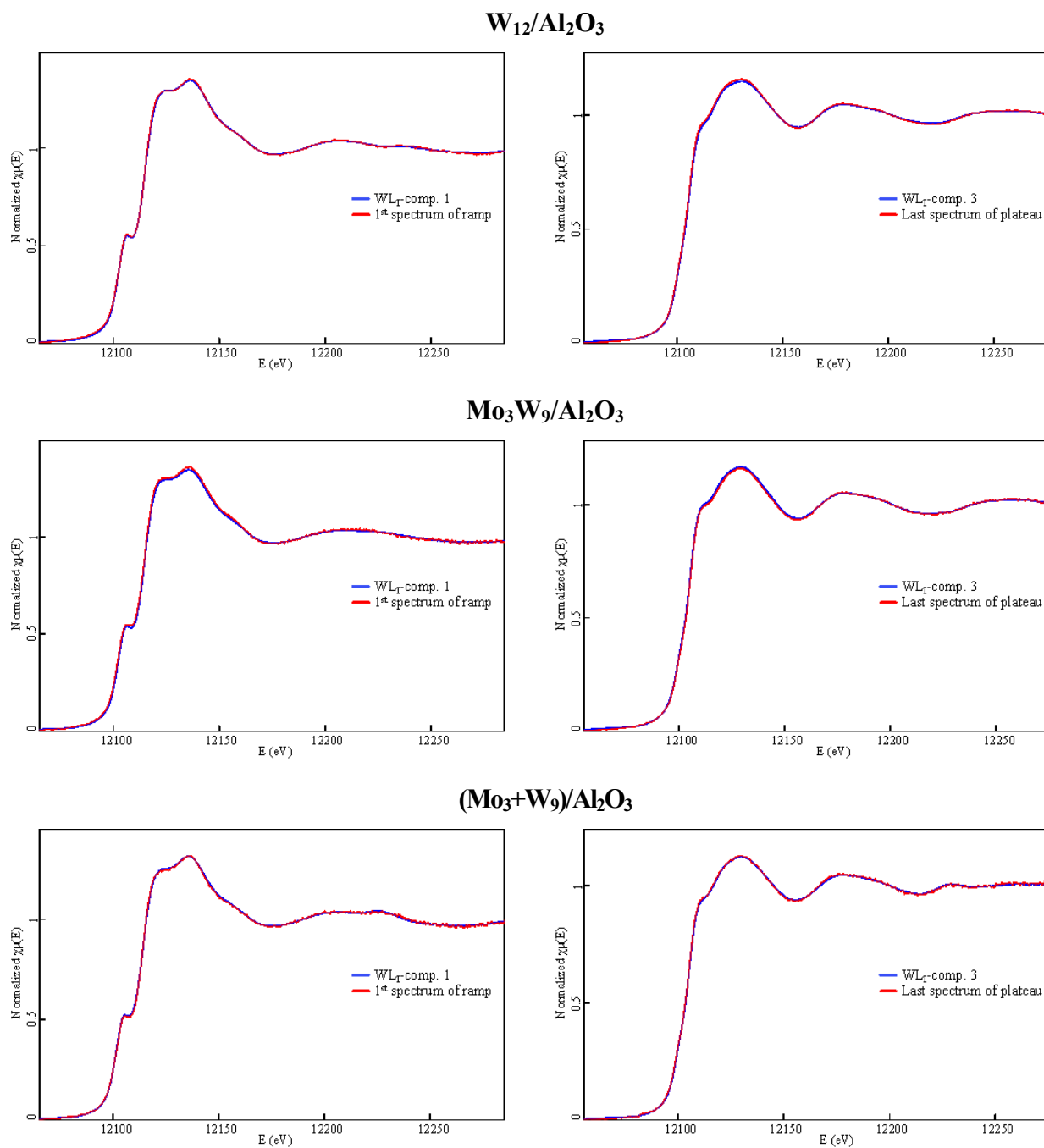
Supporting Information for Chapter 4

Characterization of Ni(Mo)W/Al$_2$O$_3$ sulfide catalysts by EXAFS

Mo K edge

NiMo$_{12}$/Al$_2$O$_3$

W L$_{III}$ edge

NiW$_{12}$/Al$_2$O$_3$

NiMo$_3$W$_9$/Al$_2$O$_3$

Ni(Mo$_3$+W$_9$)/Al$_2$O$_3$

Fig. S1. Magnitude of the Fourier transform of the Mo K edge and W L$_{III}$ edge spectra (solid line) and model (dotted line) for Ni(Mo)W/Al$_2$O$_3$ catalysts after sulfidation.